A SEARCH FOR THE STANDARD MODEL HIGGS BOSON DECAYING INTO TWO MUONS IN THE VECTOR BOSON ASSOCIATED PRODUCTION MODE AT THE CMS EXPERIMENT

By

XUNWU ZUO

A DISSERTATION PRESENTED TO THE GRADUATE SCHOOL
OF THE UNIVERSITY OF FLORIDA IN PARTIAL FULFILLMENT
OF THE REQUIREMENTS FOR THE DEGREE OF
DOCTORATE OF PHILOSOPHY

UNIVERSITY OF FLORIDA

2021

ACKNOWLEDGEMENTS

Still compiling the list of people to thank.

TABLE OF CONTENTS

page

ACKNOWLEDGEMENTS ... 3

LIST OF TABLES ... 7

LIST OF FIGURES ... 13

ABSTRACT ... 14

CHAPTER

1 INTRODUCTION ... 16

1.1 The standard model of particle physics ... 16
1.2 The measurements of Higgs couplings ... 20

2 THE LHC AND CMS ... 22

2.1 The Large Hadron Collider ... 22
2.2 The Compact Muon Solenoid experiment ... 28

3 OVERVIEW OF THE SEARCH OF H $\rightarrow \mu\mu$ DECAY AT CMS ... 33

3.1 Data and simulation samples ... 37
3.1.1 The simulation of the signal processes ... 38
3.1.2 The simulation of the background processes ... 39
3.2 Exclusive analyses and their strategies ... 40

4 OBJECT RECONSTRUCTION AND IDENTIFICATION ... 45

4.1 CMS object reconstruction ... 46
4.1.1 Tracks ... 47
4.1.2 Primary vertices ... 48
4.1.3 Beam spot ... 49
4.1.4 Muons ... 49
4.1.5 Electrons ... 51
4.1.6 Photons ... 53
4.1.7 Hadrons ... 55
4.1.8 Missing transverse momentum ... 56
4.2 Object selection in the H to muons analysis ... 58
4.2.1 Muon selection ... 58
4.2.2 Electron selection ... 59

5 MUON MOMENTUM CORRECTION AND CALIBRATION ... 61

5.1 Rochester correction ... 62
5.2 FSR recovery ... 63
5.3 GeoFit correction ... 65
5.3.1 Geometry of the track displacement ... 66
5.3.2 Development of GeoFit ... 70
5.3.3 Performance and validation ... 73
5.3.4 GeoFit vs track re-fit ... 74

5.4 Muon calibration results . . . 75

6 SEARCH FOR H2MU TARGETING THE VH PRODUCTION MODE . . . 85

6.1 Event selection . . . 88
6.2 MVA discrimination . . . 89
6.2.1 BDT targeting WH $\rightarrow \ell\nu + \mu\mu$ signal . . . 91
6.2.2 BDT targeting ZH $\rightarrow \ell\ell + \mu\mu$ signal . . . 94
6.2.3 Validation of the BDTs . . . 98
6.3 Event Categorization . . . 103
6.4 Signal and background modeling . . . 104
6.4.1 Signal modeling . . . 105
6.4.2 Background modeling . . . 107
6.5 Systematic uncertainties . . . 110
6.5.1 Signal shape uncertainties . . . 111
6.5.2 Signal rate uncertainties . . . 111
6.5.3 Background systematic bias . . . 116
6.6 Results of the VH analysis . . . 120

7 RESULTS OF THE H2MU SEARCH . . . 122

REFERENCES . . . 125

Tables page

1-1 The branching fractions of the main decay modes of the SM Higgs boson with a mass of 125 GeV. . . . 20

3-1 Production modes of the Higgs boson in pp collisions at the LHC, their cross sections for $m_{\mathrm{H}} = 125\mathrm{GeV}$, and the corresponding expected number of events in the dataset for this analysis (the cross sections multiplying $\mathscr{B}(\mathrm{H} \to \mu\mu)$ and the integrated luminosity ($137\mathrm{fb}^{-1}$). The leptons (ℓ) in the table refer to electrons or muons. . . . 37

3-2 Summary of the specification for the simulated Higgs signal samples. . . . 39

3-3 Summary of the specification for the simulated background samples. . . . 40

6-1 Selection criteria on muons and electrons in the VH analysis. . . . 88

6-2 Event selections for the WH and ZH categories. . . . 89

6-3 List of input variables used to train the signal-background separation BDT in the WH category. In this table, $\mu\mu_{\mathrm{H}}$ is the Higgs candidate, ℓ is the lepton from the W decay, μ_{OS} (μ_{SS}) refers to the muons in the Higgs candidate which OS (SS) to the lepton. . . . 93

6-4 List of input variables used to train the signal-background separation BDT in the ZH category. In this table, $\mu\mu_{\mathrm{H}}$ is the Higgs candidate, and $\ell\ell_{\mathrm{Z}}$ is the Z candidate. . 96

6-5 Normalization uncertainties on the Higgs boson production cross sections for various modes at $\sqrt{s} = 13\mathrm{TeV}$. . . . 112

6-6 Uncertainties on different signal components in the WH and ZH channels related to pileup re-weight and L1 prefiring re-weight. Numbers before/after are the affects from shifting the uncertainty source up/down. Uncertainties smaller than 0.1% are neglected. . . . 113

6-7 Uncertainties on different signal components in the WH and ZH channels related to the muon energy scale. Numbers before/after are the affects from shifting the uncertainty source up/down. Uncertainties smaller than 0.1% are neglected. . . . 113

6-8 Uncertainties on different signal components in the WH and ZH channels related to lepMVA scale factor. The lepMVA scale factor is the only scale factor applied to correct for the lepton efficiency modeling. The ID scale factor and Isolation scale factor are covered by the lepMVA scale factors. Numbers before/after are the affects from shifting the uncertainty source up/down. Uncertainties smaller than 0.1% are neglected. . . . 114

6-9 Uncertainties on different signal components in the WH and ZH channels related to B-jet vetoing. Numbers before/after are the affects from shifting the uncertainty source up/down. Uncertainties smaller than 0.1% are neglected. . . . 114

6-10 Uncertainties on different signal components in the WH Cat0 related to jet energy calibration. JEC uncertainties are in general small for the main signals in the WH and ZH channels. WH Cat0 is shown as an example. Numbers in other categories are similar. Numbers before/after are the affects from shifting the uncertainty source up/down. Uncertainties smaller than 0.1% are neglected.................. 115

6-11 Summary of the expect and observed limits and significance in each individual sub-category and the combination.. 121

LIST OF FIGURES

Figures page

1-1 The Standard Model of particles physics: 12 elementary fermions and 5 elementary bosons. Photo taken from [1]. 17

1-2 Summary of the CMS measurements on the Higgs coupling to fermions and bosons. Plot taken from [2]. 21

2-1 Photo taken from ... (original source unknown). An aerial view of the LHC landscape. The French-Swiss border is indicated by the yellow line and the LHC tunnels are outlined in white. The triangular building complex just below ATLAS in the picture is the main campus of CERN. 23

2-2 The schematic layout of the LHC. Each octant contains a insertion point. Points 1, 2, 5, and 8 are the locations of collision experiments. Points 3 and 7 are for beam collimation. Hadrons are injected at Points 1 and 8, accelerated at Point 4, and eventually discarded at Point 6. Plot taken from Ref. [3]. 24

2-3 Magnetic field of an ideal quadrupole. Plot taken from Ref. [4]. 25

2-4 An illustration of the interactions in a pp collision. The primary interaction in this example is the Higgs boson production in association with a top quark pair, whose Feynman diagram is shown in 3-2. Plot taken from Ref. [5]. 26

2-5 A cutaway diagram of the CMS detector. The design is specified to a design stage called the Phase-1 detector upgrade [6, 7, 8]. Plot taken from Ref. [9]. 28

2-6 A longitudinal section view of the CMS detector, gridded with the CMS coordinates. Plot taken from Ref. [10]. 29

2-7 The magnetic field in CMS displayed in a longitudinal section, operating with a central field strength of 3.8 T. The field value $|B|$ is shown on the left and the field lines are shown on the right. Plot taken from Ref. [11]. 30

2-8 Sketch of one quarter of the Phase-1 CMS tracking system in r-z view. The pixel detectors are shown in green, while single-sided and double-sided strip modules are depicted as red and blue segments, respectively. Plot taken from Ref. [12]. 31

3-1 A conceptual plot for the dimuon mass shapes for the signal and the background. The blue line shows the expected background shape, while the red line shows the expected signal shape on top of it. 34

3-2 Main production modes of the Higgs boson. 35

3-3 Examples of minor Higgs production modes. 36

3-4 Scheme of the procedure of assigning events to different categories. All events passing the common baseline selection are divided into four mutually exclusive categories: ggH, VBF, VH (WH and ZH), and $t\bar{t}H$ (leptonic and hadronic). 42

4-1 A transverse view of the CMS detector layout in the barrel region, with illustrations of the interactions between different particles and different detector components. Plot taken from Ref. [13]. 45

5-1 Performance of the *FSR recovery* in the simulated $\mathrm{H} \to \mu\mu$ events. The $m_{\mu\mu}$ before and after the *FSR recovery* are shown for the events that contain at least one FSR photon (left), and for the inclusive signal events (right). Plot taken from Ref. [14]. 64

5-2 Performance of the *FSR recovery* in the $\mathrm{Z} \to \mu\mu$ events that contain FSR photons, in both data and simulation. A good agreement between simulation and data is observed, before or after the correction. Plot taken from Ref. [14]. 64

5-3 Scheme of the d0 definition in CMS. The (x_0, y_0) is the coordinate of a point near the vertex in the frame where the vertex is at $(0,0)$, and the ϕ_0 is the azimuthal angle of the track at (x_0, y_0). 67

5-4 Scheme of the track geometry in the transverse plane. The blue lines show the geometry of the reconstructed track, compared to the black lines which are the geometry of the true track. The difference between the blue track and black track is exaggerated in this scheme. The blue track and the black track must intersect at two points. l is the distance between the two intersections, and x is the distance between the true vertex and the first intersection. s is the distance between the circular centers of the two tracks. 68

5-5 Example plots showing the correlation between $(p_{\mathrm{T}}^{reco} - p_{\mathrm{T}}^{gen})/(p_{\mathrm{T}}^{gen})^2$ and d0 $\cdot$ charge. The vertices used for the d0 calculation are the PV (left) and the BS (right). The PV plot shows a modulated dependence from expectation while the BS plot shows a linear shape as expected. Only barrel tracks from 2016 data are shown as examples. Plots of other $|\eta|$ regions and other data-taking periods show similar behaviors. Plots credit to Efe Yigitbasi. 71

5-6 Plots for the $(p_{\mathrm{T}}^{reco} - p_{\mathrm{T}}^{gen})/(p_{\mathrm{T}}^{gen})^2$ vs d0 correlation in the 2016 DY simulation, and the linear fits to them. Muon tracks are divided into three different $|\eta|$ regions: $|\eta| < 0.9$ (left), $0.9 < |\eta| < 1.7$ (middle), and $1.7 < |\eta|$ (right). Plots credit to Efe Yigitbasi.. 72

5-7 Plots for the $(p_{\mathrm{T}}^{reco} - p_{\mathrm{T}}^{gen})/(p_{\mathrm{T}}^{gen})^2$ vs d0 correlation in the 2017 DY simulation, and the linear fits to them. Muon tracks are divided into three different $|\eta|$ regions: $|\eta| < 0.9$ (left), $0.9 < |\eta| < 1.7$ (middle), and $1.7 < |\eta|$ (right). Plots credit to Efe Yigitbasi.. 72

5-8 Plots for the $(p_{\mathrm{T}}^{reco} - p_{\mathrm{T}}^{gen})/(p_{\mathrm{T}}^{gen})^2$ vs d0 correlation in the 2018 DY simulation, and the linear fits to them. Muon tracks are divided into three different $|\eta|$ regions: $|\eta| < 0.9$ (left), $0.9 < |\eta| < 1.7$ (middle), and $1.7 < |\eta|$ (right). Plots credit to Efe Yigitbasi.. 72

5-9 Plots showing the p_T dependence on the d0 value with different stages of muon correction. The plots compare the $Z \to \mu\mu$ peak in data and simulation for three years (2016-2018) combined. All positively charged muons are put in the left plot and all negatively charged ones are put in the right plot. The p_T-d0 dependence is reversed for positive and negative muons. 73

5-10 Plots showing the *GeoFit correction* improvement on the four main $H \to \mu\mu$ signal modes, ggH and VBF plotted on the left, and VH and $t\bar{t}H$ plotted on the right. The plots are made combining the expected signal in all three years of data-taking (2016-2018). The relative improvements on $m_{\mu\mu}$ resolution for ggH, VBF, VH, and $t\bar{t}H$ modes are, respectively, 6.1%, 7.8%, 8.0%, and 9.8%. 74

5-11 Plots of the $m_{\mu\mu}$ shape of the 2018 ggH simulation sample, comparing different muon correction methods. The left plot shows the $m_{\mu\mu}$ distribution calculated with muon tracks re-fit with the additional BS constraint, compared with the particle flow shape (left plot). The *Rochester correction* is not applied in the left plot for both the red and the blue lines. The right plot shows the $m_{\mu\mu}$ distribution from the re-fit method, with the *Rochester correction* applied, compared with the shape from *GeoFit correction* + *Rochester correction* (right plot). Plots credit to Pierluigi Bortignon. 75

5-12 Muon calibration plots vs $\eta(\mu^+)$, for 2016 (left column), 2017 (middle column) and 2018 (right column). The top row shows the mean value of the Voigtian fit to the $m_{\mu\mu}$ distribution, while the bottom row shows its experimental resolution. 77

5-13 Muon calibration plots vs $\phi(\mu^+)$, for 2016 (left column), 2017 (middle column) and 2018 (right column). The top row shows the mean value of the Voigtian fit to the $m_{\mu\mu}$ distribution, while the bottom row shows its experimental resolution. 78

5-14 Muon calibration plots vs $\phi(\mu^-)$, for 2016 (left column), 2017 (middle column) and 2018 (right column). The top row shows the mean value of the Voigtian fit to the $m_{\mu\mu}$ distribution, while the bottom row shows its experimental resolution. 79

5-15 Muon calibration plots vs $p_T(\mu^+)$, for 2016 (left column), 2017 (middle column) and 2018 (right column). The top row shows the mean value of the Voigtian fit to the $m_{\mu\mu}$ distribution, while the bottom row shows its experimental resolution. The p_T binning sculpts the shape of the $m_{\mu\mu}$ peak, which leads to a jump at the p_T = 45 GeV in the plots. 80

5-16 Muon calibration plots vs $p_T(\mu\mu)$, for 2016 (left column), 2017 (middle column) and 2018 (right column). The top row shows the mean value of the Voigtian fit to the $m_{\mu\mu}$ distribution, while the bottom row shows its experimental resolution. 81

5-17 Muon calibration plots vs $\eta(\mu\mu)$, for 2016 (left column), 2017 (middle column) and 2018 (right column). The top row shows the mean value of the Voigtian fit to the $m_{\mu\mu}$ distribution, while the bottom row shows its experimental resolution. 82

5-18 Muon calibration plots vs $d0(\mu^+)$, for 2016 (left column), 2017 (middle column) and 2018 (right column). The top row shows the mean value of the Voigtian fit to the $m_{\mu\mu}$ distribution, while the bottom row shows its experimental resolution. 83

5-19 Muon calibration plots vs $d0(\mu^-)$, for 2016 (left column), 2017 (middle column) and 2018 (right column). The top row shows the mean value of the Voigtian fit to the $m_{\mu\mu}$ distribution, while the bottom row shows its experimental resolution. 84

6-1 Plots of the performance of the WH $\rightarrow 3\ell$. On the left, the BDT output score, with signal in blue and background in red. On the right, the receiver operating characteristic (ROC) curve, with training sample in red and testing sample in blue. A slight over-training is observed in the region of low signal efficiency, due to the fluctuation in background. As will be shown in Fig. 6-5, the BDT dose not sculpt the shape of $m_{\mu\mu}$ 93

6-2 Input variables to the WH $\rightarrow 3\ell$ BDT, with signal in blue and background in red. .. 94

6-3 Plots of the performance of the ZH $\rightarrow 4\ell$ BDT. On the left, the BDT output score, with signal in blue and background in red. On the right, the receiver operating characteristic (ROC) curve, with training in red and testing in blue. 96

6-4 Input variables to the ZH $\rightarrow 4\ell$ BDT, with signal in blue and background in red. ... 97

6-5 For the WH BDT, the distribution of the dimuon mass shape in the background for five different BDT quantile (left), and the distribution of the BDT output for three different signal mass assumptions (right). 98

6-6 For the ZH BDT, the distribution of the dimuon mass shape in the background for five different BDT quantile (left), and the distribution of the BDT output for three different signal mass assumptions (right). 99

6-7 The WH BDT output (left) and the ZH BDT output (right) in full Run 2 in the signal region 110 GeV $< m_{\mu\mu} <$ 150 GeV. 99

6-8 Input variables to the WH BDT in full Run 2 in the signal region 110 GeV $< m_{\mu\mu}$ $<$ 150 GeV. 100

6-9 Input variables to the ZH BDT in full Run 2 in the signal region 110 GeV $< m_{\mu\mu} <$ 150 GeV. 101

6-10 The input variable $M_{\mathrm{T}}(\mu_{SS}$,MHT) to the WH BDT (left), and the BDT output for signal and background in different $M_{\mathrm{T}}(\mu_{SS}$,MHT) bins (right). A mild disagreement is seen between the simulation and data in the low bins of $M_{\mathrm{T}}(\mu_{SS}$,MHT), while the BDT is not sensitive to the $M_{\mathrm{T}}(\mu_{SS}$,MHT) values in that region. 102

6-11 Scans for the first (left), second (middle) and a potential third (right) BDT cut in the WH channel. The first BDT cut is chosen at 0.3. The second BDT cut is chosen at -0.1. A third BDT cut is not necessary. 103

6-12 Scans for the BDT cut in the ZH channel. The BDT cut is chosen at -0.1. 104

6-13 The signal modeling in the WH $\rightarrow \ell+\mu\mu$ inclusive category. Considered signal modes are WH (top left), qqZH (top middle), ggZH (top right), ttH (bottom left), THQ (bottom middle), and THW (bottom right). 106

6-14 The signal modeling in the ZH $\rightarrow \ell\ell+\mu\mu$ inclusive category. Considered signals modes are qqZH (left) and ggZH (right). 106

6-15 Schemes on how the bias affects the uncertainty on the signal strength measurement. The left plot is an illustration of the $[-\sigma,\sigma]$ coverage of the biased signal strength measurement. The middle plot shows this coverage becomes less as the bias gets larger. The right plot shows how the bias impacts the best fit signal strength uncertainty σ_{fit}. The gray dash lines in the right plot indicates the conventional acceptable range of the bias in this analysis. 117

6-16 Bias in different BDT-based WH sub-categories. The sub-categories are: Cat0 BDT [-1.0, -0.1] (left), Cat1 BDT [-0.1, 0.3] (middle), Cat2 BDT [0.3, 1.0] (right). In the tables, the Power stands for a single "Power" function and the "PowerInt" stands for a single power function plus a constant. 119

6-17 Bias in different BDT-based ZH sub-categories. The sub-categories are: Cat0 BDT [-1.0, -0.1] (left), Cat1 BDT [-0.1, 1.0] (right). In the tables, the "Power" stands for a single power function and the "PowerInt" stands for a single power function plus a constant. 119

6-18 Post-fit $m_{\mu\mu}$ distribution of the WH sub-categories. The sub-categories are: Cat0 BDT [-1.0, -0.1] (left), Cat1 BDT [-0.1, 0.3] (middle), Cat2 BDT [0.3, 1.0] (right). The upper panel in the plots shows the distribution of observed data and the shape of the signal-plus-background fit. The lower panel in the plots shows the residual distribution after subtracting the background component in the fits. The green and yellow bands show the one and two standard deviation of the background component uncertainty. Plots taken from Ref. [15]. 120

6-19 Post-fit $m_{\mu\mu}$ distribution of the ZH sub-categories. The sub-categories are: Cat0 BDT [-1.0, -0.1] (left), Cat1 BDT [-0.1, 1.0] (right). The upper panel in the plots shows the distribution of observed data and the shape of the signal-plus-background fit. The lower panel in the plots shows the residual distribution after subtracting the background component in the fits. The green and yellow bands show the one and two standard deviation of the background component uncertainty. Plots taken from Ref. [15]. 121

7-1 Expected fraction of signal events per production mode in the different sub-categories for $m_{\mathrm{H}} = 125.38$ GeV. The tH contribution is defined as the sum of tHq and tHW processes. Plot taken from Ref. [15]. 122

7-2 Expected $S/(S+B)$ and $S/\sqrt{B}$ in different sub-categories, where S and B indicate the number of expect signal and background events, respectively. Plot taken from Ref. [15]. 123

7-3 Signal strength modifiers measured for $m_{\mathrm{H}} = 125.38$ GeV in each production category (black points) are compared to the result of the combined fit (solid red line) and the SM expectation (dashed gray line). Plot taken from Ref. [15]. 124

7-4 The local p-values as a function of different m_{H} hypotheses, for each individual categories as well as the overall combination. The left plot shows the observed p-values, each solid marker indicating a mass point for which the observed p-values are computed. The right plot shows the expected p-values calculated using the background estimate from the S+B fit and injecting a signal with $m_{\mathrm{H}} = 125.38$ GeV and $\mu = 1$. Plot taken from Ref. [15]. 124

7-5 The observed profile likelihood ratio as a function of κ_{μ} for $m_{\mathrm{H}} = 125.38$ GeV. Plot taken from Ref. [15]. 125

7-6 Left: A duplicate of Figure 1-2, taken from Ref. [2]. Summary of the CMS measurements on the Higgs coupling to fermions and bosons based on data recorded in 2016. Right: The coupling strength measurements updated with this $\mathrm{H} \to \mu\mu$ result. Plot taken from Ref. [15].. 126

Abstract of Dissertation Presented to the Graduate School
of the University of Florida in Partial Fulfillment of the
Requirements for the Degree of Doctorate of Philosophy

A SEARCH FOR THE STANDARD MODEL HIGGS BOSON DECAYING INTO TWO MUONS IN THE VECTOR BOSON ASSOCIATED PRODUCTION MODE AT THE CMS EXPERIMENT

By

Xunwu Zuo

May 2021

Chair: Darin Acosta
Major: Physics

The Higgs boson was proposed in the 1960s as one of the fundamental particles in the standard model (SM) of particle physics, In 2012, the ATLAS and CMS experiments at the LHC discovered a scalar boson with a mass about 125 GeV that was later confirmed, through dedicated measurements of its properties, to be the Higgs boson of the SM. One of the important properties of the Higgs boson is its coupling to muons, which is an elementary second generation fermion in the SM. Any disagreement between the observed coupling and the SM prediction would indicate new physics phenomena beyond the SM, while an agreement would further validate the SM and help measure parameters in the theory of Higgs physics.

This thesis report on the first evidence for the Higgs boson decay to a pair of muons, based on proton-proton collision data at $\sqrt{s} = 13$ TeV recorded by the CMS experiment at the LHC, corresponding to an integrated luminosity of 137 fb^{-1}. The analysis is performed in four exclusive categories targeting different production modes of the Higgs boson: via gluon fusion, via vector boson fusion, in association with a vector boson, and in association with a top quark pair. This thesis is focused on the exclusive category of the Higgs boson production in association with a vector boson, in which an excess of events over the background expectation is observed in data with a significance of 2.0 standard deviations, while the expected significance for the SM Higgs boson with mass of 125.38 GeV is 0.42 standard deviations.

The combination of the four exclusive categories yields an overall observed significance of 3.0 standard deviations, while the expectation is 2.5. This result is also combined with the that from the data recorded at $\sqrt{s} = 7$ and 8 TeV, corresponding to integrated luminosities of 5.1 and 19.7 fb^{-1}, respectively, whose effect is an increase in both the expected and observed significance by 1%. The measured signal strength. relative to the SM prediction, is $1.19^{+0.40}_{-0.39}(\mathrm{stat})^{+0.15}_{-0.14}(\mathrm{syst})$. This result establishes the first evidence for the Higgs boson decay to second generation fermions, with a branching fraction consistent with the SM prediction, and provides the most precise measurement of the Higgs boson coupling to muons to date.

CHAPTER 1
INTRODUCTION

1.1 The standard model of particle physics

The success of modern particle physics, since its inception in 1970s, is summarized as the Standard Model (SM) of particle physics. It is a formulation that describes all known elementary particles, and three of the four known fundamental interactions between them: the electromagnetic, weak, and strong interactions, but not the gravitational interaction whose quantization is not yet confirmed. Elementary particles can be classified into fermions and bosons, based on their spins. Elementary fermions are spin 1/2 particles that form matter in the macroscopic world as we know, while elementary bosons have integer spins (0 or 1) and are the carrier of particle interactions. Fermions are further categorized into quarks and leptons, each has three generations. In each generation, there is one charge $= +\frac{2}{3}$ quark (u, c, and t for each generation), one charge $= -\frac{1}{3}$ quark (d, s, and b), one charge = 1 lepton (e, μ, and τ), and one neutral lepton (ν_e, ν_μ, and ν_τ). Each of these particles is complemented with an anti-particle which has the same mass and spin as the particle itself, but opposite charge and other quantum numbers. There are two types of elementary bosons, the vector bosons (also called gauge bosons) that have spin = 1 and the scalar boson with has spin = 0. Gauge bosons are the carriers of fundamental interactions: photons for the electromagnetic interaction, the W and Z bosons for the weak interaction, and gluons for the strong interaction. The Higgs boson is the only scalar boson in the SM, which couples to all massive elementary particles and provide the mechanism for them to be massive. The elementary particles of the SM is summarized in Figure 1-1.

The SM is mathematically constructed within Quantum Field Theory with a structure of the product of an SU(3), an SU(2), and an U(1) groups. The Lagrangian density of the SM is expressed as:

$$\begin{aligned}\mathscr{L} =&\bar{\psi}^i(i\gamma^\mu)(\mathscr{D}_\mu)_{ij}\psi^j - -\frac{1}{4}G^a_{\mu\nu}G^{a\mu\nu} - \frac{1}{4}W^a_{\mu\nu}W^{a\mu\nu} - \frac{1}{4}B_{\mu\nu}B^{\mu\nu} \\ &- m_f\bar{\psi}^i_f\psi_{fi} + \frac{1}{2}m_G^2G_\mu G^\mu + \frac{1}{2}m_W^2W_\mu W^\mu + \frac{1}{2}m_B^2B_\mu B^\mu\end{aligned} \tag{1-1}$$

In the equation:

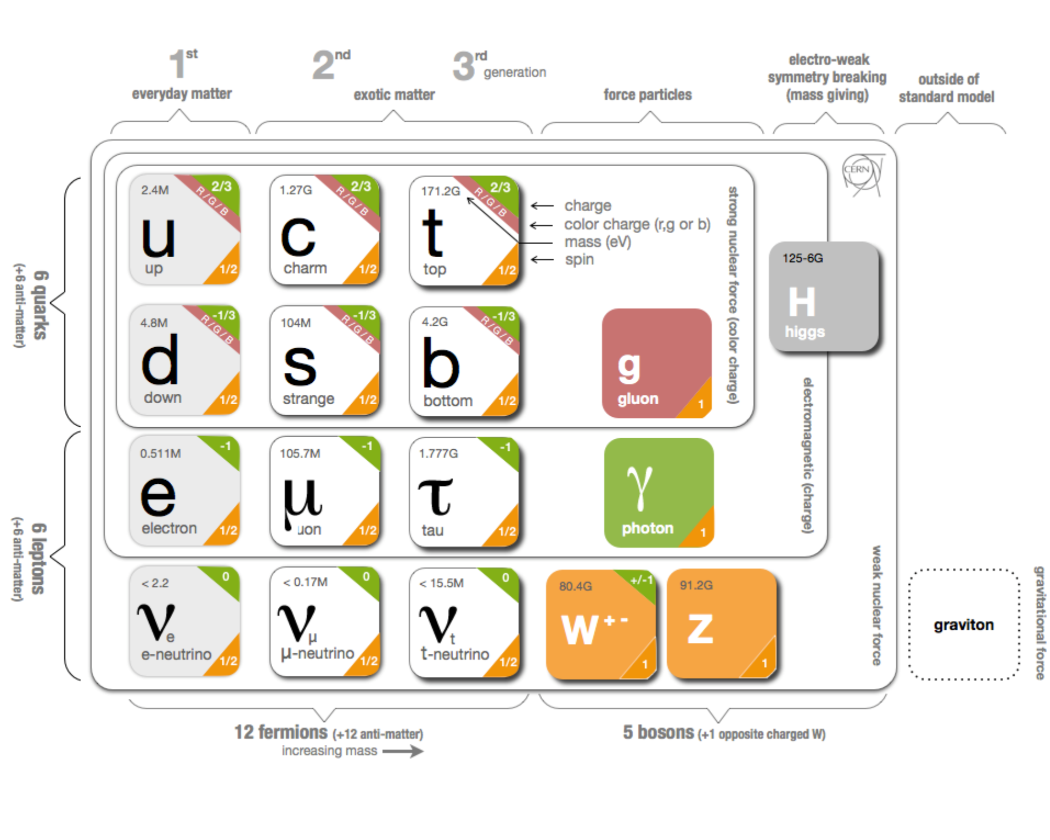

Figure 1-1. The Standard Model of particles physics: 12 elementary fermions and 5 elementary bosons. Photo taken from [1].

- ψ is the fermion field (matter field);
- $G^a_{\mu\nu}$, $W^a_{\mu\nu}$, and $B_{\mu\nu}$ are field strength tensors for the interaction fields corresponding to the groups SU(3), an SU(2), and an U(1), respectively;
- $\mathscr{D}_\mu$ is the covariant derivative operator: $\mathscr{D}_\mu\psi = (\partial_\mu - ig'B_\mu Y - igW^a_\mu T^a - ig_s G^a_\mu t^a)\psi$, g', g, and g_s being field strength coefficients, and Y, T^a, and t^a being interaction operators;
- Index a is the index of the group generators, which runs from 1 to 8 for the gluon, and 1 to 3 for the W boson;
- m_f, m_G, m_W, and m_B are the masses of the fermion, gluon, W boson, and the neutral gauge boson;
- μ and ν are the Lorentz vector indices.

The second line in Equation 1-1 indicates that fermions and gauge bosons can be massive. However, these terms unlike the terms in the first line, are not invariant under local gauge transformation. An additional scalar field is introduced, which interacts with the fermion and boson fields, leading to a spontaneous symmetry breaking and allowing the mass terms to appear in Equation 1-1 without violating gauge invariance. This is scalar field is called the Higgs field and its effect is called the Higgs mechanism.

The Higgs field is a complex scalar field whose potential is:

$$V(\Phi) = -\mu^2\Phi^\dagger\Phi + \lambda(\Phi^\dagger\Phi)^2 \tag{1-2}$$

in which Φ is the complex scalar field and μ, λ are coefficients. λ needs to be positive for $V(\Phi)$ to have a minimum value. If $\mu^2 = 0$, the minimum of $V(\Phi)$ is zero, when $|\Phi| = 0$, and the no mass is raised for the fermions and bosons. If $\mu^2 < 0$, $V(\Phi)$ shall have a nonzero minimum value when $|\Phi^\dagger\Phi| = \frac{\mu^2}{2\lambda}$. In gauge transformation, when reducing Φ to a real scalar field ϕ, it can be rewrote as $\phi = v + h$, where $v = \frac{\mu^2}{\lambda}$ is a constant, the Lagrangian of the Higgs field can be written as:

$$\mathscr{L}_H = -V(\Phi) = -\lambda v^2 h^2 - \lambda v h^3 - \frac{\lambda}{4}h^4 + const. \tag{1-3}$$

in which the first term is the mass term of the Higgs boson, the second term is the tri-Higgs coupling vertex term, and the third term is the quad-Higgs coupling term. The Higgs mass, from the first term, is:

$$m_h = \sqrt{2\lambda}\,v \tag{1-4}$$

where v can be determined from theory $v = 246$ GeV, while λ is an unknown parameter.

Adding the Higgs field to a massless SM Lagrangian, the Lagrangian becomes:

$$\begin{aligned}\mathscr{L} =& \bar{\psi}^i(i\gamma^\mu)(\mathscr{D}_\mu)_{ij}\psi^j - -\frac{1}{4}G^a_{\mu\nu}G^{a\mu\nu} - \frac{1}{4}W^a_{\mu\nu}W^{a\mu\nu} - \frac{1}{4}B_{\mu\nu}B^{\mu\nu}\\ &+ \mu^2\Phi^\dagger\Phi - \lambda(\Phi^\dagger\Phi)^2\\ &+ (\mathscr{D}_\mu\Phi)^\dagger(\mathscr{D}^\mu\Phi)\\ &- y_e\bar{L}^L\Phi e_R - y_u\bar{Q}_L\bar{\Phi}u_R - y_d\bar{Q}_L\Phi d_R + (h.c.)\end{aligned} \tag{1-5}$$

where the first line is the massless SM terms, the second line is the Higgs self-interaction term, the third line is the Higgs-gauge interaction term, and the fourth line is the Higgs-fermion interaction term.

The Higgs-gauge term can be expanded as:

$$
\begin{aligned}
(\mathscr{D}_\mu \Phi)^\dagger (\mathscr{D}^\mu \Phi) =& \frac{1}{2}(\partial_\mu h)(\partial^\mu h) \\
&+ \frac{g^2 v^2}{4} W_\mu^+ W_\mu^- + \frac{(g^2+g'^2)v^2}{8} Z_\mu Z^\mu \\
&+ \frac{g^2 v}{2} h W_\mu^+ W_\mu^- + \frac{g^2}{2} hh W_\mu^+ W_\mu^- \\
&+ \frac{(g^2+g'^2)v}{4} h Z_\mu Z^\mu + \frac{g^2+g'^2}{8} hh Z_\mu Z^\mu
\end{aligned}
\tag{1-6}
$$

in which the first line is the Higgs kinetic term, the second line is the mass terms for W and Z bosons, the third line is the hWW and hhWW interaction vertices, and the fourth line is the hZZ and hhZZ interaction vertices. From this Lagrangian, the W and Z boson have masses of

$$
\begin{aligned}
m_W &= \frac{gv}{2} \\
m_Z &= \frac{v}{2}\sqrt{g^2+g'^2}
\end{aligned}
\tag{1-7}
$$

The Higgs-fermion terms, also called the Yukawa term, can be expanded as:

$$
\begin{aligned}
\mathscr{L}_{Yukawa} =& -(\frac{y_e v}{\sqrt{2}})\bar{e}e - \frac{y_e}{\sqrt{2}} h\bar{e}e \\
&-(\frac{y_u v}{\sqrt{2}})\bar{u}u - \frac{y_u}{\sqrt{2}} h\bar{u}u \\
&-(\frac{y_d v}{\sqrt{2}})\bar{d}d - \frac{y_d}{\sqrt{2}} h\bar{d}d
\end{aligned}
\tag{1-8}
$$

in which the each line has a fermion mass term and a Higgs-fermion vertex term, and the three lines are for leptons, up-type quarks, and down-type quarks, respectively. As a result, the masses of leptons and two types of quarks are

$$
m_e = \frac{y_e v}{2}, \qquad m_u = \frac{y_u v}{2}, \qquad m_d = \frac{y_d v}{2} \tag{1-9}
$$

Overall, fermions, the W, Z bosons, and the Higgs boson itself are allowed to be massive through the Higgs mechanism (Equations 1-4, 1-7, and 1-9). The Higgs mechanism is experimentally confirmed by the observation of the Higgs boson by ATLAS and CMS Collaborations in 2012 [16, 17, 18], while the latest and most precise measurement of the Higgs mass is 125.38 ± 0.14 GeV from the CMS Collaboration [19]. Furthermore, the Higgs boson couples to the W, Z bosons through gauge coupling, whose coupling strength is proportional to the mass of the gauge boson. Similarly, the Higgs boson couples to fermions through Yukawa coupling, whose coupling strength is also proportional to the mass of the fermion. Therefore, precise measurements of the Higgs coupling strength to different particles are keys to further validate the SM and search for new physics beyond the SM.

1.2 The measurements of Higgs couplings

The Higgs boson couples to all massive elementary particles, and can decay to most of them (except the top quark whose mass is greater than the Higgs boson). The branching fractions of the decays are directly related to the coupling strength. The Higgs boson can also decay to massless particles (gluons and photons) through top-quark-induced or W-boson-induced loop diagrams. Table 1-1 lists the branching fractions of the main decay modes of the Higgs boson.

Table 1-1. The branching fractions of the main decay modes of the SM Higgs boson with a mass of 125 GeV.

Decay mode	Branching fraction
$\mathrm{H} \to \mathrm{b\bar{b}}$	58.4%
$\mathrm{H} \to \mathrm{W^+W^-}$	21.4%
$\mathrm{H} \to gg$	8.19%
$\mathrm{H} \to \tau\bar{\tau}$	6.26%
$\mathrm{H} \to c\bar{c}$	2.89%
$\mathrm{H} \to \mathrm{ZZ}$	2.62%
$\mathrm{H} \to \gamma\gamma$	0.227%
$\mathrm{H} \to \mathrm{Z}\gamma$	0.153%
$\mathrm{H} \to \mu\bar{\mu}$	0.022%

The Higgs boson decay to electroweak gauge bosons and charged fermions of the third generation (except the top quark) had been observed, with coupling strengths consistent with the SM prediction [20, 21, 22, 23, 24, 25, 26, 27, 28]. In addition, the Higgs boson coupling to the top quark has also been measured through the Higgs production process in association with a top quark pair [29, 30]. The measurements on the Higgs coupling strengths from CMS with the LHC proton-proton collision data collected in 2016 is summarized in Figure 1-2, in which, the gauge couplings and Yukawa couplings are expressed by the coupling modifiers (κ_{W}, κ_{Z}, κ_t, κ_τ, κ_b, and κ_μ) in the κ-framework [31]. It shows a incredible agreement between the experimental measurements and the SM predictions for particles across a mass range of order 10^4. However, the measurement on the Higgs to muon coupling, due to the small branching fraction, is not as precise as the other ones. This measurement, through the study of $\mathrm{H} \to \mu\mu$ decay, is particularly important as it is the only constraining point on the low-mass side in Figure 1-2 ans it is the most experimentally sensitive measurement of the Higgs boson couplings to second-generation fermions.

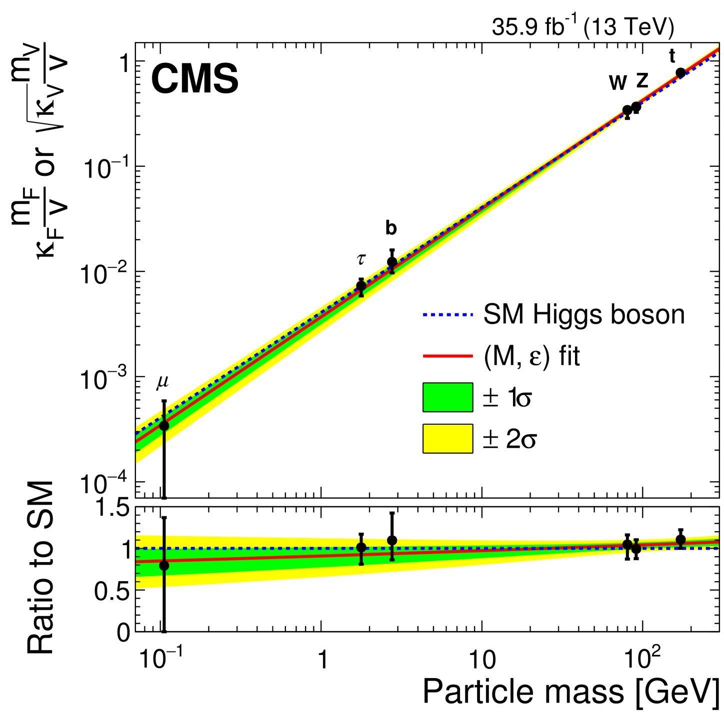

Figure 1-2. Summary of the CMS measurements on the Higgs coupling to fermions and bosons. Plot taken from [2].

CHAPTER 2
THE LHC AND CMS

The Standard Model provides a precise description of the elementary particles we have known. But there remains fundamental questions to be answered. Is there a Higgs boson that provides the mechanism for particles to be massive? Are there more than one type of Higgs bosons? Is supersymmetry a real? What are dark matter and dark energy? Why is there far more matter than antimatter in the observed universe? Are there phenomena in particle physics that cannot be explained by the existing theories?

A good way to study these questions at the same time is via high energy hadron collisions. The Large Hadron Collider is the most powerful hadron collider that human have built for this purpose, and the Compact Muon Solenoid (CMS) experiment is one of the experiments at the LHC that study the outcome of the collisions. An overview of the LHC is given in Section 2.1, and the CMS detector is described in Section 2.2.

2.1 The Large Hadron Collider

The Large Hadron Collider (LHC) [3] at CERN near Geneva Switzerland is the world's largest and most powerful machine for particle physics research. It is a double-ring superconducting hadron accelerator and collider installed in a 26.7 km circular tunnel inherited from its predecessor, the Large Electron-Positron Collider (LEP). The LHC tunnel lies in the rock stratum between 45 m and 170 m underground, and spans across the French-Swiss border from the bank of the Geneva Lake to the base of the Jura mountain. Figure 2-1 shows the geographical location of the LHC. Two series of hadron bunches rotate in opposite directions in the main LHC ring and collide at four interaction points, each hosting a major LHC experiments: Point 1 for ATLAS, Point 2 for ALICE, Point 5 for CMS, and Point 8 for LHCb.

The LHC tunnel consists eight arc and eight straight sections. The arcs make the majority of the LHC circumference, accommodating thousands of the magnet units to bend and tighten the particles' trajectory. The straight sections are approximately 528 m long each, serving as insertions for experiments or utility. The arcs and straight sections are grouped into eight octants, each covering a straight section and two halves of its neighbor-

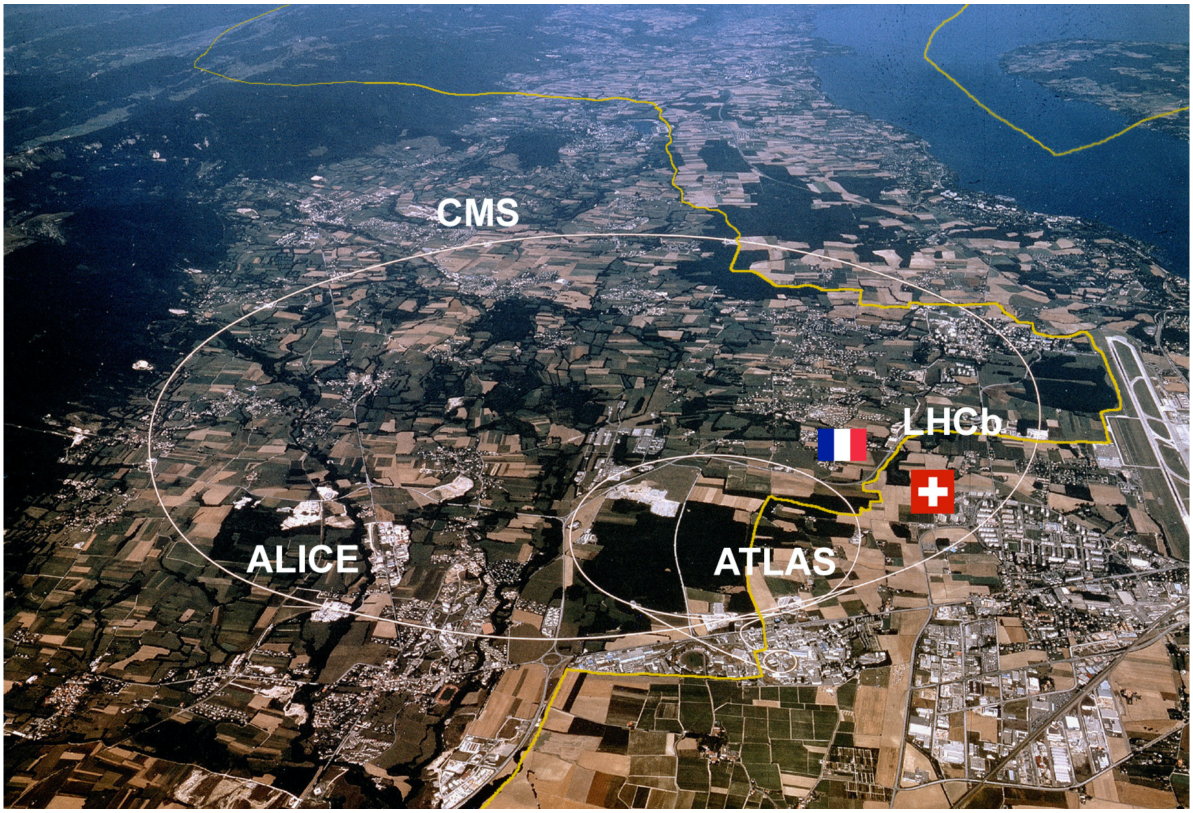

Figure 2-1. Photo taken from ... (original source unknown). An aerial view of the LHC landscape. The French-Swiss border is indicated by the yellow line and the LHC tunnels are outlined in white. The triangular building complex just below ATLAS in the picture is the main campus of CERN.

ing arcs, whose geometrical layout is shown in Figure 2-2.

Strong magnets are what guide the high energy hadrons to circulate and collide in the LHC. The LHC magnet system is based on Nb-Ti cables, cooled by superfluid helium to a temperature of 1.9 K, where the cables stay superconductive and generate a magnetic field up to their critical field strength. The maximum operable magnetic field of the LHC magnets is 8.33 T, which corresponds to a proton beam energy of 7 TeV, or a heavy ion beam energy of 2.76 TeV per nucleon.

The LHC magnet system consists 1232 main dipole magnets, about 450 quadrupole magnets, a few thousands multipole corrector magnets, and several types of specialized magnets at the eight insertion points. The dipoles bend the beams so they circulate in the LHC tunnel. Since the both beams are positively charged but travel in opposite direc-

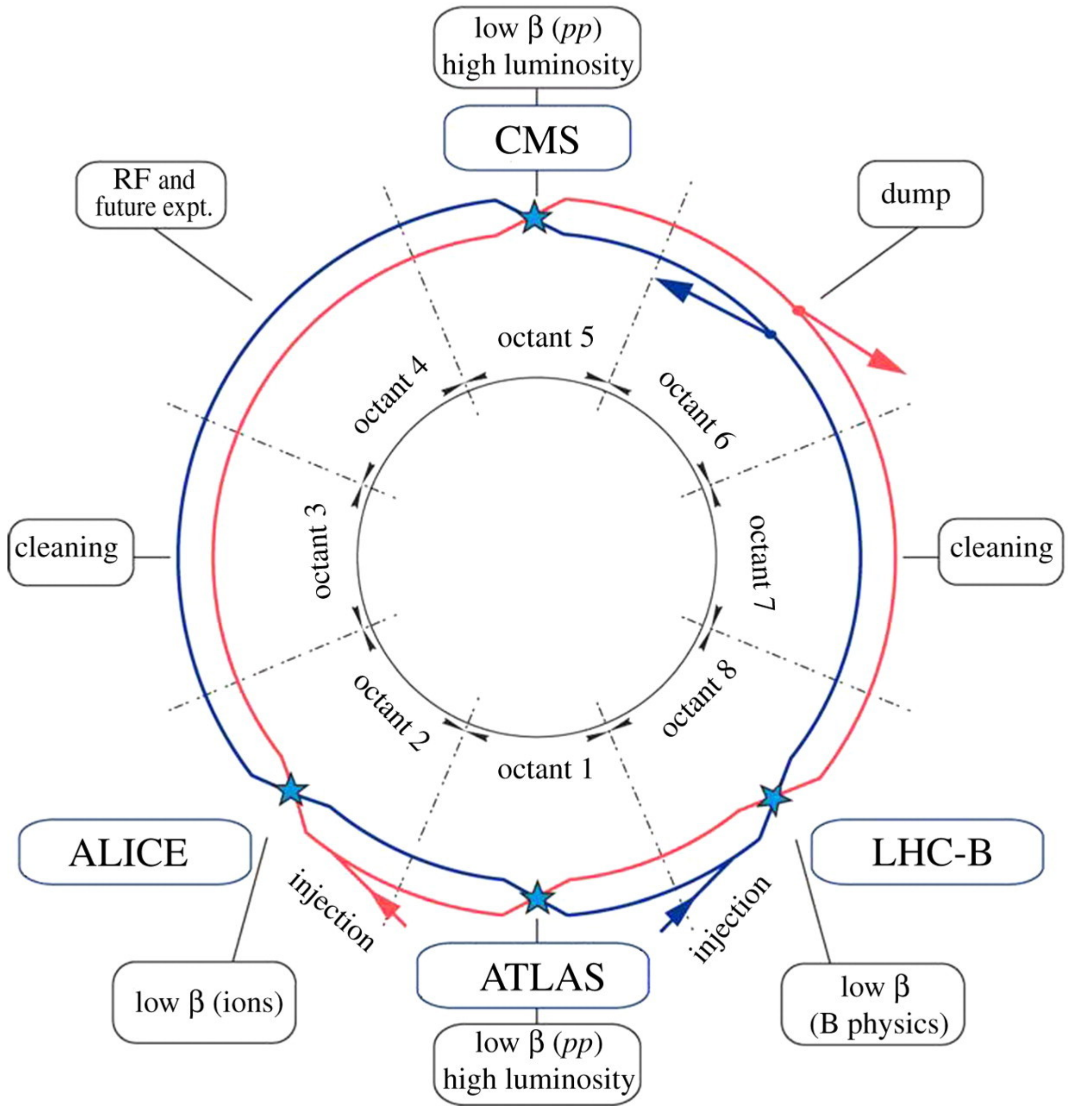

Figure 2-2. The schematic layout of the LHC. Each octant contains a insertion point. Points 1, 2, 5, and 8 are the locations of collision experiments. Points 3 and 7 are for beam collimation. Hadrons are injected at Points 1 and 8, accelerated at Point 4, and eventually discarded at Point 6. Plot taken from Ref. [3].

tions, the magnetic fields for the two beams need to be opposite as well. Given the space limitation in the tunnel and the need to keep the budget down, a "twin-bore" design is adopted, in which the two beam pipes and two sets of magnet coils are installed next to each other in the same piece of mechanic housing, called the cold mass. The cold mass is a cylindrical solid iron structure bored at its center and surrounded by a superfluid helium vessel. Each cold mass has a length of about 15 m, a diameter of about 570 mm,

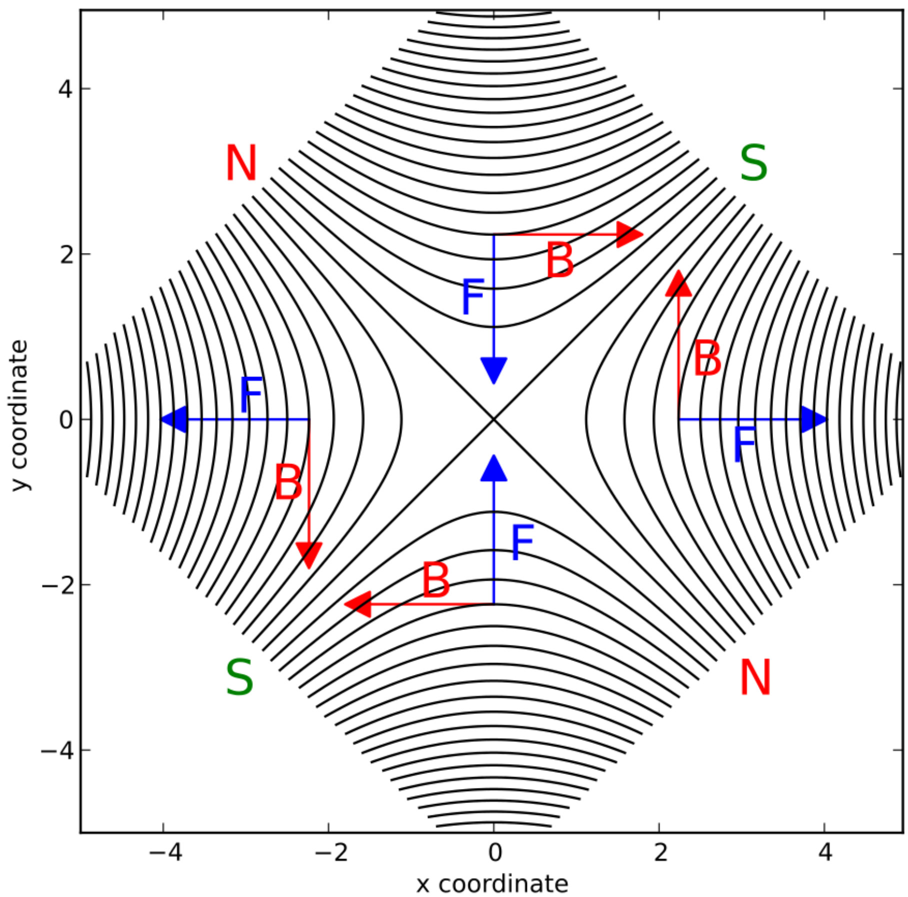

Figure 2-3. Magnetic field of an ideal quadrupole. Plot taken from Ref. [4].

and a mass of about 27.5 t. It provides a stable 1.9 K environment for the magnet coils, and in the meantime serves as their magnetic yoke. The dipoles of LHC are manufactured identically up to a high precision. The relative variation in the magnetic field strength and the field inhomogeneity must not exceed 10^{-4}, The quadrupoles provide gradient fields (shown in Figure 2-3) that squeeze the beam in one direction and disperse it in the other. A few quadrupoles in series, with certain field geometry, can focus or defocus the beams. They keep the beams from dispersing in the beam pipes, focus the beams to high intensity before collisions, and defocus them after collisions. Quadrupoles are also in stationed in twin-bored cold masses, each about 3.1 m long. Several types of small-scale multipole correctors are installed as components of the main dipoles and quadrupoles, which help to fine-tune the beam parameters. The insertion magnets serves various purposes: to adjust the beam parameters to the needs of each dedicated experiment, or to abruptly change the direction of the beam for injection or abortion. Most insertion magnets are based on Nb-Ti superconductors, while some, in radiation areas, are built of normal conducting material. The electric currents in these various magnets range from 60 A (for small correctors) to 12 kA (for main dipoles and quadrupoles), while the total energy stored in the magnets is about 10 GJ during full operations of the LHC.

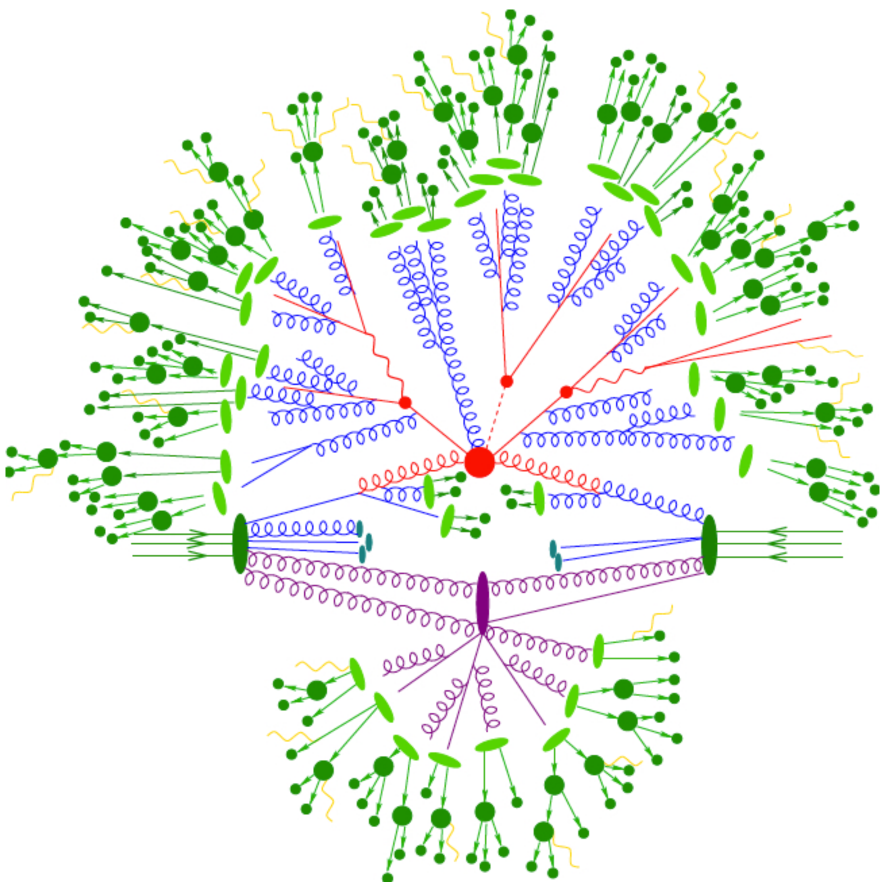

Figure 2-4. An illustration of the interactions in a pp collision. The primary interaction in this example is the Higgs boson production in association with a top quark pair, whose Feynman diagram is shown in 3-2. Plot taken from Ref. [5].

Proton-proton (pp) collisions at the LHC initiate a diverse range of processes. Quarks and gluons, together called partons, in protons can initiate QCD processes, in which a cascade of quarks and gluons are produced, which in turn hadronize and form various hadrons at high multiplicity. Quarks also participate in the electroweak interaction, producing gauge bosons, which may decay to leptons. The Higgs boson can be from quarks and gauge bosons. In pp collisions, partons carry a fraction of the proton energy, following a broad spectrum called the parton distribution function (PDF). As a result, the energy of each interaction can vary in a broad range. Furthermore, protons, compared to antiprotons and positrons, are easy to obtain and accelerate, allowing for collisions at high energy and high luminosity. Overall, pp collisions can generate all physics processes in a wide energy spectrum with a large statistical sample size, making a ideal tool to perform generic searches for expected and unexpected physics processes.

Figure 2-4 demonstrates an example of the interactions initiated in a hard pp scatter instance. The primary interaction in this example is the production of the Higgs boson associated with a top quark pair ($t\bar{t}H$), in which the loopy red lines present the incoming gluons, the big red blob is the vertex of the primary interaction, and the small red blobs are the decay vertices of the Higgs boson and the top (anti-top) quarks. Additional QCD radiations are indicated by the loopy blue lines, which undergo hadronization (light green blobs) and form hadrons (dark green blobs). The hard interaction in this example is accompanied with a softer secondary interaction (purple blob), which produce a bunch of hadrons through QCD processes. Finally, photons (curvy yellow lines) can be emitted from the final state hadrons and leptons.

At the LHC, multiple pp collisions are expected in each proton bunch crossing, known as pileup. In most cases, all of these simultaneous interactions are QCD interactions, while occasionally one of the collisions is a hard scatter that leads to processes interesting to physicists. In those occasions, the collision containing the hard scatter is considered as the primary interaction, and the other collisions are called pileup interaction. Within the primary interaction, the process of interest, for example the $t\bar{t}H$ process in Figure 2-4, is called the prompt interaction, while the other QCD-induced byproducts are called the underlying event.

2.2 The Compact Muon Solenoid experiment

The Compact Muon Solenoid (CMS) [32] is a general purpose detector operating at one of the collision sites of the LHC. It is named after its large-bore superconducting solenoid magnet, which provides a 4 T field at its core and enables precise measurements of the various collision products. The CMS detector has an overall length of 28.7 m, a diameter of 15.0 m and a weight of 14000 t. A cutaway diagram of CMS is shown in Figure 2-5. It consist, from inside to outside, of a silicon-based tracking system (blue slices in the figure), a lead tungstate crystal electromagnetic calorimeter (ECAL) (cyan blocks), a brass-scintillator hadron calorimeter (HCAL) (yellow blocks), a superconducting solenoid (white blocks), and an iron return yoke (red blocks) interleaved with a multi-layer muon detector (white panels).

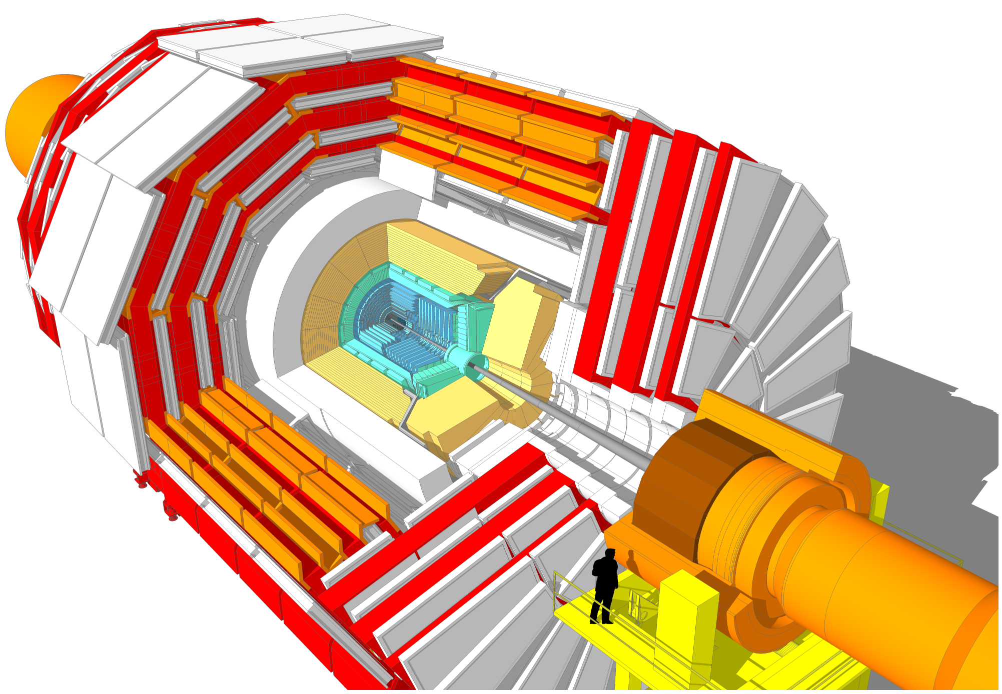

Figure 2-5. A cutaway diagram of the CMS detector. The design is specified to a design stage called the Phase-1 detector upgrade [6, 7, 8]. Plot taken from Ref. [9].

CMS adopts a spherical coordinates convention: the origin is positioned at the geometrical center of CMS expected for collisions to happen; the z axis is along the beam pipe with its positive direction pointing toward the Jura mountain; the $\phi = 0$ direction (or the x axis of the Cartesian coordinates) points horizontally toward ATLAS at the opposite side of the LHC tunnel; this leaves the y axis of the Cartesian coordinates pointing upward to the sky. In addition, the polar angle θ is in most cases replaced by a variable called pseudorapidity η, defined as $\eta = -\ln[\tan(\frac{\theta}{2})]$. The pseudorapidity is a good approximation of the longitudinal rapidity y_L of particles in the CMS frame in the limit of $|\mathbf{p}| \gg m$. The CMS coordinates, along with the $\eta - \theta$ correspondence, are shown in Figure 2-6.

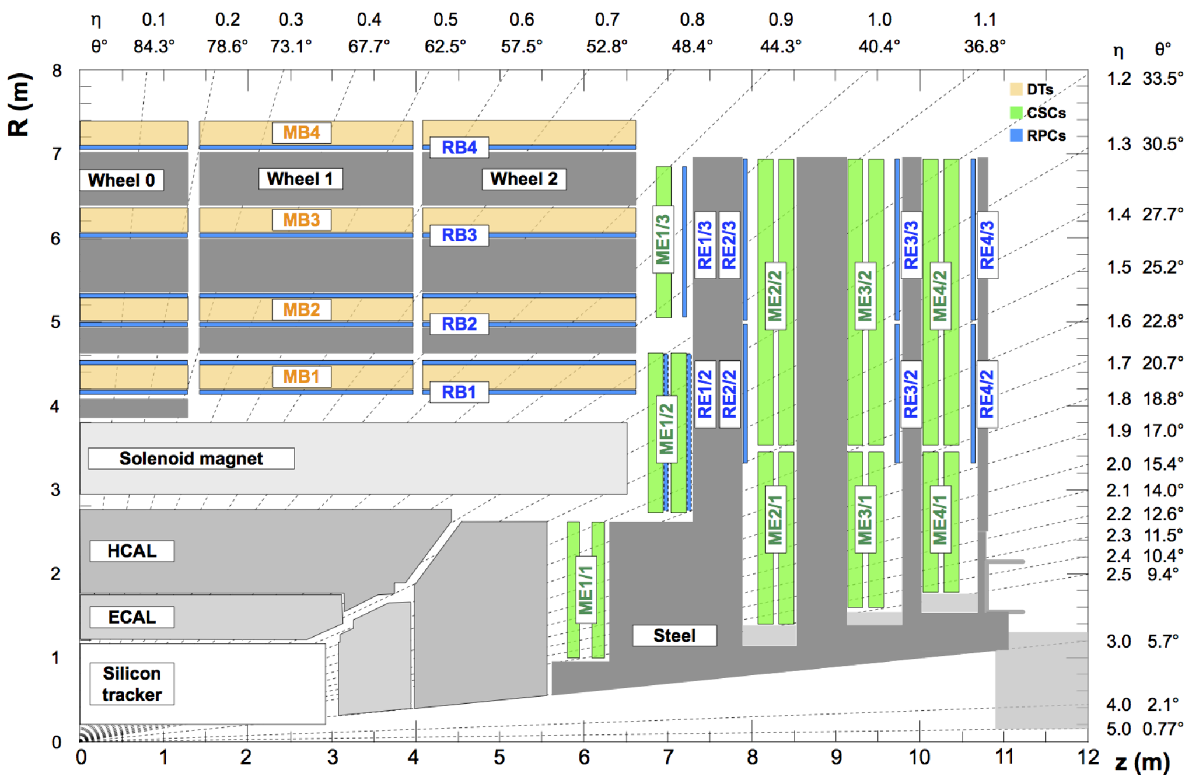

Figure 2-6. A longitudinal section view of the CMS detector, gridded with the CMS coordinates. Plot taken from Ref. [10].

The solenoid magnet of CMS is based on the same material as the LHC magnets, operating also at 1.9 K. During its full operation, the superconducting coil carries an electric current of 18500 A and stores an energy of 2.6 GJ. It generates a homogeneous 4 T field inside its bore of 6-m diameter and 12.5-m length, providing the functioning environment for the detector components installed inside of it. The superconducting coil is enclosed by its iron yoke, which is the heaviest part of the CMS detector, weighing about 12000 t, almost twice as much iron in the Eiffel Tower. The iron yoke guides the magnetic field outside of the coil, and in the meantime serves as the supporting frame for all other CMS detector components. Figure 2-7 shows the operating magnetic field of CMS.

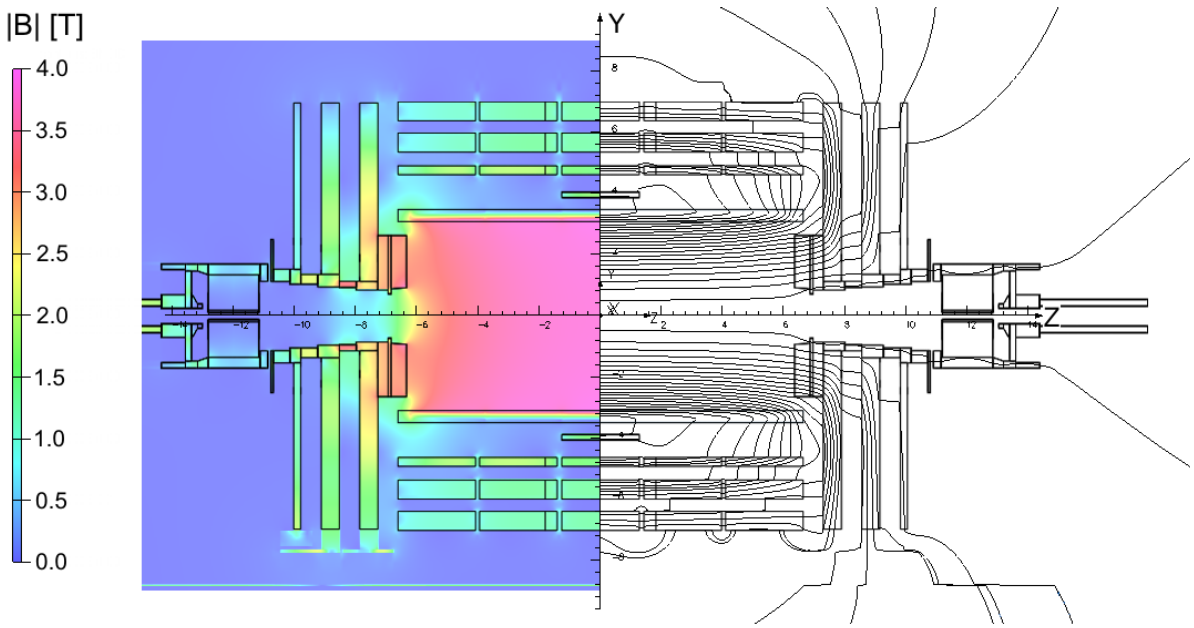

Figure 2-7. The magnetic field in CMS displayed in a longitudinal section, operating with a central field strength of 3.8 T. The field value $|B|$ is shown on the left and the field lines are shown on the right. Plot taken from Ref. [11].

The CMS inner tracker is designed to provide a precise and efficient measurement of the trajectories of charged particles emerging from the LHC collisions. It is laid out in a cylindrical volume of 5.8-m length and 2.5-m diameter surrounding the beam pipe, shown in Figure 2-8. It is composed of a pixel detector with four barrel layers at radii of 2.9 cm, 6.8 cm, 10.9 cm, and 16.0 cm [12], and a silicon strip detector with 4 + 6 barrel layers extending to a radius of 1.1 m [32]. Each system is completed by endcaps which consist of three disks in the pixel detector and 3 + 9 disks in the strip detector. The CMS tracker has about 124 million pixels channels and about 9.3 million strip channels in total, and provides its full tracking ability up to a pseudorapidity range of $|\eta| < 2.5$.

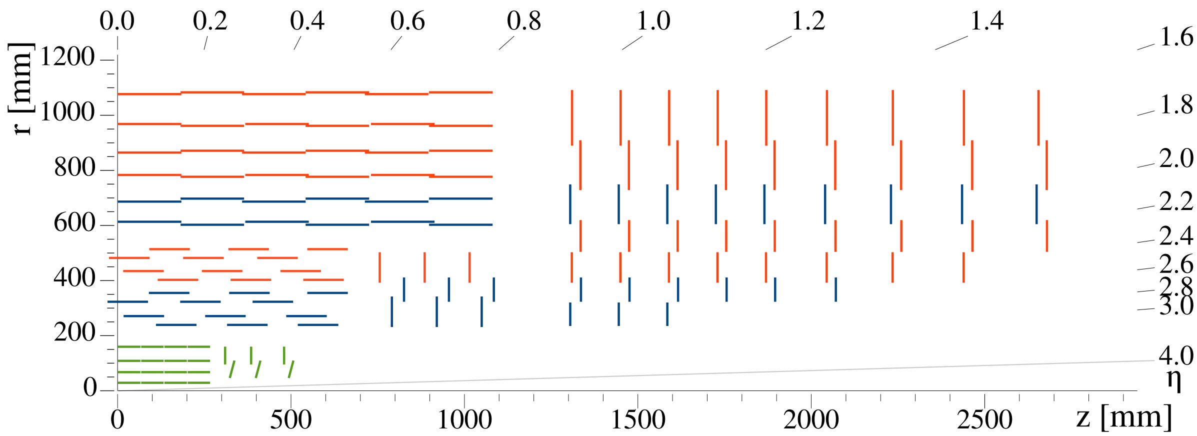

Figure 2-8. Sketch of one quarter of the Phase-1 CMS tracking system in r-z view. The pixel detectors are shown in green, while single-sided and double-sided strip modules are depicted as red and blue segments, respectively. Plot taken from Ref. [12].

In the pixel detector, the standard pixel size is 100×150 μm^2 in $r\phi \times z$ plane, with a thickness of 285 μm. At the nominal LHC luminosity, about 1000 charged particles are produced in each bunch crossing, corresponding to a hit occupancy of the order 10^{-4} per pixel per bunch crossing.

At its operation, a charged particle usually generate signals in a few neighboring pixels, known as the charge-sharing. The pixel system reads with analog pulse height read-out, which enables an interpolation between the neighboring pixels and achieves a spatial resolution in the range of 15-20 μm.

The strip detector is made up of two subsystems in two regions, the inner region ($20\,\text{cm} < r < 55\,\text{cm}$) and the out region ($55\,\text{cm} < r < 110\,\text{cm}$), both composed of silicon micro-strip detectors. A typical micro-strip cell in the inner region has a thickness of 320 μm and size of 10 cm $\times$ 80 μm, leading to an occupancy of of up to 2-3% per strip per LHC bunch crossing. Micro-strip cells in the outer region, given the larger radii and reduced particle density, are larger in size: 500 μm in thickness and up to about $25\,\text{cm} \times 180\,\mu$m in size, and corresponding to an occupancy of about 1%. The spatial resolution of the strip cells, after the interpolation of charge-sharing, ranges from 23-35 μm in the inner barrel layers, and from 35-53 μm in the outer barrel layers.

All strip cells are placed parallel to the beam pipe in the barrel, and along the radial direction in the endcaps. To provide a measurement of the coordinate along the strip length (z in the barrel and r in the endcaps), some layers of the strip detector are constructed with a double-strip design, in which a second micro-strip detector module is mounted back-to-back to each original strip module with a stereo angle of 100 mrad. This measurement achieves a resolution of 230 μm in the inner barrel and 530 μm in the outer barrel, while the resolution varies in the endcap disks depending on the hit location.

The whole tracking system, consisting of the numerous silicon sensors and their readout system, consumes about 60 kW of electric power, which in turn is dissipated as heat in the tracker volume. A cooling system is built to maintain its operation temperature of -10 $^{\circ}$C, in which the pixel layers are cooled with aluminum conducting tubes, and the strip layers are cooled with a continuous flow of C_6F_{14} liquid.

CHAPTER 3
OVERVIEW OF THE SEARCH OF $\mathrm{H} \to \mu\mu$ DECAY AT CMS

In 2012, a new boson at 125 GeV was discovered by ATLAS and CMS at the LHC [16, 17, 18]. Various measurements have been performed to probe the properties of this boson ever since, and the boson was later acknowledged as the Higgs boson predicted by the SM. Up to now, the couplings between the Higgs boson and the electroweak (EW) gauge bosons have been observed to be consistent with the SM prediction, while the Yukawa couplings between the Higgs boson and the fermions have only been established for the third generation fermions. The first and second generation fermions are less massive than their third generation counterparts and thus weaker coupling to the Higgs boson, as the coupling strength is proportional to the mass of the fermion. This leads to significantly smaller branching fractions of the decay modes of the Higgs boson to the first or second generation fermions, and poses a substantial challenge to the searches for such decays. The $\mathrm{H} \to \mu\mu$ decay in particular, has a branching ratio of $\mathscr{B}(\mathrm{H} \to \mu\mu) = 2.18 \times 10^{-4}$, which corresponds to an expectation of about 1000 event instances in all the data collected by CMS from 2016 to 2018 (called the LHC Run 2 data-taking period). In contrast, these 1000 so-called signal events are engulfed by millions of events produced through other processes (background events) that mimic their experimental signature. The search for the $\mathrm{H} \to \mu\mu$ decay, in a nutshell, is a struggle to make the signal events stand out from the vast backgrounds with statistical significance.

The search for the $\mathrm{H} \to \mu\mu$ decay has been conducted using proton-proton (pp) collision data collected at center-of-mass energies of 7, 8, and 13 TeV by the CMS Collaboration [33, 34] and the ATLAS Collaboration [35, 36, 37]. The latest result [34] from CMS prior to this work reported an observed (expected in absence of $\mathrm{H} \to \mu\mu$ decay) upper limit of 2.9 (2.2) times the SM prediction of the Higgs boson production and the $\mathscr{B}(\mathrm{H} \to \mu\mu)$, at the 95% confidence level (CL).

Despite the challenging nature of the $\mathrm{H} \to \mu\mu$ analysis, many efforts can be made to improve the separation of signal and background processes, allowing for a sizable refinement of the result. First of all, the Higgs boson has a narrow natural width, and the muons are well identified objects in the CMS detector. This means that the two muons from the Higgs decay always compose an invariant mass near the nominal Higgs mass, 125 GeV. While for the background processes, the muons are created either by the decay of a Z boson, or by decays of multiple particles, for example a t and $\bar{t}$ quark pair, each resulting in a single muon. The Z boson has a mean mass at 91.2 GeV and a natural width of 2.5 GeV, making a slowly falling tail in the mass spectrum around 125 GeV. For the muons that come from two different sources, their invariant mass follows a flat random distribution near the mass range of interest. Therefore, the signal can be strongly distinguished against the background in the dimuon invariant mass spectrum, as a sharp peak against a smooth falling shape. Figure 3-1 shows the conceptual shape of these mass spectra.

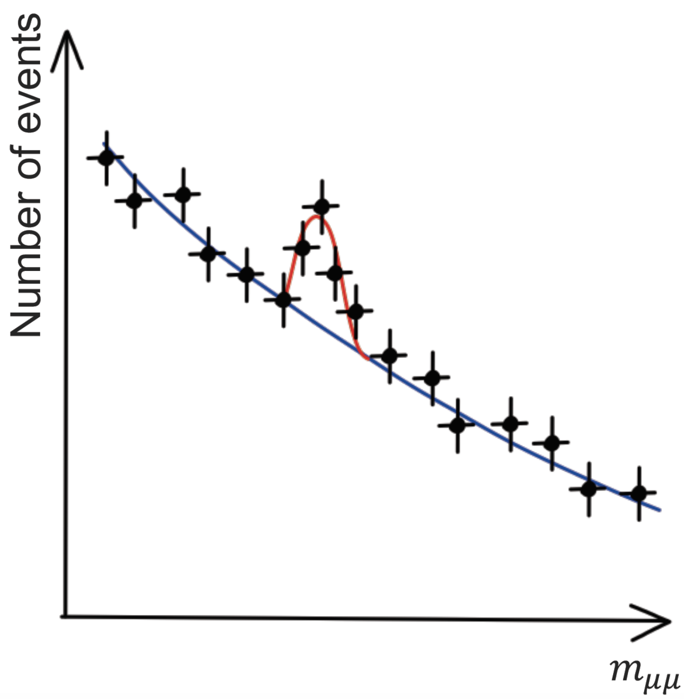

Figure 3-1. A conceptual plot for the dimuon mass shapes for the signal and the background. The blue line shows the expected background shape, while the red line shows the expected signal shape on top of it.

Furthermore, the Higgs boson is produced via several distinct production modes, each with some unique kinematic characteristics. By applying selection criteria targeting a certain signal production mode, it is possible to select a specific part of the kinematic phase space that is enriched with that signal, and reject many background processes that do not share the same kinematic features. There are four main production modes considered in this analysis, ordered by their production cross sections: gluon fusion (ggH), vector boson fusion (VBF or qqH), associated production with a weak vector boson (VH), and associated production with a pair of top quarks ($t\bar{t}H$). The Feynman diagrams for these main production modes are shown in Figure 3-2. Some other minor production modes are also considered as signal contributions, including associated production with a pair of bottom quarks ($b\bar{b}H$), associated production with a Z boson through gluon fusion (ggZH), associated production with a top quark and a W boson (tHW), and associated production with a top quark and a light quark (tHq). The Feynman diagrams for these minor production modes are shown in Figure 3-3. Table 3-1 summarizes the cross sections for all these production modes, along with the expected number of events in the Run 2 dataset (137 fb^{-1}).

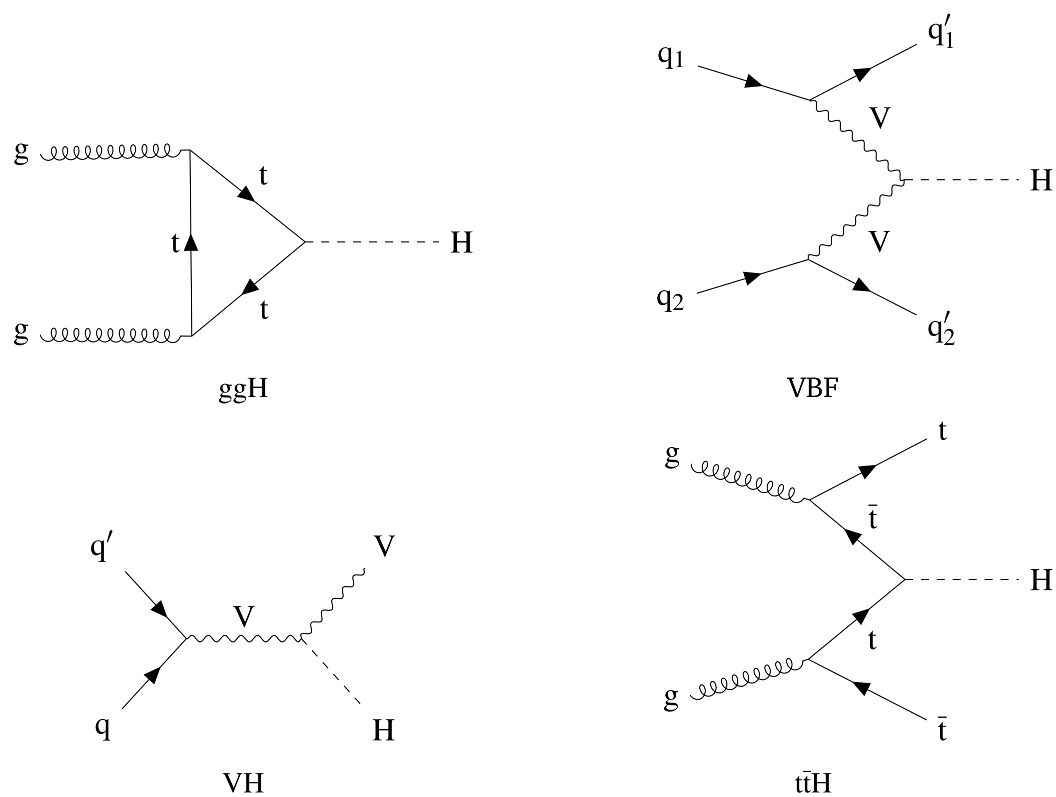

Figure 3-2. Main production modes of the Higgs boson.

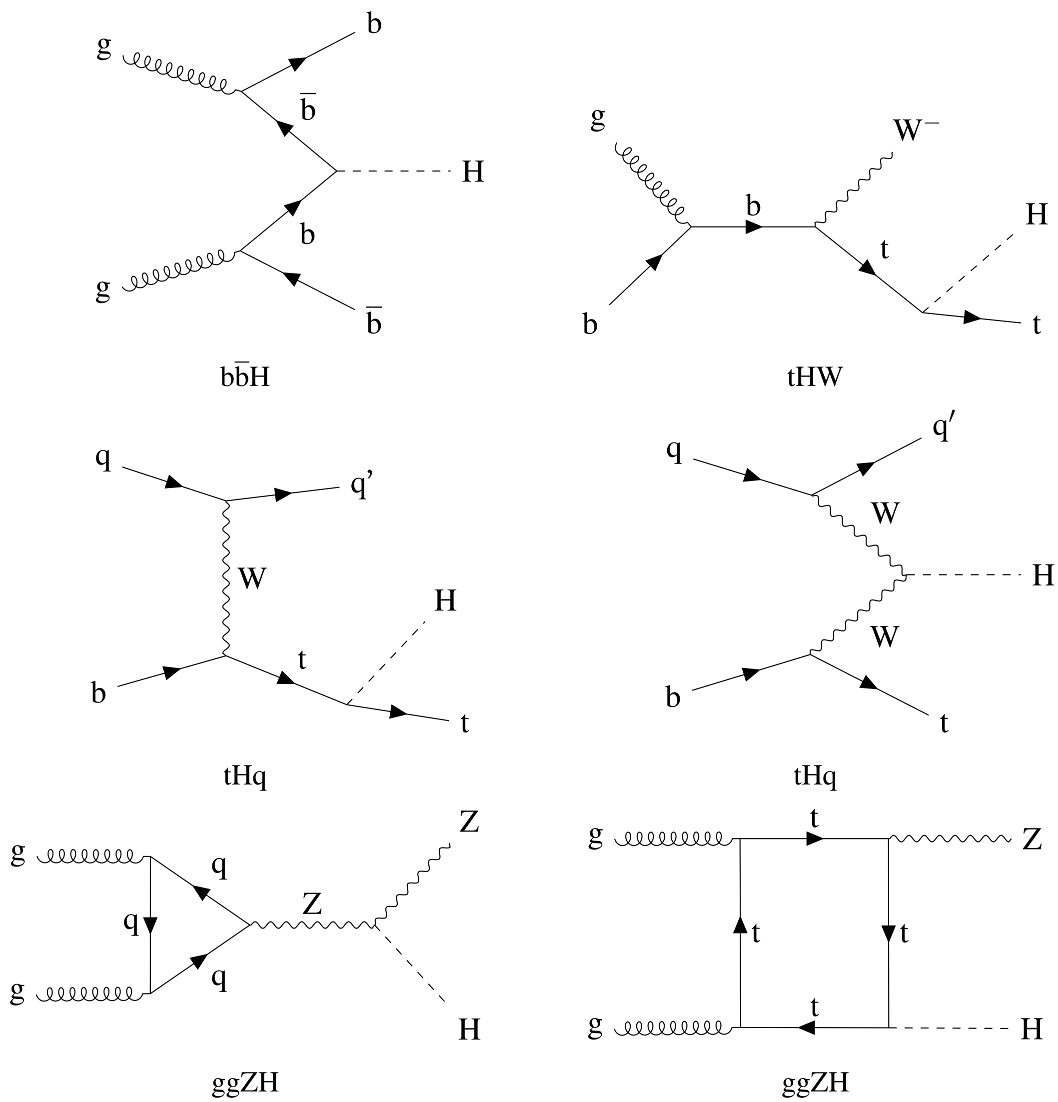

Figure 3-3. Examples of minor Higgs production modes.

Four event categories are defined in this analysis targeting each of the four main Higgs production modes, all of them requiring two oppositely charged (OS) muons that form a candidate for the Higgs boson decay. The additional requirements for each category are: the $t\bar{t}H$ category requires the presence of additional b-jets (from the decay of the top quarks) in the event, the VH category targets events with additional leptons (e or μ, from the decay of the vector boson), the VBF category selects events with two energetic and forward jets, while the ggH category does not specify additional objects, and collects all events that are not selected by the other three categories. No dedicated category is made

Table 3-1. Production modes of the Higgs boson in pp collisions at the LHC, their cross sections for $m_{\mathrm{H}} = 125\mathrm{GeV}$, and the corresponding expected number of events in the dataset for this analysis (the cross sections multiplying $\mathscr{B}(\mathrm{H} \to \mu\mu)$ and the integrated luminosity ($137\mathrm{fb}^{-1}$). The leptons (ℓ) in the table refer to electrons or muons.

signal mode	decay mode	Cross section (pb)	Expected number of events
ggH	inclusive	48.58	1450
VBF	inclusive	3.782	113
WH	inclusive	1.373	41.0
	$\mathrm{W} \to \ell\nu$	0.293	8.75
$\mathrm{qq} \to \mathrm{ZH}$	inclusive	0.761	22.7
	$\mathrm{Z} \to \ell\ell$	0.051	1.53
ggZH	inclusive	0.123	3.67
	$\mathrm{Z} \to \ell\ell$	0.008	0.25
$\mathrm{t\bar{t}H}$	inclusive	0.507	15.1
	≥ 1 $\mathrm{t} \to$ leptons	0.193	5.76
	Both $\mathrm{t} \to$ hadrons	0.230	6.86
sum of above	inclusive	55.13	1646
$\mathrm{b\bar{b}H}$	inclusive	0.488	14.6
tHq	inclusive	0.074	2.21
tHW	inclusive	0.015	0.45
sum of all	inclusive	55.70	1663

for the minor signal modes, either because they have very similar features to one of the main modes, or because their cross sections are much smaller than the main modes and do not make a difference.

With such selections, naturally, each of the selected phase spaces presents a distinct event topology and contains a distinct background composition. Therefore, the analysis is performed independently in each of the event categories, following different optimized strategies. The detailed description of the analysis strategies in each event category is given in Section 3.2.

3.1 Data and simulation samples

This analysis uses the proton-proton collision data collected by the CMS detector during Run 2, which corresponds to a total integrated luminosity of $137.2\mathrm{fb}^{-1}$.

The triggers used in this analysis are the single muon triggers, which impose some loose isolation requirements and a p_{T} threshold on the HLT muon candidates. The p_{T}

cut is 27 (24) GeV for data collected in 2017 (2016, 2018). For the muons selected in this analysis, as explained in Chapter 4, the efficiencies of these triggers are above 95%, making the selection efficiency for the events with two muons close to 100%.

Simulated events from the Monte Carlo (MC) event generators for the signal and the dominant background processes are used to optimize the analysis strategy and assess the systematics uncertainties. The generated events are processed through a detailed simulation of the CMS detector based on GEANT4 [38] and are reconstructed with the same algorithms that are used for data. All MC samples except the EW $Z + jj$ samples use PYTHIA 8.2 [39] to model the parton showering (PS), hadronization, and the underlying event (UE), while the EW $Z + jj$ samples use HERWIG++ and HERWIG7 [40] for the same purpose. The effect of pileup interactions is modelled by overlaying simulated inelastic pp collisions on the hard-scattering event.

3.1.1 The simulation of the signal processes

The ggH signal process is simulated at next-to-leading order (NLO) accuracy in perturbative QCD, using both the MADGRAPH5_aMC@NLO v2.4.2 [41] and POWHEG v2.0 [42, 43, 44, 45] MC event generators. The p_T distribution of the Higgs boson in ggH process is then reweighted to match the POWHEG NNLOPS prediction [46, 47]. The VBF, WH, qqZH, and $\mathrm{t\bar{t}H}$ processes are simulated with POWHEG v2.0 [48, 49, 50] at NLO precision in QCD. The $\mathrm{b\bar{b}H}$ process is simulated at NLO precision in QCD with POWHEG. the tHq, and tHW processes are generated at leading order (LO) with the MADGRAPH5_aMC@NLO generator. The ggZH process is simulated at LO with the POWHEG generator. Simulated signal events are generated, for each production mode, at m_H values of 120, 125, 130 GeV. A table summarizing the simulation for signals is shown in Table 3-2.

Expected signal yields are normalized to the production cross sections and $\mathscr{B}(H \to \mu\mu)$ values taken from the recommendations of LHC Yellow Report [51]. The ggH production cross section is computed at next-to-next-to-NLO (N3LO) precision in QCD, and at NLO in EW theory [52]. The cross section of Higgs boson production in the VBF [53] and

Table 3-2. Summary of the specification for the simulated Higgs signal samples.

Sample	Generator (Perturbative order)	Parton Shower	Cross section	Additional corrections
ggH	MadGraph5_aMC@NLO (NLO QCD)	PYTHIA	N3LO QCD, NLO EW	p_T(H) from NNLOPS
VBF	POWHEG (NLO QCD)	PYTHIA dipole shower	NNLO QCD, NLO EW	-
qq $\rightarrow$ VH	POWHEG (NLO QCD)	PYTHIA	NNLO QCD, NLO EW	-
ggZH	POWHEG (LO)	PYTHIA	NNLO QCD, NLO EW	-
$t\bar{t}$H	POWHEG (NLO QCD)	PYTHIA	NLO QCD, NLO EW	-
$b\bar{b}$H	POWHEG (NLO QCD)	PYTHIA	NLO QCD	-
tHq	MadGraph5_aMC@NLO (LO)	PYTHIA	NLO QCD	-
tHW	MadGraph5_aMC@NLO (LO)	PYTHIA	NLO QCD	-

qq $\rightarrow$ VH [54] modes is calculated at next-to-NLO (NNLO) in QCD, including NLO EW corrections, while the $t\bar{t}$H cross section is computed at NLO in QCD and EW theory [55, 56]. The $b\bar{b}$H, tHq, and tHW cross sections are computed at NLO in QCD without including higher-order EW corrections [51, 57, 58]. The H $\rightarrow \mu\mu$ partial width is computed with HDECAY [59, 60] at NLO in QCD and EW theory.

3.1.2 The simulation of the background processes

The background is modeled considering various SM processes, summarized in Table 3-3. The main background in the ggH and VBF categories is the DY process, which is simulated at NLO in QCD using the MadGraph5_aMC@NLO generator. The corresponding cross section is calculated with FEWZ v3.1b2 [61] at NNLO in QCD and NLO accuracy in EW theory. The EW production of a Z boson in association with two jets ($\mathrm{Z}+jj$) is an important background in the VBF category. This process is simulated at LO using the MadGraph5_aMC@NLO v2.6.5 generator. The WZ, $q\bar{q} \rightarrow$ ZZ, and WW processes, which constitute the main backgrounds in the VH category, are simulated at NLO in QCD using either the POWHEG or MadGraph5_aMC@NLO generators. Their production cross sections are corrected with the NNLO/NLO K factors taken from Refs. [62], [63], and [64]. The gluon-initiated loop-induced ZZ process (ggZZ) is simulated with the MCFM v7.0 generator [65] at LO and the corresponding production cross section is corrected to match higher-order QCD predictions, following the strategy detailed in Ref. [22]. Minor contributions from triboson processes (WWW, WWZ, WZZ, and ZZZ) are also taken into account and are simulated at NLO in QCD using the MadGraph5_aMC@NLO generator.

The main backgrounds in the $t\bar{t}$H category involve the production of top quarks. The $t\bar{t}$ background is simulated with NLO precision in QCD using the POWHEG generator, and its cross section is obtained from the TOP++ v2.0 [66] prediction that includes NNLO corrections in QCD and resummation of next-to-next-to-leading logarithmic (NNLL) soft gluon terms. The single top quark processes are simulated at NLO in QCD via either POWHEG or MADGRAPH5_aMC@NLO and their cross sections are computed, at the same order of precision, using HATHOR [67]. Finally, contributions from the $t\bar{t}$Z, $t\bar{t}$W, $t\bar{t}$WW, $t\bar{t}t\bar{t}$, and tZq processes are also considered and are simulated using the MADGRAPH5_aMC@NLO generator at NLO precision in QCD. For the simulated samples corresponding to the 2016 (2017–2018) data-taking periods, the NNPDF v3.0 (v3.1) NLO (NNLO) parton distribution functions (PDFs) are used [68, 69]. For processes simulated at NLO (LO) in QCD with the MADGRAPH5_aMC@NLO generator, events from the matrix element (ME) characterized by different parton multiplicities are merged via the FxFx (MLM) prescription [70, 71].

Table 3-3. Summary of the specification for the simulated background samples.

Sample	Generator (Perturbative order)	Parton Shower	Cross section	Additional corrections
Drell-Yan	MADGRAPH5_aMC@NLO (NLO QCD)	PYTHIA	NNLO QCD, NLO EW	-
Zjj-EW	MADGRAPH5_aMC@NLO (LO)	HERWIG++/HERWIG7	LO	-
$t\bar{t}$	POWHEG (NLO QCD)	PYTHIA	NNLO QCD	-
Single top quark	POWHEG/MADGRAPH5_aMC@NLO (NLO QCD)	PYTHIA	NLO QCD	-
Diboson (VV)	POWHEG/MADGRAPH5_aMC@NLO (NLO QCD)	PYTHIA	NLO QCD	NNLO/NLO K factors
ggZZ	MCFM (LO)	PYTHIA	LO	NNLO/LO K factors
$t\bar{t}$V, $t\bar{t}$VV	MADGRAPH5_aMC@NLO (NLO QCD)	PYTHIA	NLO QCD	-
Triboson (VVV)	MADGRAPH5_aMC@NLO (LO)	PYTHIA	NLO QCD	-

3.2 Exclusive analyses and their strategies

In order to maximally harness the kinematic features in the different production modes of the Higgs boson, the analysis is conducted in four independent event categories: the ggH, VBF, VH and $t\bar{t}$H categories. The workflow to divide events into different categories is shown in Figure 3-4. As a common prerequisite in this analysis, all events should contain two opposite-charged (or opposite-sign, OS) muons that make the candidate for the Higgs boson decay. Then, as a first step, events containing b-tagged jets (either one medium tag or two loose tag of the DeepCSV [72] working points) are classified into the $t\bar{t}$H category. The $t\bar{t}$H category is further divided into the $t\bar{t}$H leptonic category and the

$t\bar{t}H$ hadronic category depending on whether the event contains electrons or additional muons (leptonic category), or whether it contains at least three jets (hadronic category). Some events containing b-tagged jets may not pass the secondary selections for either the leptonic or hadronic $t\bar{t}H$ categories. They are most likely background events, and are therefore discarded. The events without b-tagged jets, fall into the VH category if they contain additional leptons (electrons or muons). Inside the VH category, events are further tagged as WH events if there is one and only one extra lepton in the event, or tagged as ZH events if there are two same-flavor opposite-sign (SFOS) extra leptons. A small collection of events may pass the primary VH selection but fail the secondary WH or ZH selections, for example events that contain one extra electron and one extra muon. These events are most likely not from the signal processes, and are discarded. For the events with neither b-tagged jets nor additional leptons, if there are at least two energetic jets, composing a jet pair with $m_{\mathrm{jj}} > 400\mathrm{GeV}$ and $\Delta\eta_{\mathrm{jj}} > 2.5$, the events are tagged as the VBF events. Finally, the ggH category collects all events that are not assigned to other categories. Most events in the ggH category are profiled to have either no additional objects or just one additional jet other than the Higgs candidate muons. The detailed definition of the different objects used in this categorization is given in Chapter 4.

The analysis is performed independently in each event category. Since these categories have distinct profiles in the expected signal yield, the signal purity, and the background composition, the optimal approaches to perform the analyses are also different. As a result, two different strategies to perform the analysis are considered:

- **Data-driven parametric fit to the $m_{\mu\mu}$ spectrum:** As is done in the previously published analyses on the the data collected prior to 2017 [33, 34], a multivariate analysis (MVA) method is used to profile the separation between the signal and the background processes. The MVA can be either cut-based as in the Run 1 analysis [33], or machine learning (ML) based as in the analysis on the 2016 data [34]. The MVA considers the kinematic information that is uncorrelated with the $m_{\mu\mu}$, and is used to divide the events into several regions with different signal-to-background-ratios (S/B), called the MVA-categories. In each MVA-category, the signal strength is evaluated from fits to the $m_{\mu\mu}$ spectrum in data, in what is called the *signal fit region*, for example $110 < m_{\mu\mu} < 150\mathrm{GeV}$. Both the signal and the background are

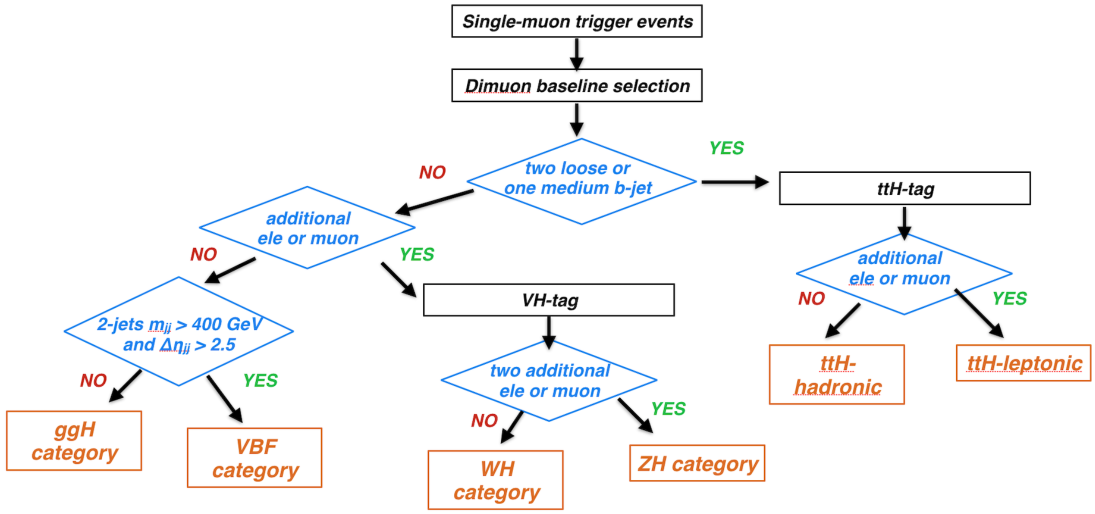

Figure 3-4. Scheme of the procedure of assigning events to different categories. All events passing the common baseline selection are divided into four mutually exclusive categories: ggH, VBF, VH (WH and ZH), and $t\bar{t}$H (leptonic and hadronic).

modeled by parametric functions that are carefully studied to provide a truthful description of the distributions of physics processes. The total yield of the background is unconstrained in the fit and is determined entirely by the data. The effects of the systematic uncertainties from various sources on either the signal yield or the signal shape are assessed and propagated to the fit result. The systematic uncertainties do not affect the background estimation since it is based on data rather than predictions from simulations.

- **MC-based template fit to the Neural Network discriminator:** This approach is also based on an MVA, for which a ML algorithm, Deep Neural Network (DNN), is taken. The DNN takes all the kinematic variables *including* $m_{\mu\mu}$, and profiles the discrimination between the signal and the background. Without making further categories, the binned template of the DNN output in the whole phase space is used for the signal strength evaluation. Since the fit is applied to the DNN output rather than the $m_{\mu\mu}$ distribution, the *signal fit region* is further divided into two parts: the *signal region*, $115 < m_{\mu\mu} < 135$ GeV, and the *sideband region*, $110 < m_{\mu\mu} < 115$ GeV or $135 < m_{\mu\mu} < 150$ GeV. The data are fit simultaneously in both regions using the DNN templates of the signal and background simulation. The systematic uncertainties affect both the signal and the background prediction, and are employed as variations in either the yield or the shape of the templates. The background yield is estimated from simulation and is allowed to vary within its uncertainty in the fit, in the same manner as the other systematic uncertainties. The signal strength is extracted from the fit in the *signal region*. The *sideband region* does not contain any signal contribution, but is nonetheless used in the fit, to enhance the constraint on the background estimation.

These two strategies should give comparable results in the ideal case, where there are abundant statistics in both data and simulation, and where the data are well described by simulation. However these conditions are usually not met in real analyses, and one strategy may become preferable over the other. The pp collision is a very noisy environment, making it difficult to achieve an accurate modeling of many kinematic aspects, for example the pile-up events, the parton shower, and the production of leptons through bottom or charm quarks (non-prompt leptons). The modeling of these features usually involves extensive work in the validation of simulated samples, and is generally associated with large systematic uncertainties. In the scenarios where the MC does not model the data very well, or where the uncertainties from MC modeling are not much smaller than the statistical uncertainty in the data, it is more advantageous to follow the data-driven approach. On the other hand, if a phase space lacks enough statistics in data but can be well described by the MC, it is more beneficial to perform a MC-based analysis there.

The ggH category contains the majority of the events in the $\mathrm{H} \to \mu\mu$ analysis, and has very low S/B. In all its MVA-based sub-categories, there are abundant data that the statistical uncertainty of data is smaller than the systematic uncertainties of the background prediction from simulation. Therefore the data-driven strategy is taken in the analysis in the ggH category. The VBF category is featured with a good amount of events, although much less than the ggH category, and a good S/B. This makes it possible to enhance the sensitivity of the analysis by picking very high S/B regions with the help of MVA discriminators. Naturally, the number of events in the high S/B regions is very low. Therefore the MC-based strategy is used in the VBF category. The VH and the $\mathrm{t\bar{t}H}$ categories both have very few events, but high S/B, which seems like a good playground for the MC-based approach. However, one of the main backgrounds in the VH and $\mathrm{t\bar{t}H}$ categories involves extra lepton(s) from non-prompt sources, and lacks accurate MC modeling. Moreover, the expected signal yields in these categories are low. It is impractical to make DNN templates with many bins, otherwise only a small fraction of one data event is expected in each bin.

Given the dataset used in this analysis, the data-driven method is the preferred choice in both the VH and the $\mathrm{t\bar{t}H}$ categories. Overall, the ggH, VH, and $\mathrm{t\bar{t}H}$ categories follow the data-driven strategy, while the VBF category takes the MC-based approach.

More details of the analysis strategy can be found in the paper describing this analysis [15], recently submitted for publication by CMS. The following chapters will cover the object definition and the muon corrections that are common to the whole analysis, then the detailed steps of the analysis in the VH category, and finally the results of both the VH category and of the combination of all four categories.

CHAPTER 4
OBJECT RECONSTRUCTION AND IDENTIFICATION

In CMS, physics objects such as electrons, muons, taus, photons, and hadrons can leave different signals in multiple detector components. An illustration of how different particles interact with the CMS detector is shown in Figure 4-1. As various particles are produced by pp collisions in each event, the reconstruction of them requires a holistic processing of the information from all parts of the detector. This is achieved by the particle-flow (PF) algorithm [73], which combines all detector signals per event and finds the optimal identification and reconstruction of individual particles (PF candidates). Properties of each PF candidate are calibrated centrally by CMS and provided to the analyzers. The selection of each type of physics object is optimized by the analyzers based the characteristics of their analyses.

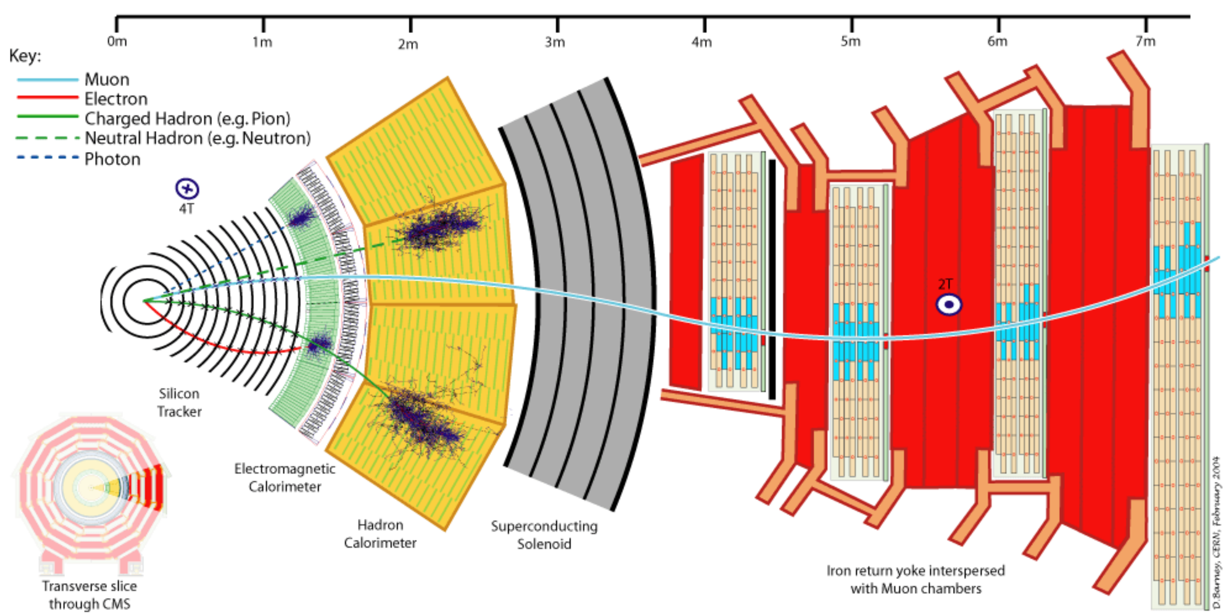

Figure 4-1. A transverse view of the CMS detector layout in the barrel region, with illustrations of the interactions between different particles and different detector components. Plot taken from Ref. [13].

Section 4.1 gives a brief description of the reconstruction sequence for different particles. Section 4.2 lists the selection criteria for different objects adopted in the $\mathrm{H} \to \mu\mu$ analysis.

4.1 CMS object reconstruction

In pp collisions in CMS, final-state particles are produced at the beam interaction region. As they travel outward, they first enter the tracker system, in which the trajectories of charged particles (electrons, muons, and charged hadrons) bend in a strong uniform magnetic field and leave hits in the tracker layers. Passing the tracker, electrons and photons are absorbed in the ECAL, which in turn yields the measurements of their position and energy. Hadrons may leave energy deposits in the ECAL as well, but can only be fully absorbed in the HCAL encircling the ECAL. Muons and neutrinos pass the calorimeters and the superconducting magnet with little or no interactions. Muons then bend and leave hits in the muon detectors outside of the magnet, while neutrinos escape all detector layers without leaving any electronic signal. A graphical summary of these interactions is given in Figure 4-1.

The PF algorithm combines all detector signals described above and attains a global determination of the final-state particles, along with the measurements of their properties. Particles are identified and reconstructed in a sequential manner in PF and are described accordingly in the following sections: tracks of charged particles are first build based on the tracker hits (Section 4.1.1); vertices are reconstructed from groups of compatible tracks (Section 4.1.2); the interaction region is profiled by putting many vertices together (Section 4.1.3); muons and electrons are identified by associating tracks to signals in either the muon chambers or the ECAL (Section 4.1.4 and 4.1.5); hadrons and photons are reconstructed by combining measurements from ECAL, HCAL, with unmatched tracks (Section 4.1.6 and 4.1.7); muons, electrons, hadrons, and photons are all single final-state particles called PF candidates, which can be encapsulated as jets or hadronic decays of τ leptons; and finally, the missing transverse momentum ($E_{\mathrm{T}}^{\mathrm{miss}}$) is defined as the negative of the vectorial sum of all PF candidates, indicating the presence of neutrinos from the collision (Section 4.1.8).

4.1.1 Tracks

Tracks are the best measured objects in CMS and are the foundation of the reconstruction of various particles. Any charged particle can leave hits in the tracking system and can be reconstructed as a track. Tracks can later be linked to signals in the muons detectors and identified as a muon, or be linked to energy deposits in the ECAL and identified as an electron, or be linked to energy deposits in the HCAL and identified as a charged hadron. A ensemble of tracks can also provide information on the interaction vertices, opening the possibility to identify colliding point, converted photons, secondary decays of b quarks and τ leptons, and unexpected long-lived particles (LLPs).

In a typical pp event at CMS during the 2016-2018 data-taking period, where the center-of-mass energy is 13 TeV and the pileup averages about 34, order of a thousand tracks are produced by the collisions, leaving numerous hits in the tracking layers. In order to correctly sew these hits into tracks, a track finder based on a combinatorial Kalman filter (KF) [74] is applied:

- Initial seeds are generated with a few hits compatible with a charged particle trajectory.
- For each seed trajectory, the next layer is surveyed for hits compatible with the seed. A new trajectory candidate is generated for each possible new hit association, with the trajectory quality updated based on the compatibility.
- This pattern recognition is repeated until it reaches the outermost layer. The total number of trajectory candidates is truncated at each layer to avoid an exponential increase.
- The final trajectory candidates are cleaned for duplications, and are evaluated for their properties.

The KF track finder is applied in several successive iterations [75], each targeting a different type of track: first prompt high p_T tracks, then prompt low p_T tracks, followed by displaced tracks, and finally tracks with significant detector inefficiencies. After each iteration, all hits associated with the selected tracks are removed from the consideration of the remaining iterations. In this way, the tracking efficiency is maximized while the mis-reconstruction rate is kept as low as possible.

Tracks identified by the finder algorithm are refit with a Kalman filter and smoother to evaluate their properties: transverse momentum, direction, and origin. A Kalman filter starts with the innermost hits (typically four) on the track, and builds the covariance matrix [76], which is used to propagate hit uncertainties into the uncertainties of global track properties. This filter proceeds forward through the full list of hits, updating the trajectory estimate and the covariance matrix with each hit. The hit position uncertainty is re-evaluated using the current trajectory estimate as well at each step. As a complement, an additional filter is initialized at each hit with the result of the forward filter but works backward using all hits outside of the current hit. The weighted average of the track parameters from the two filters is taken as the estimate of the trajectory at that hit. This practice is called a smoothing procedure which ensures the optimal estimate at any hit on the track including, in particular, the innermost and outermost hit. The track is extrapolated to the interaction region and to the calorimeters and muon chambers from the closest hit (the innermost or outermost hit), which are specially important for vertex reconstruction and for track matching to signals in other detectors, respectively.

4.1.2 Primary vertices

In pp collisions at the LHC, multiple pp interactions can happen in the same bunch crossing, known as pileup. Most of them produce tracks, while only a tiny fraction of the interactions are hard scatters interesting to physicists. All the pp interactions happen in the beam interaction region (called the beam spot) which spreads along the beam axis, following a normal distribution with a standard deviation of a few centimeters. In order to separate different tracks belonging to different interactions, tracks are extrapolated to the beam axis to find their origins (vertices). The vertex reconstruction is performed with the follow procedure [75]:

- Tracks are first selected by the requirement on their compatibility with the center of the beam spot, along with some track quality criteria. This selection picks out tracks from secondary decays and tracks with low quality, ensuring a high reconstruction efficiency.
- Tracks are then clustered based on their z-coordinates at their point of closest ap-

proach to the center of the beam spot. The clustering algorithm starts with a large series of hypothetical vertices along the beam axis, and optimize the global assignment based on the likelihood of each track associated to each hypothetical vertex. After the optimization, a few ensembles of hypothetical vertices emerge, each considered as a vertex candidate.

- The position of each vertex candidate is fit with the parameters of all the tracks associated to it. The fit is performed adaptively with a weight assigned to each track reflecting the likelihood that it genuinely belongs to the vertex. The weights are updated in each iteration until the sum of weights is maximized.

All the resulting vertices along the beam axis are called the primary vertices (PVs). The PVs are ordered by the quadratic sum of the p_{T} of their tracks, $\sum p_{\mathrm{T}}^2$, and the PV with the highest $\sum p_{\mathrm{T}}^2$ is considered as the hard-scatter vertex, while the other vertices are considered as pileup vertices. In most physics analyses, the hard scatter vertex is the interaction of interest, and is therefore sometimes referred to as the single primary vertex.

4.1.3 Beam spot

The beam spot refers to the 3D-region in which pp collisions happen, and is determined from the distribution of primary vertices from many events. The position and size of the beam spot are evaluated as the x, y, z coordinates of the beam spot center and their corresponding standard deviations. These values are determined per luminosity section, which is a period of 23 seconds of event collection. If no significant shift of the beam spot center is observed in multiple consecutive luminosity sections, their beam spot position values are merged to extract a final estimate. The beam emittance grows with time, leading to a gradual growth of beam spot size. Therefore the beam spot size values are kept per luminosity section instead of merging multiple ones.

4.1.4 Muons

The muon detectors in CMS allows muons to be identified with high efficiency, which is guaranteed by the upstream calorimeters absorbing other particles (except neutrinos). The muon reconstruction combines information from both the tracker and muon chambers, building three different reconstructed muon types [10]:

- *Standalone muon.* Hits in muon chambers are clustered into track segments with a KF track finding procedure similar to the one applied in track reconstruction in Section 4.1.1. Track segments are built with DT or CSC hits as seeds and are grown into trajectories containing DT, CSC, and RPC hits. The resulting tracks are called the standalone muon tracks.

- *Tracker muon.* Each track built with tracker hits in Section 4.1.1 with a p_{T} larger than 0.5 GeV and a total momentum p larger than 2.5 GeV is extrapolated to the muon system. A comparison is made between the spatial coordinates of the extrapolated tracker track and the nearby DT or CSC muon segments. If the extrapolated track matches at least one muon segment, the tracker track is considered as a tracker muon track.

- *Global muon.* A global muon is build starting with a standalone muon and matched to a tracker track. The matching is performed by comparing KF parameters of the two tracks. A combined fit is performed using information from both the tracker track and the standalone muon track to determine the final parameters of the global muon track.

Most tracker muons are also global muons, as most muons can be successfully reconstructed as standalone muons. The track muons are more efficient in identifying low p_{T} muons, which may only leave hits in the innermost muon station but are not energetic enough to reach the others, failing to be reconstructed as a global muon. This higher efficiency, on the other hand, is accompanied with a higher misidentification rate, as hadron shower remnants can sometimes reach the innermost muon station, known as the punch-through, which could fake a tracker muon but not a global one.

The momentum of each global muon is measured fitting all tracker hits plus either zero or one, or multiple hits in muon detectors, depending on their compatibility with the extrapolated tracker track. Since the tracker hits have better spatial resolution than the muon detector hits, the contribution from muon detectors is marginal for muons with p_{T} < 200 GeV. On the other hand, for muons with $p_{\mathrm{T}} > 200$ GeV, the information from muon detectors improves the measurement significantly, because the tracks of these high p_{T} muons are very straight, and muon detector hits, being far from the tracker hits, provides essential information for the track curvature evaluation.

The isolation is another important property of muon tracks. It help to distinguish between muons from energetic prompt interactions (prompt muons) and the ones from weak decays within jets (non-prompt muons). It is defined as the ratio to the muon p_{T} by the sum of energy in a geometric cone, $\Delta R = \sqrt{(\Delta\phi)^2 + (\Delta\eta)^2}$. The summation considers all charged hadrons and neutral particles in PF [73],

$$I_{\mathrm{PF}} = \sum_{h^{\pm},HS} p_{\mathrm{T}}^{h^{\pm}} + \max(0, \sum_{h^0} p_{\mathrm{T}}^{h^0} + \sum_{\gamma} p_{\mathrm{T}}^{\gamma} - \Delta\beta \sum_{h^{\pm},PU} p_{\mathrm{T}}^{h^{\pm}}) \tag{4-1}$$

where HS means hard scatter and PU means pileup. h^0 and $h^{\pm}$ in the equation are neutral and charged hadrons. This calculation aims to mitigate the contamination from pileup and only focus on the hard scatter. The factor $\Delta\beta$ is set to be 0.5, which corresponds approximately to the ratio of neutral particle to charged hadron production in inelastic pp collisions, as an estimate to remove the pileup particle energy.

In addition to the kinematic variables, a set of variables is defined to reflect the quality of the muon reconstruction, such as the χ^2 of the track fit, the number of hits per track (either in the tracker or the muon detectors, or both), and for global muons specifically, the degree of matching between the tracker track and the standalone muon track. There are other variables evaluating whether the muon track is compatible with the primary vertex, and whether a kink can be found in the muon track. Based on these variables, CMS offers several sets of official muon identification criteria for physics analyses, each targeting a different type of muon. The specific muon selection criteria adopted in the $\mathrm{H} \to \mu\mu$ analysis is detailed in Section 4.2.1.

4.1.5 Electrons

Electrons (and positrons) produce hits in the tracker layers and are eventually absorbed by the ECAL. Both the tracker and ECAL provide information on electron identification but both suffer from significant inefficiencies: most electrons emit bremsstrahlung photons as they travel through the tracker layers and lose a sizeable fraction of their energy, which degrades the quality of the reconstructed tracks and biases the momentum measurements; while most of the electron energy including the bremsstrahlung photons is captured by a series of neighboring ECAL units, this energy deposit is very often overlapped with deposits from other photons and hadrons and is very hard to disentangle. The electron identification relies on the combination of tracker and ECAL information, starting with two types of seed [77]:

- *ECAL-based seed.* Energy deposits in several ECAL channels are grouped into clusters. If the energy deposit in a cluster exceeds 1 GeV, it is considered as a potential incident particle and the cluster is called a seed cluster. Since a final state electron may reach the ECAL as several electrons and/or photons due to bremsstrahlung radiation and photon conversion, which scatter in multiple clusters tangent to the electron track, clusters near the seed cluster are further grouped into a supercluster (SC). A SC is defined with a small window in η and an extended window in ϕ in order to follow the azimuthal bending of electron tracks in the magnetic field. If a SC can be loosely matched to a track seed (as described in Section 4.1.1), and if there is no significant energy deposit in the HCAL towers behind the SC, this SC along with the track seed(s) linked to it are selected as an ECAL-based electron seed.
- *Track-based seed.* An electron seed can also be built from a generic track if its p_{T} exceeds 2 GeV. When the energy radiated by the electron is small, the reconstructed track has good quality and can be extrapolated to the ECAL surface. If the ratio of the closest ECAL cluster energy to the track momentum is compatible with unity, The track along with the ECAL cluster is selected as a track-based seed. For electrons that lose considerable energy via photon emission, their tracks may have kinks and generally have unideal qualities. These tracks are selected with some loose quality criteria and refit with a Gaussian-sum filter (GSF), which is more CPU intensive than the KF used for general tracking, but more adapted to sudden and substantial energy losses along the trajectory. The GSF refit track is extrapolated to the ECAL surface, and a multivariate discriminator is evaluated combining the track and ECAL information. The track and the ECAL cluster is considered as an electron seed if the discriminator suggests so.

Electron seeds obtained from these two approaches are merged and submitted to a more exhaustive GSF refit. In addition, a survey is performed among generic tracks near the seeds, to pick up any track pair with a common displaced vertex. Such track pairs are likely to originate from photon conversions (more details in Section 4.1.6). Conversion tracks made lead to a refinement of the SC shape and an update (or removal) of the GSF tracks. A electron is reconstructed only if the GSF track can be built, and if the HCAL energy deposit behind the ECAL SC does not exceed 10% of the SC energy. Energy collected by the ECAL SC is subject to losses for several reasons: material in the tracker, electromagnetic shower leakages, and intermodule gaps in ECAL. The total energy in the ECAL SC is corrected with a multivariate regression algorithm to account for these energy losses. The final energy assignment for electrons is based on a combination of the corrected SC energy and the momentum of the GSF track.

The electron identification is based on several aspects of the reconstruction. The isolation of electrons follows the definition in Equation 4-1 and is the main handle to distinguish prompt electrons from non-prompt ones. The electromagnetic show shape also helps to reject fake electrons from hadrons and is described by a few variables: the ratio between the SC energy and the HCAL energy behind it, the variable $\sigma_{i\eta i\eta}$ indicating the second moment of the ECAL energy in a 5×5 crystal array, and the variable R_9 defined as the most energetic 3×3 crystal array divided by the total SC energy. A few other variables evaluates the compatibility between the ECAL SC and the track: the distance in η between the seed cluster and the track, the distance in ϕ between the energy-weighted SC position and the track, the difference between the inverse of the SC energy and the inverse of the track momentum. Furthermore, some other variables are also included accounting for how many missing hits are in the track and whether the electron is likely to come from the conversion of a photon.

CMS offers several sets of official electron identification criteria based on these variables, either in a cut-based fashion or as a multivariate discriminator. The specific electron selection criteria adopted in the $\mathrm{H} \to \mu\mu$ analysis is detailed in Section 4.1.5.

4.1.6 Photons

Photons can be produced by various processes in CMS: from prompt interactions, from bremsstrahlung emission of electrons, and from secondary decay of hadrons (mostly π^0). Although photons themselves do not produce hits in trackers, they have a significant probability to convert into an electron-positron pair in the tracker material. Photons, if not converted, are all fully absorbed by the ECAL, whose signals can very often be mixed with the signals from nearby electrons and hadrons if there are any. As a result, photon identification is entangled with the reconstruction of electrons and hadrons. In CMS, photons can be defined in three cases at different stages of the PF reconstruction: the converted photons based on displaced track pairs and their associated ECAL clusters, the isolated unconverted photons based on ECAL deposits with little HCAL energy deposit behind it, and the non-isolated unconverted photons based on ECAL deposits with significant HCAL energy deposit behind it.

The reconstruction of converted photons involves tracks and ECAL clusters, and is performed along with the reconstruction of electrons and isolated unconverted photons. After the electron seeding stage, a conversion finding algorithm [78] examines all tracks near the ECAL SC and looks for tracks significantly displaced from the primary vertex. If displaced tracks of different charges are found, they are paired with some proximity requirement and fit to a common vertex with a kinematic vertex fit. These track-pair candidates are defined as converted photons if they satisfy thresholds on the quality of kinematic fit, on the total p_{T}, and on the compatibility between the converted tracks and the associated ECAL clusters.

The reconstruction of isolated photons shares the same procedure as the electron reconstruction described in Section 4.1.5, and is only different at the last stage: an electron is defined if a GSF track can be built from the seed, while a photon is defined if no GSF track can be built associated to the ECAL SC and if the E_{T} is greater than 10 GeV. These photon candidates from ECAL seeding are further retained if they are isolated from other tracks and ECAL clusters and if there are no significant HCAL energy deposits around. The corrected ECAL SC energy is used for the final photon energy assignment.

More often, photons in CMS are produced by decays of hadrons and are not isolated from other calorimeter deposits. The reconstruction of non-isolated photons is performed along with the reconstruction of hadrons, which is detailed in Section 4.1.7. Once muons, electrons, isolated photons, and charged hadrons are reconstructed by PF, the tracks and calorimeter deposits associated to them are masked, leaving only unassigned ECAL and

HCAL clusters. In general, photons carry about 25% of the total jet energy, all absorbed by the ECAL, while neutral hadrons leave only 3% of the total jet energy in the ECAL. Therefore, within the tracker acceptance ($|\eta| < 2.5$), as charged hadrons are already identified, all the unassigned ECAL deposits are considered as photons and all remaining HCAL deposits are considered as neutral hadrons. However, out of the tracker acceptance, charged hadrons cannot be distinguished from neutral ones. Charged and neutral hadrons together leaves about 25% of the total jet energy in the ECAL, which is at the same level of photon energy. ECAl deposits can no longer be assumed as photons. In this case, hadrons are reconstructed with HCAL clusters, and a fraction of energy is removed from the associated ECAL clusters. The remaining net ECAL clusters are reconstructed as photons. The energy estimate of these non-isolated photons takes the uncorrected ECAL cluster energy.

The identification of photons is based on the isolation and electromagnetic shower shape variables as described for electron identification (Section 4.1.5). CMS offers identification criteria either as cut-based selections or a multivariate discriminator. These identifications target only isolated photons, while the non-isolated one are encapsulated in jets (Section 4.1.7). Photons are not used in the $\mathrm{H} \to \mu\mu$ analysis as primary physics objects, but are only used for the recovery of the energy losses in final state radiation (FSR). The selection for FSR photons is described in Section 5.2.

4.1.7 Hadrons

Hadrons are produced in plenty by pp collisions in CMS. Charged hadrons leave hits in the tracker and all hadrons are fully absorbed by the calorimeters. All hadrons are initiated by gluons or quarks in QCD process, and are always produced as cascades, known as jets. As a result, their detector signals, especially in calorimeters, always overlap with one another. As the detectors only provide information on the trajectory (for charged hadrons only) and energy of the hadrons, CMS reconstruct hadrons as charged and neutral ones without further distinguishment of their exact composition.

Energy deposits in HCAL are grouped into clusters in a similar fashion as that in the

ECAL seeding. Cluster seeds are first identified as HCAL cells that have an energy over a threshold and larger than their neighboring cells. Seeds are grown into topological clusters by iteratively including adjacent cells with an energy above another threshold. A topological cluster may cover many seeds if they are connected by cells with significant energy deposits. Each topological cluster is fit with a Gaussian-mixture model in which the energy distribution in the cells is assumed to be the sum of N Gaussian energy distributions, where N is the number of seeds in the topological cluster. Each resulting Gaussian component is considered a a cluster.

Within the tracker acceptance, HCAL clusters linked to tracks are reconstructed as charged hadrons. Non-isolated photons and neutral hadrons are reconstructed from the remaining ECAL and HCAL clusters respectively. Beyond the tracker acceptance, hadrons are reconstructed from the HCAL clusters without differentiating their charges, and photons are reconstructed with the remaining ECAL clusters.

All hadrons (and non-isolated photons) are considered as PF candidates but are not used as individual physics objects for analyses. PF candidates are clustered into more complex objects like jets and the hadronic decays of τ leptons, which are used in physics analyses indicating outgoing partons or τ leptons from the collisions. Jets are reconstructed with the anti-k_T algorithm [79, 80], and hadronic τ decays are reconstructed wth the hadrons-plus-strips (HPS) algorithm [81, 82] seeded from jets. Jets can be reconstructed considering all PF candidates (PF jets), or reconstructed with PF candidate except charged hadrons from pileup vertices via charged hadron subtraction (CHS). Only CHS jets are used in the $\mathrm{H} \to \mu\mu$ analysis.Hadronic τ decays are not used in the $\mathrm{H} \to \mu\mu$ analysis.

4.1.8 Missing transverse momentum

Neutral particles produced in pp collisions that interact weakly with regular material can traverse the CMS detector undetected. There is no way to determine their number, type, or exact direction. However, when these particles are produced along with detectable particles: muons, electrons, photons, hadrons etc., their presence can be inferred from the detected particles as an imbalance in the total momentum perpendicular to the beam pipe. This imbalance is referred to as the missing transverse momentum ($\vec{p}_T^{miss}$) or the missing transverse energy ($E_{\mathrm{T}}^{\mathrm{miss}}$). No distinguishment is made between $E_{\mathrm{T}}^{\mathrm{miss}}$ and the magnitude of the missing transverse momentum (p_T^{miss}) as there is no way to infer the invariant mass of the missing particle(s).

$E_{\mathrm{T}}^{\mathrm{miss}}$ (or $H_{\mathrm{T}}^{\mathrm{miss}}$) itself is not a physics object but is crucial to physics analyses, both in SM measurements containing leptonic decays of the W boson and in searches for new weakly-interactive particles beyond the SM. CMS offers two ways to reconstruct the $E_{\mathrm{T}}^{\mathrm{miss}}$ [83]. The PF $E_{\mathrm{T}}^{\mathrm{miss}}$ [84] is defined as the negative of the vector p_{T} sum of all PF candidates in the event. The other reconstruction method is called the "pileup per particle identification" (PUPPI) [85], which sums all PF candidates while rescaling the energy of all hadrons based on their likelihood of originating from the PV. The PF $E_{\mathrm{T}}^{\mathrm{miss}}$ is used in the $\mathrm{H} \to \mu\mu$ analysis.

In addition, another missing energy estimate based on high level physics objects, $H_{\mathrm{T}}^{\mathrm{miss}}$, are adopted in many analysis. It sums only identified leptons and jets, instead of all PF candidates, in order to focus on the expected products of the prompt interaction. In the $\mathrm{H} \to \mu\mu$ analysis, the $H_{\mathrm{T}}^{\mathrm{miss}}$ definition only considered leptons and jets that pass their selection criteria specific in 4.2.

By its nature, the resolution of $E_{\mathrm{T}}^{\mathrm{miss}}$ (or $H_{\mathrm{T}}^{\mathrm{miss}}$) is much worse than other physics objects. A mismeasurement on $E_{\mathrm{T}}^{\mathrm{miss}}$ can originate from proton debris falling out of the detector acceptance, mis-reconstruction of objects and mis-association between pileup and primary vertices, and in general experimental resolution in all detector components. Improving the $E_{\mathrm{T}}^{\mathrm{miss}}$ estimate is the key to improve the precision of many measurements and the sensitivity of many searches.

4.2 Object selection in the H to muons analysis

4.2.1 Muon selection

CMS provides official muon identification (ID) criteria based on several kinematic variables: the number of hits in the muon track; the fit quality of the muon track; the compatibility between the tracker track and the standalone muon for global muons; and the compatibility between the muon track and the primary vertex. The global track fit χ^2 and a kink-finder χ^2 are used as indicators of the fit quality of the global muon track. The compatibility between the tracker track and the standalone muon is evaluated with the χ^2 of the position match, and a variable called the segment compatibility. The compatibility between the track and the primary vertex is evaluated with their impact parameters (as defined in Section 5.3.1) along with a variable (called the SIP) reflecting the significance of the impact parameters relative to its uncertainty.

The official muon identification is provided for different types of muons [10]: ID for generic muons, dedicated ID for low-p_T muons ($p_T < 20$ GeV), and dedicated ID for high-p_T muons ($p_T > 200$GeV). The muons of moderate-p_T are used in most studies on electroweak and Higgs physics, and can be selected with three levels (known as working points) of generic identifications:

- *Loose muon ID* selects PF muons that is either a tracker or a global muon without further requirements. It has the highest selection efficiency among all IDs.
- *Medium muon ID* poses requirements on the number of hits in the tracker track and on the track fit quality, on top of the loose ID. The number of tracker hits must be more than 80% of the number of tracker layers the muon traverses. The global fit χ^2 must be less than 3, the kink-finder χ^2 must be less than 20, and the position match χ^2 must be less than 12. The segment compatibility is required to be greater than 0.303 for global muons, or greater than 0.451 for tracker-only muon. It rejects badly-reconstructed muons while keeping a high efficiency for the well-reconstructed ones.
- *Tight muon ID* suppresses muons from decay in flight and from hadronic punch-through. The muon must be a loose muon, as well as a global muon with its track fit $\chi^2 < 10$. The muon track must include at least one hit in the muon chamber and at least six layers of the inner tracker, at least one of them been pixel hits. It must also be compatible with the primary vertex, with $d_{xy}^{PV} < 0.2\,\text{cm}$, $d_z^{PV} < 0.5\,\text{cm}$.

Several levels of selection criteria on the PF isolation is also centrally provided, in which the Loose Isolation requires the PF isolation of the muon in a cone of $\Delta R < 0.4$ to be less than 25% of the muon p_{T}. It cleans muons from hadronic activities and keeps a selection efficiency of about 99% regarding to the Medium ID.

The $\mathrm{H} \to \mu\mu$ analysis adopts the Medium muon ID and Loose Isolation as a baseline selection. In addition, muons are required to have $p_{\mathrm{T}} > 20\mathrm{GeV}$ and $|\eta| < 2.4$, and should be compatible with the primary vertex with impact parameters $d_{xy}^{PV} < 0.05\,\mathrm{cm}$, $d_{z}^{PV} < 0.1\,\mathrm{cm}$ and the SIP < 8.0.

Finally, to further reject non-prompt muons, a multivariate identification method, called the LeptonMVA, is applied. Several analyses in CMS have used the LeptonMVA approach, and the version adopted by the $\mathrm{H} \to \mu\mu$ analysis is developed in the context of the search for tZq production [86]. This LeptonMVA comines the information of the muon isolation, the vertex compatibility, and the relative position and relative energy between the muon and its closest jet. The selection requirement on the LeptonMVA is chosen to be LeptonMVA > 0.4, which corresponds to an efficiency of about 95% and a fake rate of about 3-4%.

4.2.2 Electron selection

As described in Section 4.1.5, the electron identification in CMS is based on the electron track quality and the properties of the ECAL supercluster: $\sigma_{i\eta i\eta}$, $|\Delta\eta_{in}^{seed}|$, $|\Delta\phi_{in}|$, H/E, $|1/E - 1/p|$, the number of missing hits, and the photon-conversion indicator. The official identification criteria is provided either as a series of selection cuts based on these variables, or as a multivariate discriminator summarizing these variables [77].

The cut-based ID includes four standard working points: Veto ID used for vetoing electrons, corresponding to about 95% efficiency; Loose ID which is tolerant for fake electrons, with an efficiency of about 90% on real electrons; Medium ID which balanced between the fake rate and the signal efficiency, which is about 80%; and the Tight ID which is about 70% efficient for real electrons but also has a low fake rate. The multivariate discriminator is developed combining the aforementioned variables, plus the PF isolation of the electron, the fraction of the track momentum at the outermost tracker layer relative to that at the innermost tracker layer, and a variable evaluating the track-cluster match. Two working points are provided for the MVA-based ID, corresponds to 80% and 90% efficiencies.

The $\mathrm{H} \to \mu\mu$ analysis adopts the 90%-efficiency working point of the MVA-based ID as a baseline selection. It also requires electrons to have $p_{\mathrm{T}} > 20\mathrm{GeV}$ and $|\eta| < 2.5$, and to be compatible with the primary vertex with impact parameters $d_{xy}^{PV} < 0.05\,\mathrm{cm}$, $d_{z}^{PV} < 0.1\,\mathrm{cm}$ and the SIP < 8.0. The electron must also have less than two missing hits in its track, and must not be linked to a photon conversion, these two requirements being used in the cut-based ID but not included in the MVA-ID. The ECAL is less efficient in the region of $1.444 < \eta < 1.566$, where there are gaps between ECAL modules. Electrons in this is not considered for the analysis.

Finally, the LeptonMVA discriminator, similar to that for muons, is also developed for electrons in Ref. [86]. The selection requirement of LeptonMVA > 0.4 is also applied to electrons, corresponding to an efficiency of about 93% and a fake rate of about 4%.

CHAPTER 5
MUON MOMENTUM CORRECTION AND CALIBRATION

This analysis aims to find a sharp signal peak on top of a smooth background in the $m_{\mu\mu}$ distribution. It is of crucial importance to correct the mismeasurement in muon momentum scale and improve the momentum resolution. The sharper muon peak, the better sensitivity of this analysis. It is also crucial to reduce the differences in the muon momentum scale and resolution between data and simulation, so that there is no significant bias in the modeling of the signal.

Three sets of corrections are applied in this analysis: the *Rochester correction* [87], the recovery of the final state radiation (FSR) photons, and the *GeoFit correction*. The *Rochester correction* is a centrally provided correction (by CMS) which corrects the biases in the muon momentum resulted from the mismodeling of detector alignment and magnetic field. A brief description of the *Rochester correction* is given in Section 5.1, while the technical details can be found in the Ref. [87]. The *FSR recovery* is a common practice in many CMS analyses which corrects the muon energy loss via FSR radiation. The recovery scheme in this analysis is optimized specifically for the $\mathrm{H} \to \mu\mu$ decay, which is described in Section 5.2 and in more details in Ref. [14]. The *GeoFit correction* is developed by the author in the context of the $\mathrm{H} \to \mu\mu$ analysis and approved by the CMS collaboration. It uses information of muon vertexing to correct the biases in muon momentum of the reconstructed muon tracks. The development of the *GeoFit correction* is described in details in Section 5.3. The effects these three corrections focus on are orthogonal, and are even mutually exclusive between the *FSR recovery* and *GeoFit correction*. In practice, the *Rochester correction* is applied to all muons, then each muon is surveyed for FSR photons. If a FSR photon is found associated to the muon, the *FSR recovery* is applied, if not, the *GeoFit correction* is applied.

The *Rochester correction*, *FSR recovery*, and *GeoFit correction* are applied to both data and simulation. The performance of the muon corrections is examined with the study on the $\mathrm{Z} \to \mu\mu$ peak, which is listed in details in Section 5.4. These corrections fix all the known biases in muon measurement, and ensure a per-mille-level agreement between data and simulation.

5.1 Rochester correction

In reality, the CMS detector can have various imperfections, such as the misalignment of the detector components, and the uncertainties in the magnetic field. Sometimes these imperfections are not correctly emulated in reconstruction software, and as a result, the reconstructed muons can be inaccurate. These measurement biases are reflected as the dependences of the muon momentum on its η, ϕ coordinates, and its charge. These dependences, in turn, smear the inclusive muon resolution and lead to sub-optimal physics results.

On the other hand, in the simulation of CMS events, none of the imperfections is assumed, which leads to slightly different detector responses from those in data, and eventually mismodelings (usually over-optimistic modelings) in muon measurement. The muon correction also needs to be applied to the simulation, in a manner not exactly the same as that to data. This also means that the reconstructed muons in simulation cannot be used as the reference for the correction. Instead, the correction is derived from the generated muon information, smeared with some functional forms to match the experimental resolution. This provides a set of reference muons that is free from any bias in reconstruction.

The well-understood $\mathrm{Z} \to \mu\mu$ events are used to develop the *Rochester correction*. The idea of the correction is briefly summarized as follows:

- For data, reconstructed simulation (reco-sim), and the reference simulation (ref-sim), muons are divided into different η and ϕ bins, separately for μ^+ and μ^-. In each bin, the $1/p_\mathrm{T}$ distributions of data and reco-sim are corrected so that the mean value of the distribution becomes the same as that in the ref-sim.
- The $1/p_\mathrm{T}$ in reco-sim is usually narrower than that in data. A smearing is applied to the reco-sim $1/p_\mathrm{T}$ distribution so that it matches the resolution in data.
- After the steps above, the $m_{\mu\mu}$ in each bin may still be off from the expected distribution by some small amounts. The ratio between this offset and the nominal Z mass is applied to the muon p_T as a correction factor iteratively, until the offset is minimized.

The *Rochester correction* removes the $m_{\mu\mu}$ dependences on muon η, ϕ, and charge, as well as the $m_{\mu\mu}$ resolution differences between data and the simulation. Details of the performance of the *Rochester correction* can be found in Section 5.4.

5.2 FSR recovery

In CMS, muons produced in pp collisions may radiate photons and lose energy, which is referred to as the final state radiation (FSR). The radiation may carry substantial energy and lead to a underestimation of the muon momentum, In an analysis that relies on the dimuon mass $m_{\mu\mu}$, the FSR may lead to two effects that degrade the sensitivity: a loss of event acceptance, and a smearing of the $m_{\mu\mu}$ resolution. To mitigate these effects, some of the FSR photons can be identified can added back to the muon energy, which is called the *FSR recovery*.

The selection for the FSR photons is modified on top of the strategy developed in the CMS $\mathrm{H} \to \mathrm{ZZ}$ analyses [22, 88]. The selection criteria is summarized as follows:

- Photons with transverse energy $E_T^\gamma > 2$ GeV and $|\eta| < 1.4$, $1.6 < |\eta| < 2.4$ are considered as FSR candidates.
- The photon is required to be within the cone of $\Delta R < 0.5$ around its closest muon which satisfies $p_\mathrm{T} > 20$ GeV and $|\eta| < 2.4$.
- The photon is not identified as a bremsstrahlung photon associated with a reconstructed electron.
- The PF isolation of the photon in a cone of $\Delta R < 0.3$ should be less than 1.8, i.e. $\sum_i p_\mathrm{T}^i(\Delta R(\gamma, i) < 0.3)/p_\mathrm{T}(\gamma) < 1.8$, where i iterates the PF objects around the photon other than the candidate muon.
- The separation between the photon and the muon satisfies $\Delta R(\mu,\gamma)/p_\mathrm{T}^2(\gamma) < 0.012$.
- In order to suppress energetic photons from the $\mathrm{H} \to \mathrm{Z}\gamma \to \mu\mu\gamma$ process, the p_T ratio between the photon and the muon is required to be less than 0.4, i.e. $p_\mathrm{T}(\gamma)/p_\mathrm{T}(\mu) < 0.4$.
- If multiple FSR photons are associated to a same muon, only the photon with the smallest $\Delta R(\mu,\gamma)/p_\mathrm{T}^2(\gamma)$ is taken.

With this set of selection, about 3% of signal events are tagged with FSR photons. The momentum of the FSR photons are added to the muon momentum, while the photons themselves are removed from the calculation of the muon isolation. The *FSR recovery* significantly improves the $m_{\mu\mu}$ reconstruction in the FSR tagged events, as shown in the left plot of Figure 5-1. And overall, as shown in the right plot of Figure 5-1, the effect on the inclusive signal is a 3% improvement on the $m_{\mu\mu}$ resolution, and a 1.7% increase in the total signal yield. The performance of *FSR recovery* is also validated with the $Z \to \mu\mu$ events, shown in Figure 5-2, where a good agreement is kept between simulation and data with or without the *FSR recovery*. The *FSR recovery* is expected to perform the same way on data as on simulation, and no bias is introduced by the application of the *FSR recovery*.

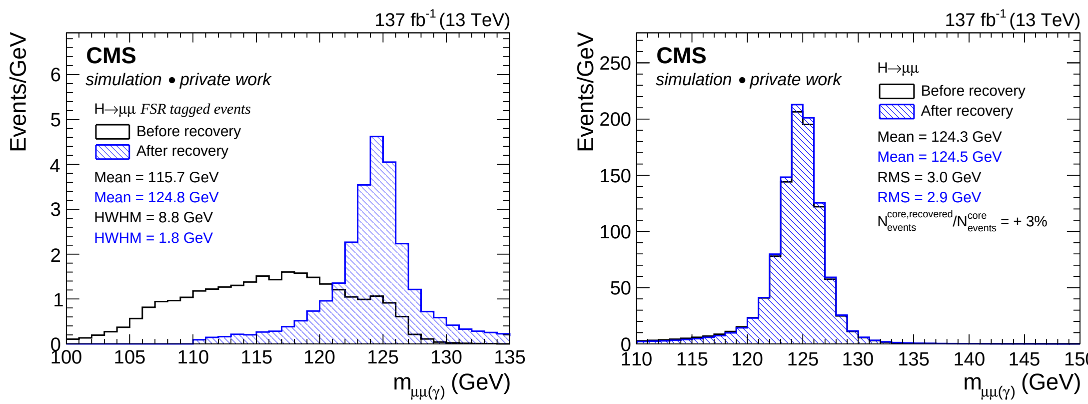

Figure 5-1. Performance of the *FSR recovery* in the simulated $H \to \mu\mu$ events. The $m_{\mu\mu}$ before and after the *FSR recovery* are shown for the events that contain at least one FSR photon (left), and for the inclusive signal events (right). Plot taken from Ref. [14].

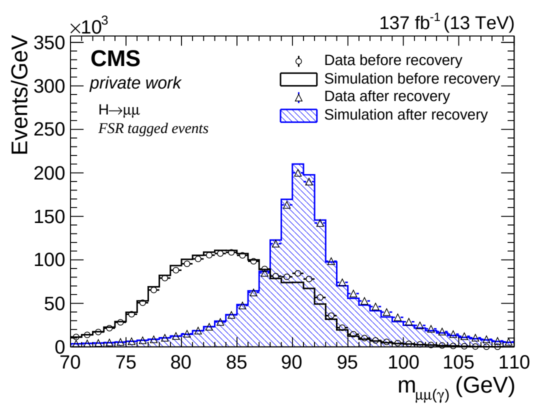

Figure 5-2. Performance of the *FSR recovery* in the $Z \to \mu\mu$ events that contain FSR photons, in both data and simulation. A good agreement between simulation and data is observed, before or after the correction. Plot taken from Ref. [14].

5.3 GeoFit correction

In CMS, charged tracks are reconstructed from the hits in the tracker system. The tracks may originate from primary vertices (PV), which are vertices of the pp interactions, or secondary vertices, which are the decay vertices of particles with a non-infinitesimal lifetime. The track reconstruction does not assume any vertex information since the vertices are reconstructed as the intersections of groups of tracks. This practice is essential for the studies of b quarks, τ leptons, and other long-lived particles that produce a vertex displaced from the colliding region in the transverse plane at the scale of a millimeter or above. However, for the tracks from prompt interactions, such as the decay of a Z boson, W boson, or H boson, called the prompt tracks, even if they are expected not to have a visible displacement from the PV, a non-zero displacement may still appear in reconstruction, due to the uncertainties in the track fit. In other words, if a track is known to be prompt, the posterior information on the colliding position can be used to improve the quality of the track fit, and in turn the measurement on the track momentum.

The study shown in this section reports the finding that this false displacement in prompt tracks has a strong geometrical correlation with the mis-measurement of the track momentum. A simple analytic function can be derived from the geometry and can be verified by fitting the displacement vs the p_{T} bias in the simulated samples. This analytic form is applied as a correction to p_{T} and is therefore named the *GeoFit correction*. Section 5.3.1 explains the geometry of the track displacement and the correlation between different variables. Section 5.3.2 describes the studies on simulated samples in order to find the best fit parameters in that correlation. The *GeoFit correction* is developed using only muon tracks in the context of the $\mathrm{H} \to \mu\mu$ search. It removes the dependence of $m_{\mu\mu}$ on track displacement which leads to an improvement on the $m_{\mu\mu}$ resolution of the combined signal ranging from 3% to 10%, depending on the data-taking period. Details of the *GeoFit correction* performance, along with validation studies are shown in Section 5.3.3. In addition, an alternative way to correct this p_{T} bias is to redo the track fit including the colliding vertex as an additional hit in the track, which should achieve a more fundamental correction at the cost of more computational resources. A preliminary set of study comparing the *GeoFit correction* with the track re-fit shows the two correction methods give almost equivalent results, detailed in Section 5.3.4.

5.3.1 Geometry of the track displacement

The displacement of a track from a vertex is usually measured as the impact parameters, d_{xy} and d_z, which are the signed distance between the vertex and its point of closest approach (PCA) on the track, in the transverse and longitudinal directions. In CMS, because most studies only care about the transverse impact parameter, the PCA is defined as the point on the 2D-projection of the track in the transverse plane that is the closest to the vertex. (It is not necessarily the PCA in the 3D-space. The d_z is calculated at the 3D-point corresponding to the 2D-PCA, rather than the 3D-PCA.) As the d_z is not used in our studies, the term "impact parameter", if not otherwise stated, refers specifically to the transverse impact parameter d_{xy}, also denoted as d0. The definition of d0 can be expressed as

$$d0 = -x_0 \cdot sin(\phi_0) + y_0 \cdot cos(\phi_0) \tag{5-1}$$

where (x_0, y_0) is the coordinate of a point near the vertex in the frame in which the vertex is at $(0,0)$, and ϕ_0 is the azimuthal angle of the track at (x_0, y_0). A scheme for this definition is shown in Figure 5-3.

In the track geometry, illustrated in Figure 5-4, the reconstructed track is very close to, but slightly deviated from, the true track, which leads to a small d0 between the reco track and the true vertex, as well as a small distance between the circular centers of the reco track and the true track. The circular centers of the two tracks are labels as O and O' for the true track and the reco track, and s is the distance between O and O'. The radii of the two tracks are r and r', with $\Delta r = r' - r$. The two tracks must intersect at two points, labeled as point M and N, with the distance between M and N denoted as l. β is half of the central angle spanned by the chord l in the true track, while α is the angle $\angle O'MO$. The

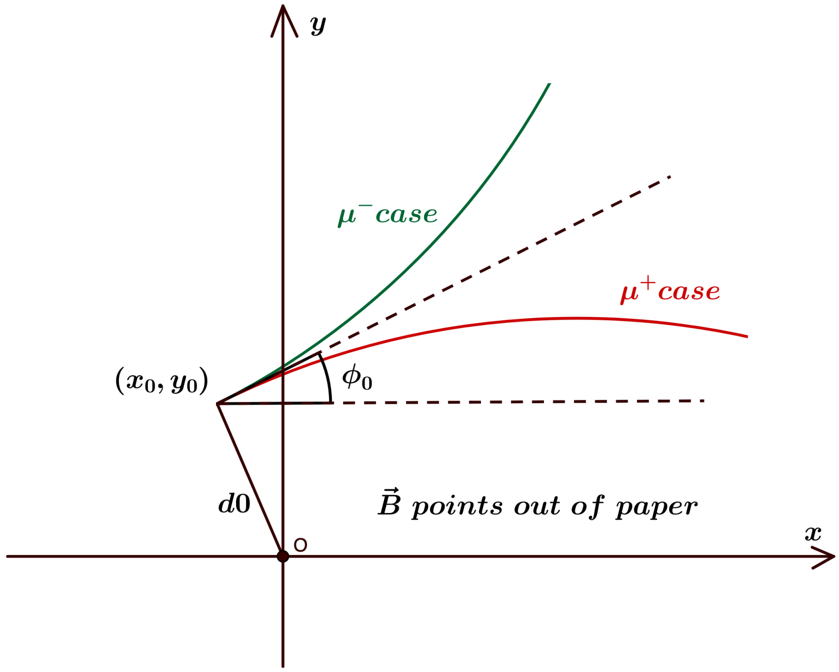

Figure 5-3. Scheme of the d0 definition in CMS. The (x_0, y_0) is the coordinate of a point near the vertex in the frame where the vertex is at $(0,0)$, and the ϕ_0 is the azimuthal angle of the track at (x_0, y_0).

true vertex is denoted as V, with d0 as the impact parameter of the reco track to it, while the PCA on the reco track is denoted as P. The distance between M and V is marked as x. As this scheme represents typical muon tracks in CMS, the radii of the tracks under study are at the scale of several tens of meters, and the Δr is expected to be much smaller than r. Points M and N are expected to be around the coverage of the CMS tracker system, which is about a meter. Therefore x and l are expected to be much smaller than r as well. Finally, the d0 scale of the tracks under study is about ten microns, which is much smaller than x, l, and r.

In this setup, a few geometrical relationships can be found between different variables, listed as follows: Since $x \ll r$, arc $\overset{\frown}{VM}$ and $\overset{\frown}{PM}$ can be viewed as line segments which are respectively perpendicular to OM and $O'M$. Therefore in triangle $\triangle VMP$,

$$d0 = x \cdot sin\alpha \tag{5-2}$$

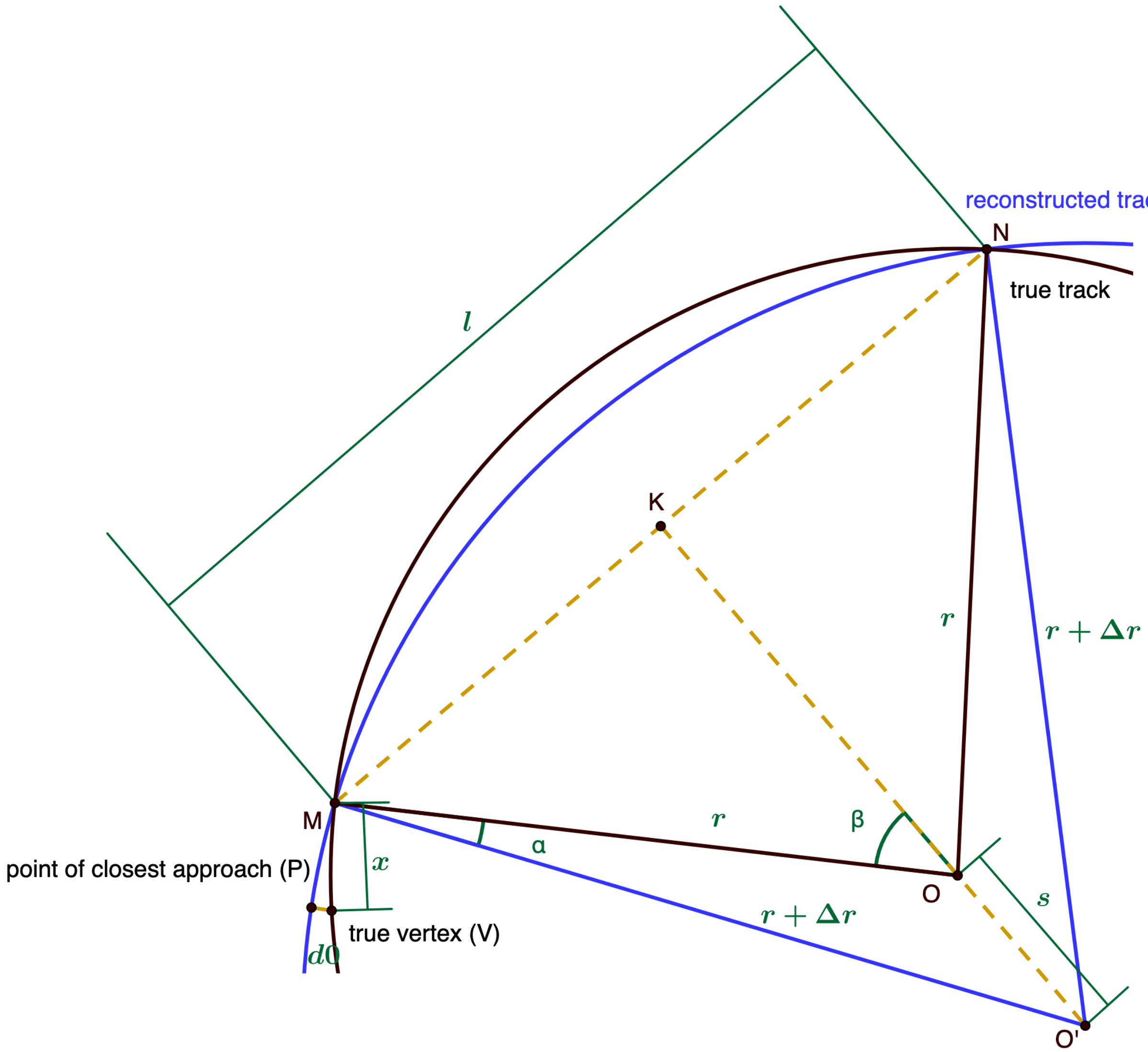

Figure 5-4. Scheme of the track geometry in the transverse plane. The blue lines show the geometry of the reconstructed track, compared to the black lines which are the geometry of the true track. The difference between the blue track and black track is exaggerated in this scheme. The blue track and the black track must intersect at two points. l is the distance between the two intersections, and x is the distance between the true vertex and the first intersection. s is the distance between the circular centers of the two tracks.

In triangle $\triangle O'MO$, the sine law gives

$$\frac{s}{sin\alpha} = \frac{r + \Delta r}{sin\beta} \tag{5-3}$$

And in triangle $\triangle O'MK$,

$$sin\beta = \frac{l/2}{r} \tag{5-4}$$

Then, using the Pythagorean theorem in both triangle $\triangle O'MK$ and triangle $\triangle OMK$, there is

$$s = \sqrt{(r+\Delta r)^2 - (l/2)^2} - \sqrt{r^2 - (l/2)^2} \tag{5-5}$$

Combining Equation 5-2 to 5-5 and assuming $r \gg l$, one can get

$$d0 = \frac{xl}{2} \cdot \frac{\Delta r}{r^2} \tag{5-6}$$

Note that in CMS, under the 3.8T magnetic field, tracks follow

$$p_{\mathrm{T}} \text{ (in GeV)} = 1.14 \cdot r \text{ (in meter)} \tag{5-7}$$

We reach

$$d0 \propto \frac{\Delta p_{\mathrm{T}}}{p_{\mathrm{T}}^2} \tag{5-8}$$

Now a quantitative relationship is extracted between d0 and p_{T}, but with one caveat: the variables x and l in the scheme above may vary track by track, and are impossible to measure in real data, meaning that the coefficient in the proportionality is not a constant for different tracks, and Equation 5-8 can be smeared. Therefore, to validate this proportionality, studies are performed on simulated samples comparing the reconstructed p_{T} and the generated p_{T} of muon tracks. Plots of $(p_{\mathrm{T}}^{reco} - p_{\mathrm{T}}^{gen})/(p_{\mathrm{T}}^{gen})^2$ vs d0 are made, to see whether the proportionality can be observed after the smearing, which is the topic of Section 5.3.2.

Another remark needs to be made, that in Figure 5-4 the p_{T} mismeasurement is related to the relative position of the true vertex to the reconstructed track. To be more specific, if the true vertex is inside of the reco track, the p_{T} is overestimated, while if the true vertex is outside of the reco track, the p_{T} is underestimated. However, in the CMS definition of d0 shown in Figure 5-3, the sign of d0 corresponds to an opposite relative position between the vertex and the track for the positively charged muons and the negatively charged muons. A positive d0 value means the true vertex is inside of the reco track if the muon is positive, but outside of the reco track if the muon is negative. Therefore in CMS convention the d0-p_{T} correlation is expected be reversed for different muon charges, and in Section 5.3.2 studies are always performed evaluating d0 $\cdot$ charge rather than just d0.

5.3.2 Development of GeoFit

The $(p_{\mathrm{T}}^{reco} - p_{\mathrm{T}}^{gen})/(p_{\mathrm{T}}^{gen})^2$ vs d0 plots are made with the following steps: The values p_{T}^{reco}, p_{T}^{gen}, and d0 are extracted for each track in simulated samples. The distribution of $(p_{\mathrm{T}}^{reco} - p_{\mathrm{T}}^{gen})/(p_{\mathrm{T}}^{gen})^2$ is made for tracks in different d0 $\cdot$ charge bins. The maximum position and the corresponding full-width-half-maximum (FWHM) is found for each fine-binned $(p_{\mathrm{T}}^{reco} - p_{\mathrm{T}}^{gen})/(p_{\mathrm{T}}^{gen})^2$ distribution and set as the value and the uncertainty of one data point in the plots in Figure 5-5. The plots are then fit with analytic functions which are considered as the experimental realization of Equation 5-8.

In CMS, the colliding position can be measured as two different physics objects, the primary vertex (PV) and the beam spot (BS). A primary vertex is a 3D-point which is compatible with several tracks in the same event. Usually several PVs are reconstructed per event, each of them considered as the position of a pp collision instance. The beam spot, on the other hand, is actually a 3D-region in which most of the pp collisions happen, and is reconstructed with all tracks in all the events in each luminosity section. The beam spot is usually around 10-20 μm wide in the x, y directions, and about 7-9 cm long in the z direction.

Both the PV and the BS are reasonable representation of the colliding position and are useful in different cases. The PV has a good z coordinate precision and can be used to judge if two tracks originate from the same interaction. But the position of the PV can be biased by the few energetic tracks associated to it, as the tracks are weighted by their p_{T}^2 in the reconstruction of the PV. The BS is wide-spread in z direction, but is less affected by individual tracks in its x, y coordinates. To compare the two types of vertices, the d0 is measured regarding each of them, and examples of the $(p_{\mathrm{T}}^{reco} - p_{\mathrm{T}}^{gen})/(p_{\mathrm{T}}^{gen})^2$ vs d0 dependences are shown in Figure 5-5. The dependence in the PV plot is not linear as the reconstructed PV is pulled towards the energetic muon tracks, while the dependence in the BS plot follows a linear trend as predicted in Equation 5-1. Therefore, the BS is considered as the position of the true vertex in the rest of the study.

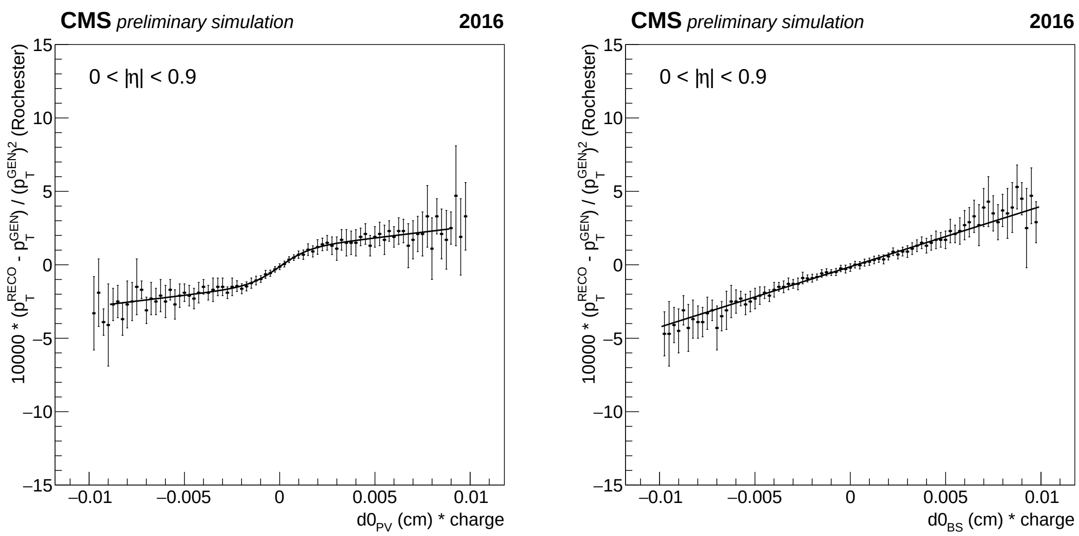

Figure 5-5. Example plots showing the correlation between $(p_{\mathrm{T}}^{reco} - p_{\mathrm{T}}^{gen})/(p_{\mathrm{T}}^{gen})^2$ and d0 $\cdot$ charge. The vertices used for the d0 calculation are the PV (left) and the BS (right). The PV plot shows a modulated dependence from expectation while the BS plot shows a linear shape as expected. Only barrel tracks from 2016 data are shown as examples. Plots of other $|\eta|$ regions and other data-taking periods show similar behaviors. Plots credit to Efe Yigitbasi.

The $(p_{\mathrm{T}}^{reco} - p_{\mathrm{T}}^{gen})/(p_{\mathrm{T}}^{gen})^2$ vs d0 correlation is found to be different in different $|\eta|$ regions and data-taking periods: different $|\eta|$ regions are covered by different detector components, and there have been upgrades on the detector and the reconstruction algorithm between different data-taking periods. Overall, the $(p_{\mathrm{T}}^{reco} - p_{\mathrm{T}}^{gen})/(p_{\mathrm{T}}^{gen})^2$ vs d0 correlation is evaluated by three years (2016, 2017, 2018) and three $|\eta|$ regions (barrel, overlap, endcap), shown in Figure 5-6 for 2016, 5-7 for 2017, and 5-8 for 2018. Each of the plot is fit with a linear function, whose best fit parameters are also shown in the plot.

These fit results are applied as the analytic correction to muon p_{T}, based on the d0,

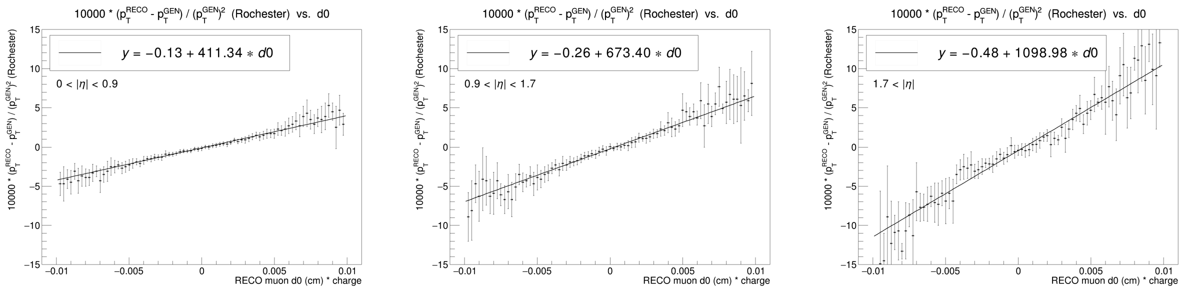

Figure 5-6. Plots for the $(p_{\mathrm{T}}^{reco} - p_{\mathrm{T}}^{gen})/(p_{\mathrm{T}}^{gen})^2$ vs d0 correlation in the 2016 DY simulation, and the linear fits to them. Muon tracks are divided into three different $|\eta|$ regions: $|\eta| < 0.9$ (left), $0.9 < |\eta| < 1.7$ (middle), and $1.7 < |\eta|$ (right). Plots credit to Efe Yigitbasi.

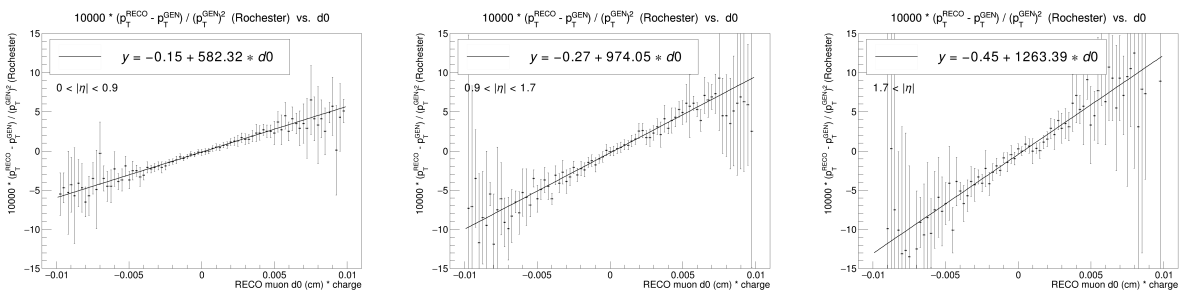

Figure 5-7. Plots for the $(p_{\mathrm{T}}^{reco} - p_{\mathrm{T}}^{gen})/(p_{\mathrm{T}}^{gen})^2$ vs d0 correlation in the 2017 DY simulation, and the linear fits to them. Muon tracks are divided into three different $|\eta|$ regions: $|\eta| < 0.9$ (left), $0.9 < |\eta| < 1.7$ (middle), and $1.7 < |\eta|$ (right). Plots credit to Efe Yigitbasi.

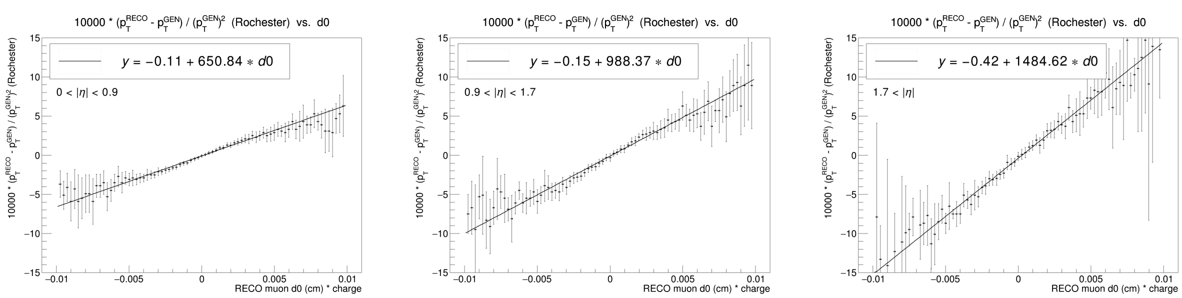

Figure 5-8. Plots for the $(p_{\mathrm{T}}^{reco} - p_{\mathrm{T}}^{gen})/(p_{\mathrm{T}}^{gen})^2$ vs d0 correlation in the 2018 DY simulation, and the linear fits to them. Muon tracks are divided into three different $|\eta|$ regions: $|\eta| < 0.9$ (left), $0.9 < |\eta| < 1.7$ (middle), and $1.7 < |\eta|$ (right). Plots credit to Efe Yigitbasi.

p_{T}, $|\eta|$, and charge of the muon. The correction is applied to all muons in data and simulation in all categories in the $\mathrm{H} \to \mu\mu$ analysis, unless the muon is tagged for *FSR recovery*. The performance of this correction is detailed in Section 5.3.3.

5.3.3 Performance and validation

The *GeoFit correction* removes the p_T dependence on d0, the overall effect of which on the $Z \rightarrow \mu\mu$ peak is illustrated in Figure 5-9. A clear trend in the $m_{\mu\mu}$ is seen regarding to d0 before the *GeoFit correction*, while no significant dependence remains after the correction. As a side remark, the $m_{\mu\mu}$ mismeasurement in Figure 5-9 can be as large as 1.5 GeV for extreme d0 values, but in data and simulation the distribution of the muon d0 is roughly a Gaussian shape with a standard deviation around 15 μm. So most of the events are near the center of the plots, and the size of the correction is not as exaggerated as the values at the tails.

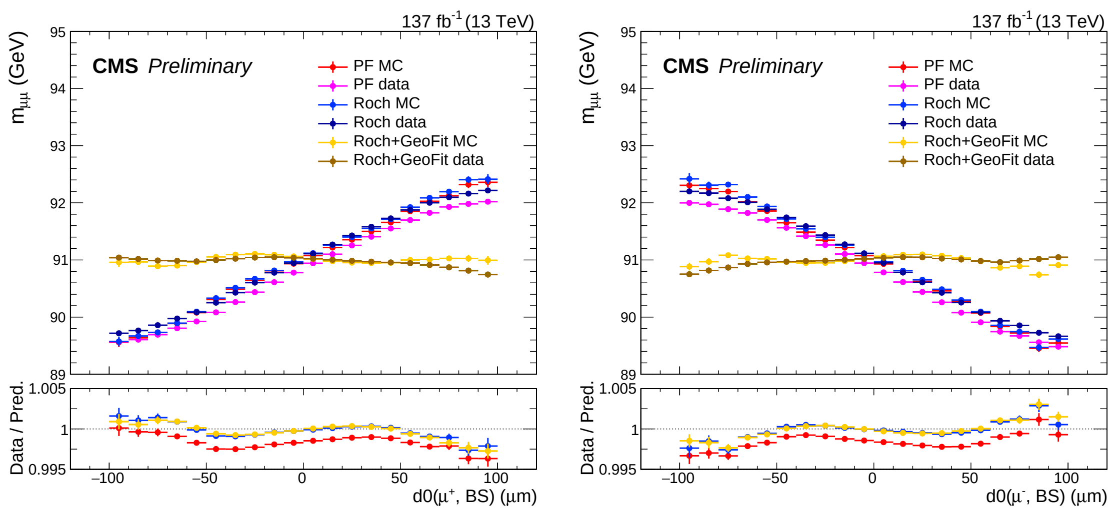

Figure 5-9. Plots showing the p_T dependence on the d0 value with different stages of muon correction. The plots compare the $Z \rightarrow \mu\mu$ peak in data and simulation for three years (2016-2018) combined. All positively charged muons are put in the left plot and all negatively charged ones are put in the right plot. The p_T-d0 dependence is reversed for positive and negative muons.

Overall, the removal of the p_T-d0 dependence leads to an improvement on the inclusive $m_{\mu\mu}$ resolution. This improvement is different for different processes depending on their kinematic profiles in p_T and $|\eta|$. Figure 5-10 shows the improvement on $m_{\mu\mu}$ resolution in the four main expected signal modes, ggH, VBF, VH, and $t\bar{t}H$. The relative improvements on $m_{\mu\mu}$ resolution for ggH, VBF, VH, and $t\bar{t}H$ modes are, respectively, 6.1%, 7.8%, 8.0%, and 9.8%. This improvement on signal resolution translates into about 5% improvement on the significance of the inclusive $H \to \mu\mu$ analysis.

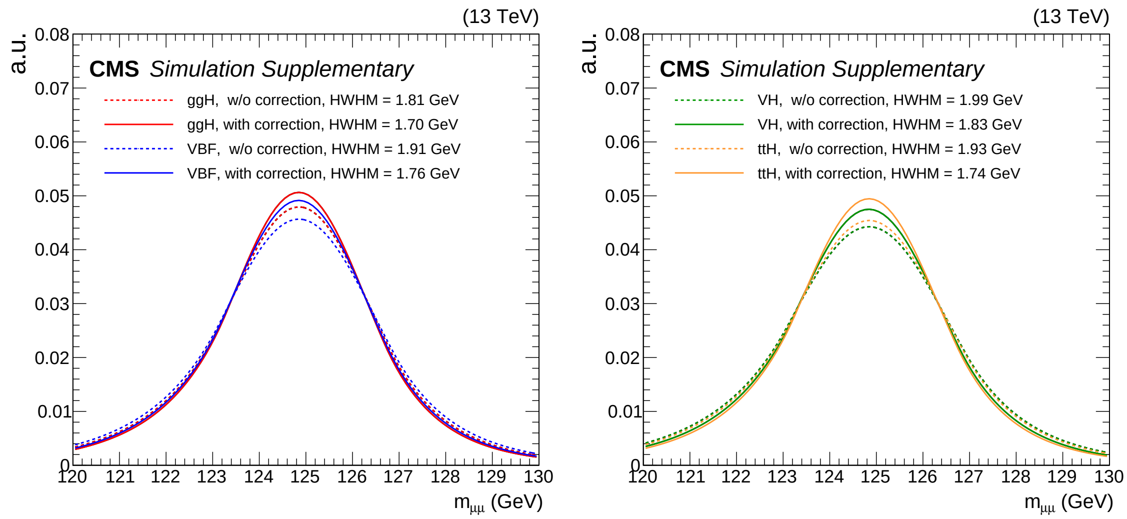

Figure 5-10. Plots showing the *GeoFit correction* improvement on the four main $H \to \mu\mu$ signal modes, ggH and VBF plotted on the left, and VH and $t\bar{t}H$ plotted on the right. The plots are made combining the expected signal in all three years of data-taking (2016-2018). The relative improvements on $m_{\mu\mu}$ resolution for ggH, VBF, VH, and $t\bar{t}H$ modes are, respectively, 6.1%, 7.8%, 8.0%, and 9.8%.

5.3.4 GeoFit vs track re-fit

The *GeoFit correction* provides a simple method to correct the p_T dependence on d0 based on high level physics variables. Since the origin of this p_T dependence is well-understood, it is also possible to derive a more fundamental correction by re-fitting each muon track including the BS position as an additional constraint to the track. This method requires lower-level information of muon reconstruction and is computationally more expensive, but is in principle more precise. To compare the performance of the *GeoFit correction* and the re-fitting method, a preliminary study is made on the 2018 ggH signal simulation. The $m_{\mu\mu}$ shape of the inclusive signal is plotted applying the track re-fit method vs applying the *GeoFit correction*, shown in Figure 5-11. This comparison shows that the $m_{\mu\mu}$ shapes from the two methods are almost equivalent. The *GeoFit correction*, although an approximation method, captures most of the effect and provides about the same improvement in $m_{\mu\mu}$ resolution as the re-fitting method. The *GeoFit correction* is therefore chosen in the H $\rightarrow \mu\mu$ analysis to speed up the workflow. In the meantime, the possibility of CMS centrally providing the re-fit results for more general use cases is under discussion, which may become an official option in Run 3 (2022-2024) of CMS data-taking.

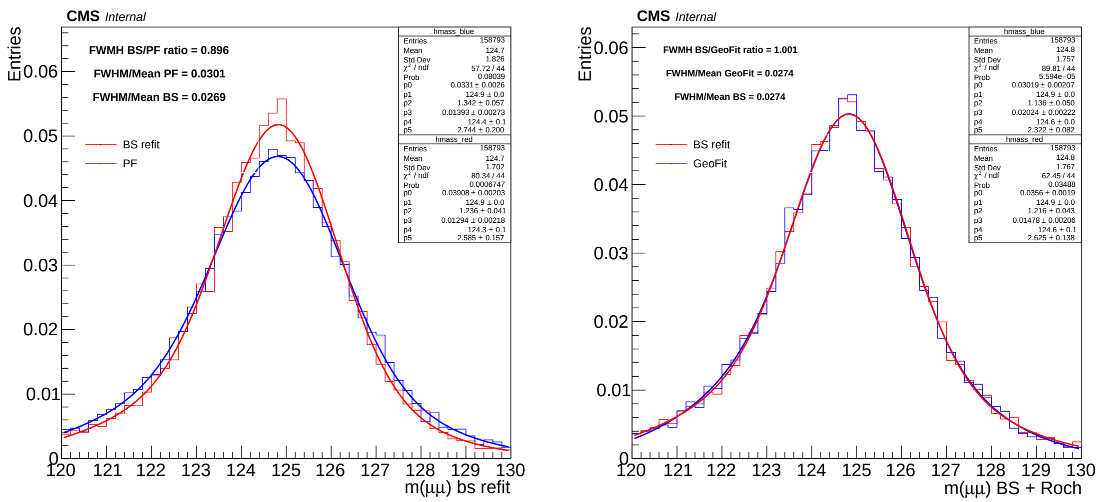

Figure 5-11. Plots of the $m_{\mu\mu}$ shape of the 2018 ggH simulation sample, comparing different muon correction methods. The left plot shows the $m_{\mu\mu}$ distribution calculated with muon tracks re-fit with the additional BS constraint, compared with the particle flow shape (left plot). The *Rochester correction* is not applied in the left plot for both the red and the blue lines. The right plot shows the $m_{\mu\mu}$ distribution from the re-fit method, with the *Rochester correction* applied, compared with the shape from *GeoFit correction* + *Rochester correction* (right plot). Plots credit to Pierluigi Bortignon.

5.4 Muon calibration results

The Z $\rightarrow \mu\mu$ is a well-understood process with a mass scale not far from the Higgs boson and with a much larger number of events in CMS. It is therefore used as a candle to monitor the performance of the *Rochester correction* and the *GeoFit correction*, and validate that these corrections do not introduce new biases. In this study, the distribution of the $m_{\mu\mu}$ is plotted in different bins of some dimuon kinematic variables. The $m_{\mu\mu}$ distributions are fit with a Voigtian + Exponential function, the Voigtian part being a convolution of a Breit-Wigner function and a Gaussian function. The parameters mean mass from the Breit-Wigner part and standard deviation from the Gaussian part are taken as the mean value and the experimental resolution of the $m_{\mu\mu}$ distribution, and are plotted against the dimuon kinematic variable of interest to check for potential trends.

The calibration plots are made by year as the corrections are provided by year. Events containing *FSR recovery* are removed from this study as it is a separate effect. Different variables are tested in the Figures listed: Figure 5-12 for the η of the positive muon, Figure 5-13 for the ϕ of the positive muon, Figure 5-14 for the ϕ of the negative muon, Figure 5-15 for the p_{T} of the positive muon, Figure 5-16 for the p_{T} of the dimuon system, Figure 5-17 for the η of the dimuon system, Figure 5-18 for the d0 of the positive muon, and Figure 5-19 for the d0 of the negative muon.

From these plots, it can be concluded that all the known biases in muon p_{T} are removed and no new bias has been introduced. The *Rochester correction* and *GeoFit correction* correct orthogonal effects, and do not interfere the performance of each other. After the corrections, a per-mille level agreement is achieved between data and simulation in the $m_{\mu\mu}$ value, while the agreement in $m_{\mu\mu}$ resolution is about a few percent.

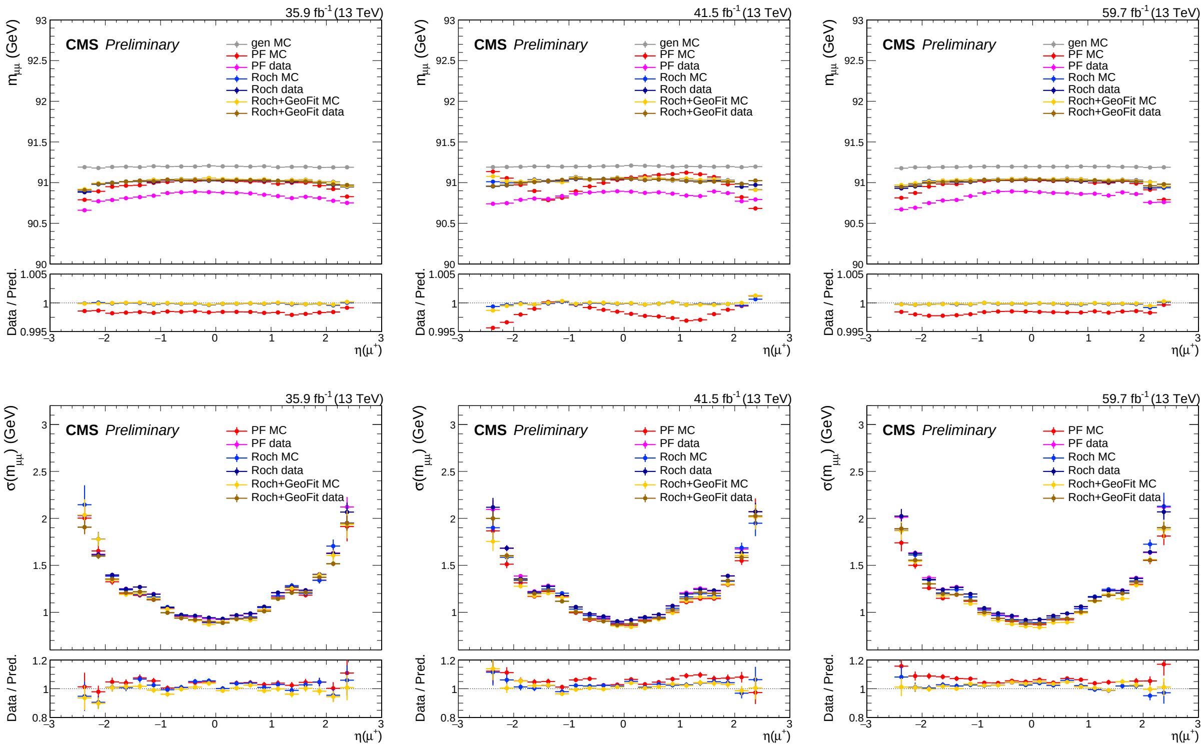

Figure 5-12. Muon calibration plots vs $\eta(\mu^+)$, for 2016 (left column), 2017 (middle column) and 2018 (right column). The top row shows the mean value of the Voigtian fit to the $m_{\mu\mu}$ distribution, while the bottom row shows its experimental resolution.

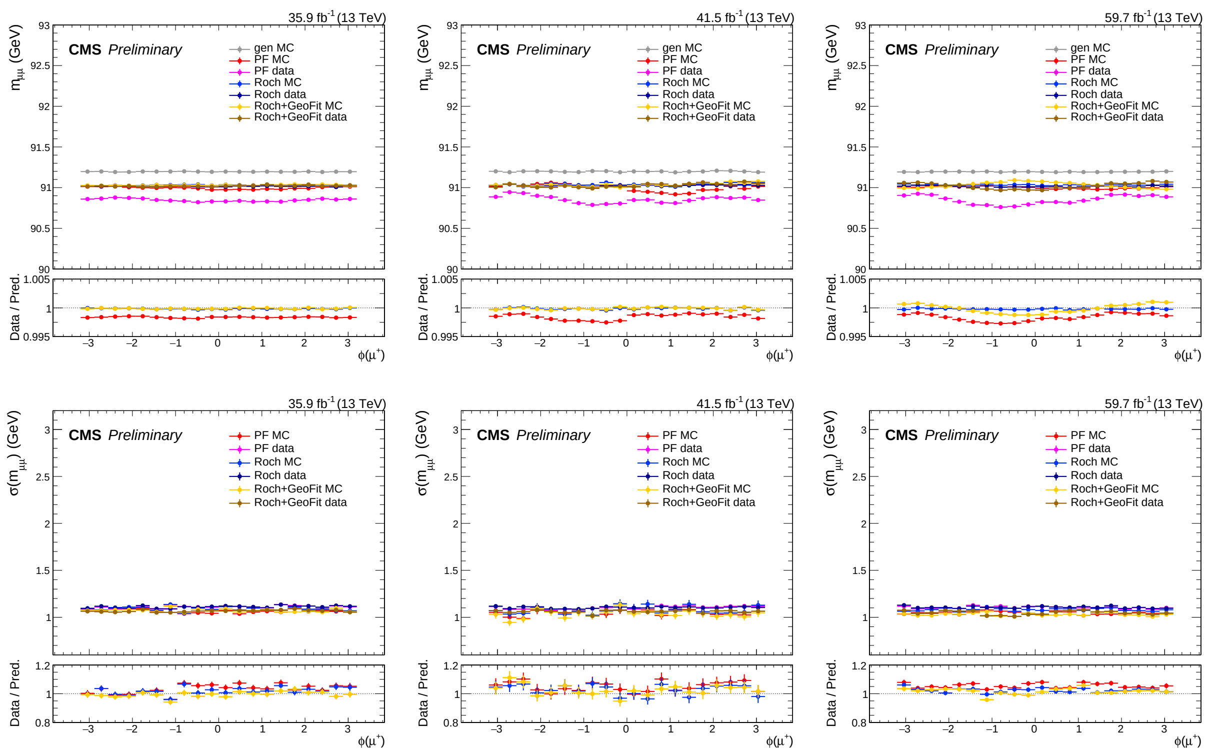

Figure 5-13. Muon calibration plots vs $\phi(\mu^+)$, for 2016 (left column), 2017 (middle column) and 2018 (right column). The top row shows the mean value of the Voigtian fit to the $m_{\mu\mu}$ distribution, while the bottom row shows its experimental resolution.

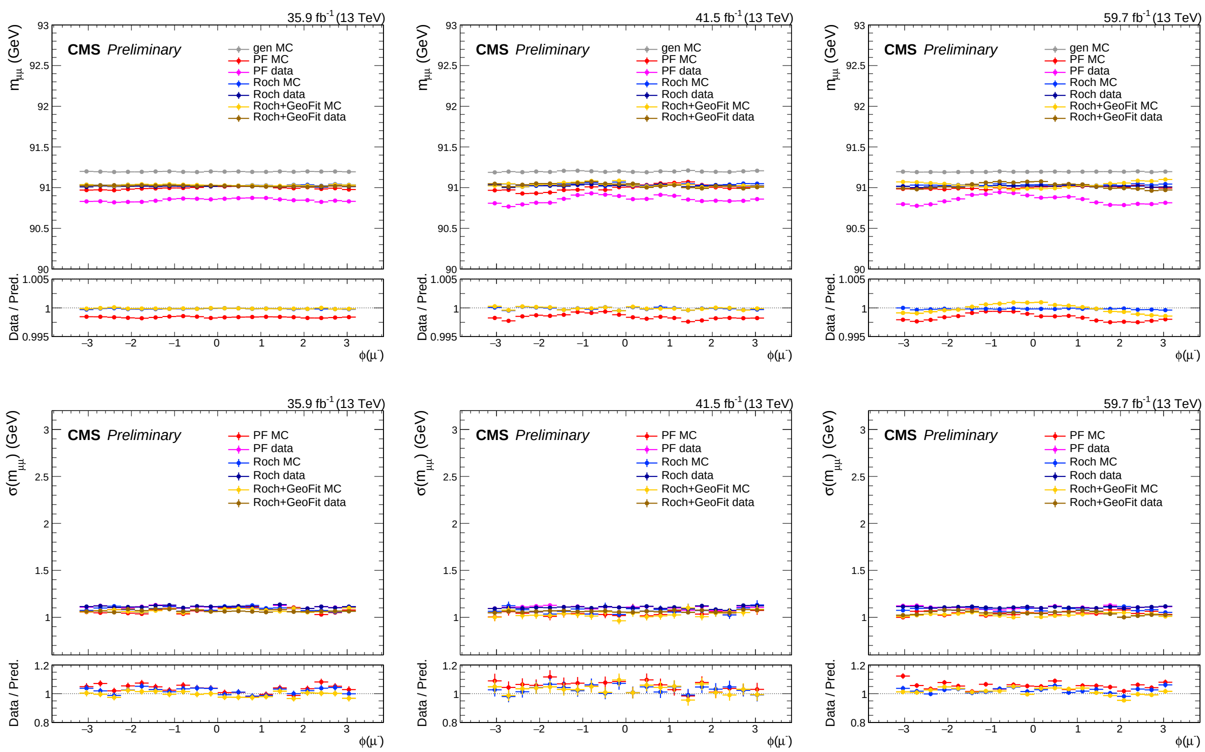

Figure 5-14. Muon calibration plots vs $\phi(\mu^-)$, for 2016 (left column), 2017 (middle column) and 2018 (right column). The top row shows the mean value of the Voigtian fit to the $m_{\mu\mu}$ distribution, while the bottom row shows its experimental resolution.

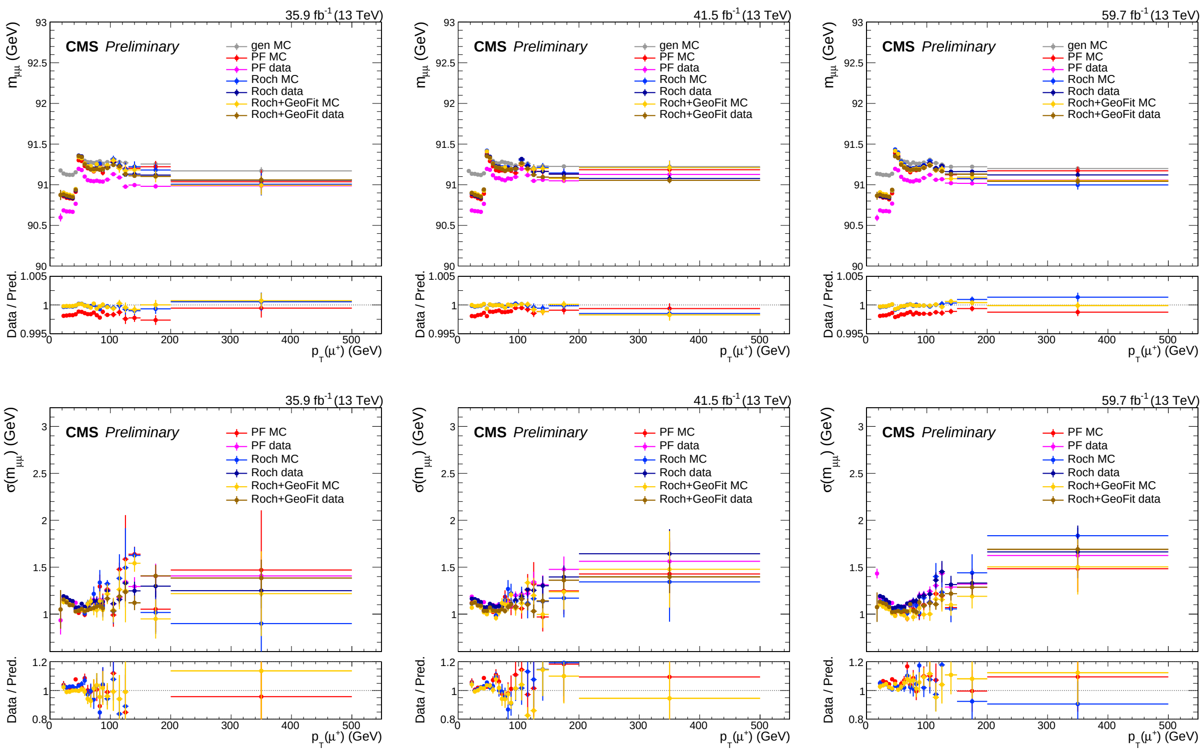

Figure 5-15. Muon calibration plots vs $p_\mathrm{T}(\mu^+)$, for 2016 (left column), 2017 (middle column) and 2018 (right column). The top row shows the mean value of the Voigtian fit to the $m_{\mu\mu}$ distribution, while the bottom row shows its experimental resolution. The p_T binning sculpts the shape of the $m_{\mu\mu}$ peak, which leads to a jump at the p_T = 45 GeV in the plots.

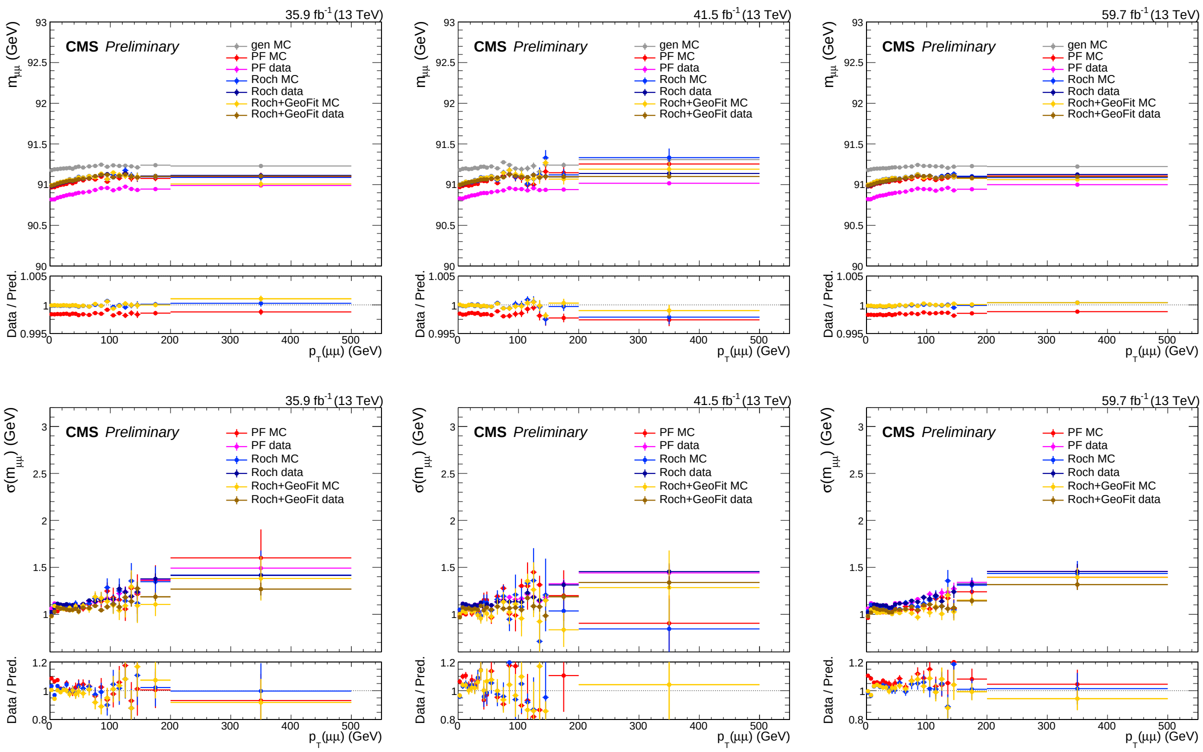

Figure 5-16. Muon calibration plots vs $p_{\mathrm{T}}(\mu\mu)$, for 2016 (left column), 2017 (middle column) and 2018 (right column). The top row shows the mean value of the Voigtian fit to the $m_{\mu\mu}$ distribution, while the bottom row shows its experimental resolution.

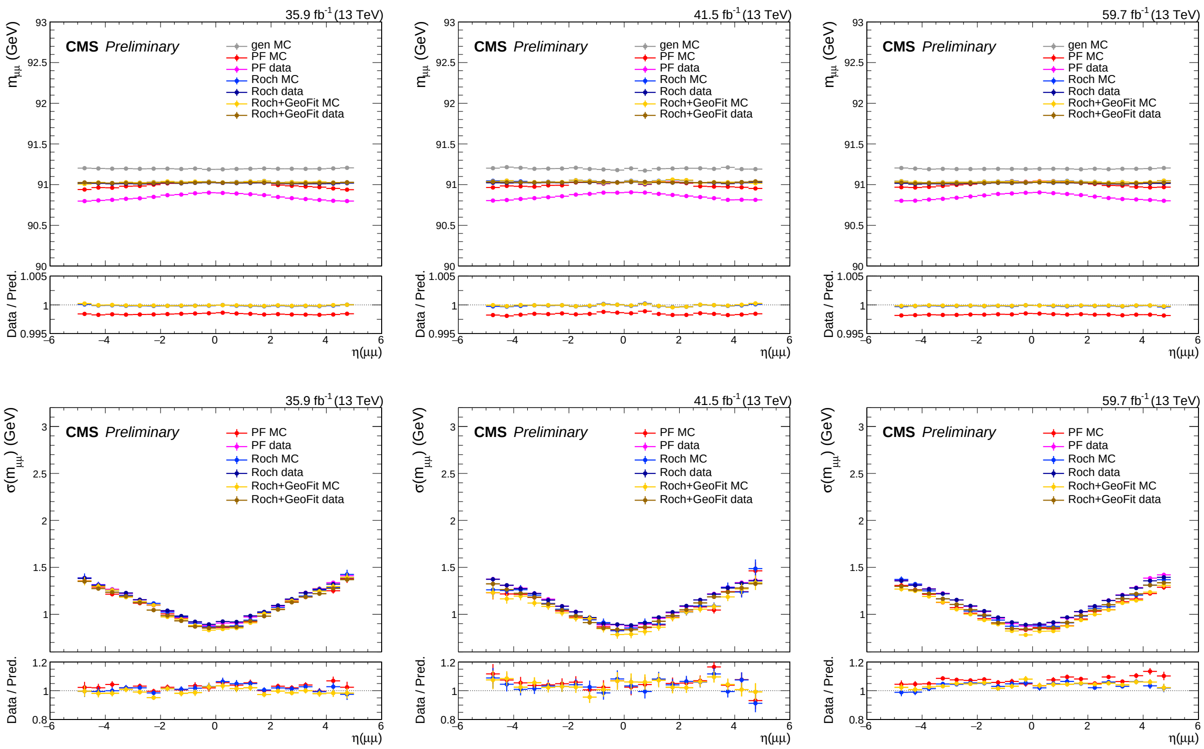

Figure 5-17. Muon calibration plots vs $\eta(\mu\mu)$, for 2016 (left column), 2017 (middle column) and 2018 (right column). The top row shows the mean value of the Voigtian fit to the $m_{\mu\mu}$ distribution, while the bottom row shows its experimental resolution.

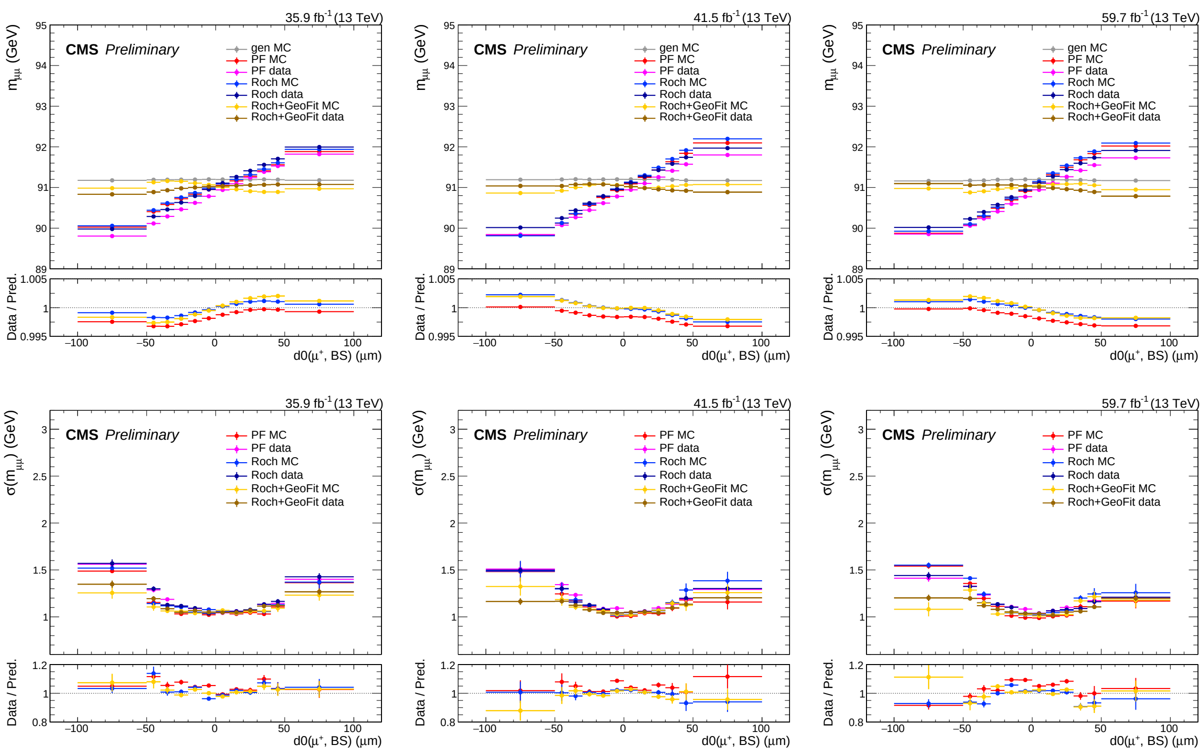

Figure 5-18. Muon calibration plots vs $d0(\mu^+)$, for 2016 (left column), 2017 (middle column) and 2018 (right column). The top row shows the mean value of the Voigtian fit to the $m_{\mu\mu}$ distribution, while the bottom row shows its experimental resolution.

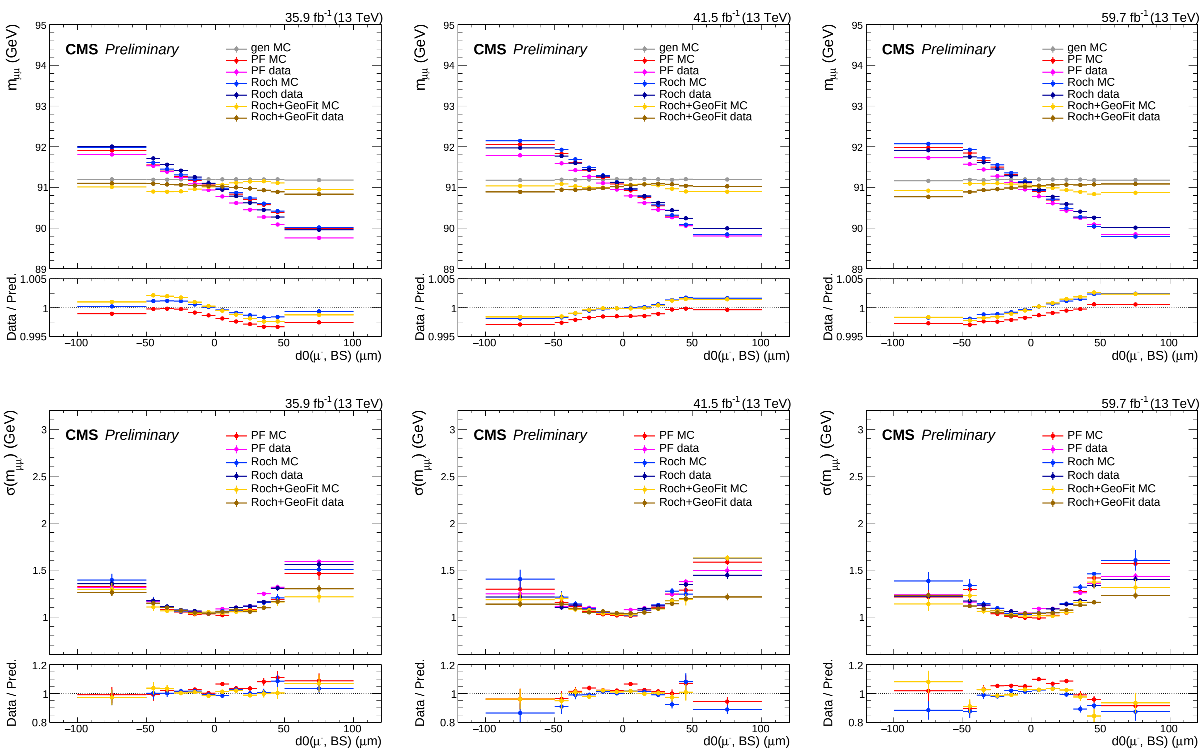

Figure 5-19. Muon calibration plots vs $d0(\mu^-)$, for 2016 (left column), 2017 (middle column) and 2018 (right column). The top row shows the mean value of the Voigtian fit to the $m_{\mu\mu}$ distribution, while the bottom row shows its experimental resolution.

CHAPTER 6
SEARCH FOR H2MU TARGETING THE VH PRODUCTION MODE

As described in Section 3.2, the analysis in the VH category targets the VH production modes of the Higgs boson, and is established as two independent parts, the WH category and the ZH category. This chapter provides a full description of the procedures and the results in these two categories. In this chapter the VH category will sometimes be referred to as the VH categories, when we focus more on the individual specifications of the WH and ZH categories, rather than their common characteristics.

The VH analyses focus on the leptonic (e or μ) decay modes of the V boson (W or Z), which leads to distinct final states involving extra well-reconstructed charged lepton(s) in addition to the two muons from the Higgs decay. By requiring these additional leptons, the main backgrounds in the generic $\mu\mu$ phase-space, the DY and the $\mathrm{t\bar{t}}$ processes, are greatly suppressed, leading to a high S/B in the VH categories, and ensuring a good expected significance with only a handful of signal events. The other decay modes of the V boson are disregarded for different reasons:

The V bosons decay to tau leptons ($\mathrm{W} \to \tau + \nu_\tau$, or $\mathrm{Z} \to \tau\bar{\tau}$) at the same rate as they decay to electrons or muons. However, in CMS, the reconstruction of τ is not as efficient as that of electrons or muons: the reconstruction of the hadronic decays of τ suffers from a sizable fake rate, while the leptonic decays of τ would just appear as an electron or a muon of much lower p_T. Tagging the hadronic decays of taus from the W or Z decay would lead to a much lower S/B than the e and μ tags in the current VH analyses, bringing negligible contribution to the overall sensitivity. As for the leptonic decays of τ, they are not explicitly vetoed. If any VH signal events containing such decays pass the selection, they are considered as part of the signal contribution. Although, this contribution is small, as the e or μ from the τ decay would most likely fail the p_T or the vertex proximity cuts.

The hadronic decays of the W or the Z boson lead to two jets in the event, making an invariant mass near the mean mass of the boson. Although amounting to a larger branching ratio than the leptonic decay modes, these hadronic decays turned out not as helpful in enriching the VH events. A selection based on the dijet invariant mass could pick most of the VH events, but in the meantime collect a much larger amount of ggH+jets and VBF events, as well as an immense background of DY+jets and $t\bar{t}$ processes. The S/B from this selection is not very high, as this phase-space is dominated by ggH+jets vs DY+jets events. Up to the time of this report, no kinematic handle is found to be particularly effective in enriching the hadronic VH signal. Therefore, the hadronic VH events are considered as minor signal contributions in the ggH category, and no dedicated VH hadronic tag is deployed.

The Z boson can decay to a pair of neutrinos at a branching ratio of 20%, which leave no electronic signal in the CMS detector and appear as a missing transverse momentum ($E_{\mathrm{T}}^{\mathrm{miss}}$) in the event. This $E_{\mathrm{T}}^{\mathrm{miss}}$ equals to the p_{T} of the Z boson and can provide discrimination against some backgrounds. However, due to the complex hadronic activity in pp collisions and the large uncertainty in the hadronic calorimetry in CMS, almost all events are reconstructed with some nonzero $E_{\mathrm{T}}^{\mathrm{miss}}$, even for events without any real $E_{\mathrm{T}}^{\mathrm{miss}}$, like the DY events. As a result, the purity of the ZH $\rightarrow \nu\nu + \mu\mu$ signal can only be enhanced if a very tight cut on the $E_{\mathrm{T}}^{\mathrm{miss}}$ is applied. The signal efficiency for this cut is, unfortunately, low, because only a small fraction of the Z bosons in ZH events have high p_{T}. Furthermore, after this cut, some large irreducible backgrounds still remain, like the $t\bar{t}$ and diboson processes. Overall, a tag for the ZH $\rightarrow \nu\nu + \mu\mu$ would be much less sensitive than the existing ZH $\rightarrow \ell\ell + \mu\mu$ tag, and is not deployed. The ZH $\rightarrow \nu\nu + \mu\mu$ signal events are considered as minor signal contributions in the ggH category.

After requiring additional lepton(s) in the event, the main background in the resulting VH phase-spaces becomes the WZ and ZZ processes, for the WH and ZH categories respectively. For both WZ and ZZ backgrounds, if more than two muons are present in the event, there are different possibilities of the association between the muons and their parent particles. In fact, the wrong pairing of muons, called the combinatorial background, yields the majority of the WZ and ZZ background. For example, in an on-shell WZ event, the muon from the W decay can be falsely paired with the oppositely signed (OS) muon from the Z decay, making an invariant mass near the Higgs mass value. A set of cut-based event selection is optimized to reduced the combinatorial background, further improving the S/B. More details are given in Section 6.1.

The minor backgrounds may include the triboson processes, the DY process accompanied with additional non-prompt leptons, or the t quark associated processes, for example the $\mathrm{t\bar{t}}$, tW, and $\mathrm{t\bar{t}V}$ processes, where the b quarks from the top decays either fall out of the acceptance of the detector or fails the b-tagging. All these minor backgrounds have different kinematic profiles from the signal and can be reduced to different extents. Boosted Decision Tree (BDT) discriminators are trained in both the WH and the ZH categories to account for the differences between the signal and the inclusive background as much as possible.

With the BDT discriminators, events are further divided in to several sub-categories with different S/B. In each sub-category, the $m_{\mu\mu}$ spectrum is plotted, and analytic functions are used to model the shapes of signal and background. The strength of the $\mathrm{H} \rightarrow \mu\mu$ signal is evaluated by fitting the signal and the background functions to the $m_{\mu\mu}$ spectrum of data. Combining the results in all WH and ZH sub-categories, an observed (expected in absence of $\mathrm{H} \rightarrow \mu\mu$ decay) upper limit of 10.8 (5.13) times the SM prediction is set at the 95% confidence level (CL) on the product of the Higgs boson production cross section and $\mathscr{B}(\mathrm{H} \rightarrow \mu\mu)$. The corresponding signal strength, relative to the SM prediction, is $\mu = 5.48^{+3.10}_{-2.83}$. An excess of signal events is observed (expected with the SM prediction) with a significance of 2.02 (0.42) standard deviations.

The following sections of this chapter are organized as follows: Section 6.1 describes the event selection. Section 6.2 discusses the details of the training of the BDTs, and the determination of sub-categories based on them. Section 6.4 shows the performances of different analytic functions on the signal and background modeling. Section 6.5 lists different sources of systematic uncertainties considered in this analysis. And Section 6.6 gives the statistical interpretation of the results.

6.1 Event selection

The VH analysis takes physics objects reconstructed by the particle-flow (PF) algorithm [73]. Selections on the objects are described in details in Chapter 4. The selection criteria for electrons and muons, which are the most important for this analysis, are also summarized in Table 6-1.

Table 6-1. Selection criteria on muons and electrons in the VH analysis.

Variable	Muon	Electron
p_{T}	$> 20\mathrm{GeV}$	$> 20\mathrm{GeV}$
$\lvert\eta\rvert$	< 2.4	< 2.5
ID and Iso	Medium ID + Loose Iso	MVA wp90
ECal gap veto	-	$(1.444, 1.566)$
d_{xy}(PV)	< 0.05 cm	< 0.05 cm
d_z(PV)	< 0.10 cm	< 0.10 cm
SIP	< 8.0	< 8.0
Conversion Veto	-	✓
Number of Missing Hits	-	< 2
lepMVA	> 0.4	> 0.4

The event selection targets the leptonic decays of the W or the Z bosons in the VH signals. The selection steps are deviced to suppress different background processes and optimize the S/B in the WH and ZH categories respectively. The event selection in the $\mathrm{WH} \to \ell\nu + \mu\mu$ category is described as follows:

- At least one muon must have $p_{\mathrm{T}} > 26\mathrm{GeV}/29\mathrm{GeV}/26\mathrm{GeV}$ for year 2016/2017/2018 respectively, which is matched to a single-muon trigger object
- All SFOS lepton pairs must have an invariant mass > 12 GeV
- The charge of the three leptons must add up to ± 1
- At least one $\mu^+\mu^-$ pair must have an invariant mass between 110 and 150 GeV
- If two $\mu^+\mu^-$ pairs fall in the 110 - 150 GeV mass window, the pair with the higher p_{T} is chosen as the Higgs candidate (denoted $\mu\mu_{\mathrm{H}}$)
- The event must contain exactly 0 medium b-tagged jet and less than 2 loose b-tagged jets
- In 3μ events, the non-Higgs-candidate $\mu^+\mu^-$ pair ($\mu\mu_{OS}$) must not have an invariant mass between 81 and 101 GeV, to suppress WZ and Z+jets backgrounds

The event selection in the $\mathrm{ZH} \rightarrow \ell\ell + \mu\mu$ category is described as follows:

- At least one muon must have $p_{\mathrm{T}} > 26\mathrm{GeV}/29\mathrm{GeV}/26\mathrm{GeV}$ for year 2016/2017/2018 respectively, and the event must contain an unprescaled single-muon trigger object
- The charge of the four leptons must add up to 0.
- All SFOS lepton pairs must have an invariant mass > 12 GeV.
- In $\mu\mu ee$ events, the e^+e^- pair must have invariant mass between 70 and 110 GeV, and the $\mu^+\mu^-$ pair must have invariant mass between 110 and 150 GeV.
- In 4μ events, if it is possible to form two distinct $\mu^+\mu^-$ pairs each with a mass between 81 and 101 GeV, the event is discarded.
- In 4μ events, one muon pair must have mass between 110 and 150 GeV, and the other muon pair must have mass between 81 and 101 GeV.
- In 4μ events, if both combinations have a muon pair in the Z-mass window and a muon pair in the signal-mass window, the combination in which the mass of the Z candidate is closer to 91 GeV is chosen.
- The event must contain exactly 0 medium b-tagged jet and less than 2 loose b-tagged jets.

These selection criteria are also summarized in Table 6-2.

Table 6-2. Event selections for the WH and ZH categories.

Criterion	WH category	ZH category
Muon trig match	✓	✓
b-jets veto, 0 medium and < 2 loose	✓	✓
$\mu^+\mu^-$ pair with $110 < m_{\mu\mu} < 150$ GeV	✓	✓
Additional lepton(s)	1	1 SFOS pair
Low-mass resonance veto $m_{\ell\ell} > 12$ GeV	✓	✓
Number of $\lvert m_{\mu\mu} - m_{\mathrm{Z}}\rvert < 10$ GeV or $\lvert m_{\mathrm{ee}} - m_{\mathrm{Z}}\rvert < 20$ GeV	$= 0$	$= 1$
Choice of muon combination	Highest $p_T(\mu\mu)$ as $\mu\mu_{\mathrm{H}}$	Smallest $\lvert m_{\mu\mu} - m_{\mathrm{Z}}\rvert$ as $\mu\mu_{\mathrm{Z}}$

6.2 MVA discrimination

After the event selection of the WH or the ZH categories, the remaining background processes resemble the kinematic signatures of the signals and cannot be decisively reduced by simple selection cuts. To further suppress the backgrounds and enhance the S/B, a BDT is trained in each category, making use of the many lesser discriminating variables.

Different variables can be effective in separating different background processes. For example, the muon pair from t quark associated processes usually have more p_{T} than those from the WH signal process, while the $E_{\mathrm{T}}^{\mathrm{miss}}$ in the DY process is likely to be smaller than that in the WH events. The main background, WZ or ZZ in the WH and ZH categories respectively, in which the Higgs candidate $\mu\mu$ pair comes from an off-shell Z boson, is a more complicated story as it looks almost kinematically identical to the signal. The key in discriminating them lies in the spin difference between the Z and the H bosons, which is measured as a difference in the helicity angle θ^* between the decay products of the Z (H) boson.

The helicity angle is defined in a decay system in the frame in which the parent particle is at rest, as the angle between the direction of the decay and the boost direction of the parent particle. The distribution of this angle is determined by the spins of the parent particle and the decay products. In the case of $\mathrm{W} \to \mathrm{WZ}$ ($\mathrm{Z} \to \mathrm{ZZ}$) vs $\mathrm{W} \to \mathrm{WH}$ ($\mathrm{Z} \to \mathrm{ZH}$), the helicity angle between the W (Z_1) and the Z_2 follows the distribution $1 + cos^2\theta^*$ while the the helicity angle between the W (Z) and the H follows a flat distribution. Similarly, for $\mathrm{Z} \to \mu\mu$ vs $\mathrm{H} \to \mu\mu$, the muons from a Z decay tend to align with the polarization of the Z boson, while the muons from a H decay do not have a preference in direction.

All these helicity angles, θ^*_{WH}, θ^*_{ZH}, and $\theta^*_{\mu\mu}$, can in principle provide significant discrimination between the signal and the background. However, in practice, θ^*_{WH} cannot be reconstructed due to the lack of information of the neutrino from the W decay, and the distribution of $\theta^*_{\mu\mu}$ is severely sculpted by the acceptance of the CMS detector, rendering a similar shape for the $\mathrm{Z} \to \mu\mu$ and $\mathrm{H} \to \mu\mu$ processes. On the other hand, the spin information can be partially captured in other variables, for example the helicity angle between the W-lepton and the $\mu\mu_{\mathrm{H}}$ system, and some other angular correlations like $\Delta\phi$, $\Delta\eta$. All these variables are tested as inputs to the BDT for the performance. Some of them turned out insignificant and are later trimmed off from the input collection. To make sure the BDTs do not sculpt the $m_{\mu\mu}$ shape, which will be used for the signal extraction, variables which are strongly correlated with $m_{\mu\mu}$, for example the p_{T} of the muons, are not used in the BDTs.

6.2.1 BDT targeting $\mathrm{WH} \to \ell\nu + \mu\mu$ signal

The WH BDT takes variables of three different kinds, the kinematic variables of leptons which are uncorrelated with $m_{\mu\mu}$, the angular correlations between different leptons as discussed above, and the variables reflecting the missing energy in the event. In total, there are 16 input variables to the BDT, which are listed in Table 6-3. The variables related to the missing energy includes the missing energy itself, the transverse mass (M_{T}) between a lepton and the missing energy, and the angular separation between a lepton and the missing energy. Two types of missing energy are tested, $E_{\mathrm{T}}^{\mathrm{miss}}$, which is the inverse of the sum of the transverse energy of all PF candidates, and $H_{\mathrm{T}}^{\mathrm{miss}}$, which only considers well-defined jets, photons, and leptons in the similar calculation. The $E_{\mathrm{T}}^{\mathrm{miss}}$-related and $H_{\mathrm{T}}^{\mathrm{miss}}$-related variables are expected to play interchangeable roles in the BDT. The $H_{\mathrm{T}}^{\mathrm{miss}}$-related variables turned out to be slightly better performing and are kept in the final BDT, while the $E_{\mathrm{T}}^{\mathrm{miss}}$-related variables are trimmed.

Another important feature in the WH category is that about 40% of the WZ background are from the wrong combination of muons in 3μ events. The duplication of some variables calculated with the alternative combination of the muons in each event may also help with the discrimination. For example, apart from the transverse mass between the nominal W-lepton and the the $H_{\mathrm{T}}^{\mathrm{miss}}$, another transverse mass is also considered, using the $H_{\mathrm{T}}^{\mathrm{miss}}$ and the same-sign muon from the nominal Higgs candidate, which turns out to be effective.

The sensitivity of this analysis depends largely on the resolution of the $m_{\mu\mu}$ peak, which is determined by muon momentum resolution, which in turn primarily depends on η of the muons as the detector condition differs in different η regions in CMS. It is important to divide events with different resolution into different categories, which leads to an enhancement to the overall S/B. In the previous $\mathrm{H} \to \mu\mu$ analysis [34, 89], the categorization is achieved by dividing events based on both the BDT output and the η value of the muons. While in this work, the resolution information is incorporated into the

BDT, not as an input variable, but by weighting the signal events by $1/\sigma(m_{\mu\mu})$, which is the per-event experimental dimuon mass resolution, calculated from the p_{T} uncertainty of the muon tracks. In this way, the BDT output encapsulates both the kinematic information and the resolution information in its output, allowing for a categorization based on a single variable, achieving a better significance with fewer categories. The resolution is not used as an direct input to the BDT because its distribution is not very different between signal and background. The weights are only applied in the training on signal events, and not applied in the evaluation of the BDT score.

The BDT is trained with a collection of simulated samples from all eras in Run 2. The training is performed in the mass window of 110 GeV $< m_{\mu\mu} <$ 150 GeV. To make sure the BDT is not sensitive to the $m_{\mu\mu}$ value, signal samples with different Higgs mass assumptions, $m_{\mathrm{H}} = 120, 125, 130$ GeV, are all used as signals in the training. Signal events are only used if the candidate $\mu\mu$ pair truly originates from the Higgs decay, so that the BDT only picks the true kinematic signatures of the signal. No parent matching is required for backgrounds. To benefit from the maximal statistics in simulation while keeping sensitive to all kinematic features, events with $e+\mu\mu$ and $\mu+\mu\mu$ are used together in the training, but can be distinguished by the "number of electrons" as one of the input variables to the BDT. To increase the statistics of the non-prompt backgrounds in the simulated events, the lep-MVA cut is loosened from 0.4 to -0.4 for the training collection, and the non-prompt yields are scaled by a factor of 0.5 to account for the increased non-prompt lepton efficiency. For both the signal and background samples, half of the events is used for the training, while the other half is used for the testing.

The BDT output and its Receiver Operating Characteristic (ROC) curve are shown in Figure 6-1, in which the BDT performs the same on training and testing samples, indicating no over-training. Distributions of the BDT input variables are shown in Figures 6-2.

Table 6-3. List of input variables used to train the signal-background separation BDT in the WH category. In this table, $\mu\mu_{\mathrm{H}}$ is the Higgs candidate, ℓ is the lepton from the W decay, μ_{OS} (μ_{SS}) refers to the muons in the Higgs candidate which OS (SS) to the lepton.

Variable	Description
$p_{\mathrm{T}}(\mu\mu_{\mathrm{H}})$	p_{T} of the Higgs candidate
$\|\eta(\mu_1)\|$	η of the leading muon in the Higgs candidate
$\|\eta(\mu_2)\|$	η of the trailing muon in the Higgs candidate
$\Delta\mathrm{R}(\mu_{SS}, \mu_{OS})$	ΔR between the two muons in the Higgs candidate
p_{T} (ℓ)	p_{T} of the extra lepton in the event
Number of electrons	Number of electrons in the event
$\Delta\mathrm{R}(\ell, \mu\mu_{\mathrm{H}})$	ΔR between the extra lepton and the Higgs candidate
$\Delta\eta(\ell, \mu\mu_{\mathrm{H}})$	$\Delta\eta$ between the extra lepton and the Higgs candidate
$\Delta\eta(\ell, \mu_{SS})$	$\Delta\eta$ between the extra lepton and the SS muon
$\cos\theta^*(\ell, \mu_{SS})$	$\cos\theta^*$ between the extra lepton and the SS muon
$\Delta\mathrm{R}(\ell, \mu_{OS})$	ΔR between the extra lepton and the OS muon
$\Delta\eta(\ell, \mu_{OS})$	$\Delta\eta$ between the extra lepton and the OS muon
$\cos\theta^*(\ell, \mu_{OS})$	$\cos\theta^*$ between the extra lepton and the OS muon
$M_{\mathrm{T}}(\mu_{SS}$,MHT)	transverse mass of the $H_{\mathrm{T}}^{\mathrm{miss}}$ and the SS muon
$M_{\mathrm{T}}(\ell$,MHT)	transverse mass of the $H_{\mathrm{T}}^{\mathrm{miss}}$ and the extra lepton
$\|\Delta\phi(\ell$,MHT)$\|$	$\|\Delta\phi\|$ between the $H_{\mathrm{T}}^{\mathrm{miss}}$ and the extra lepton

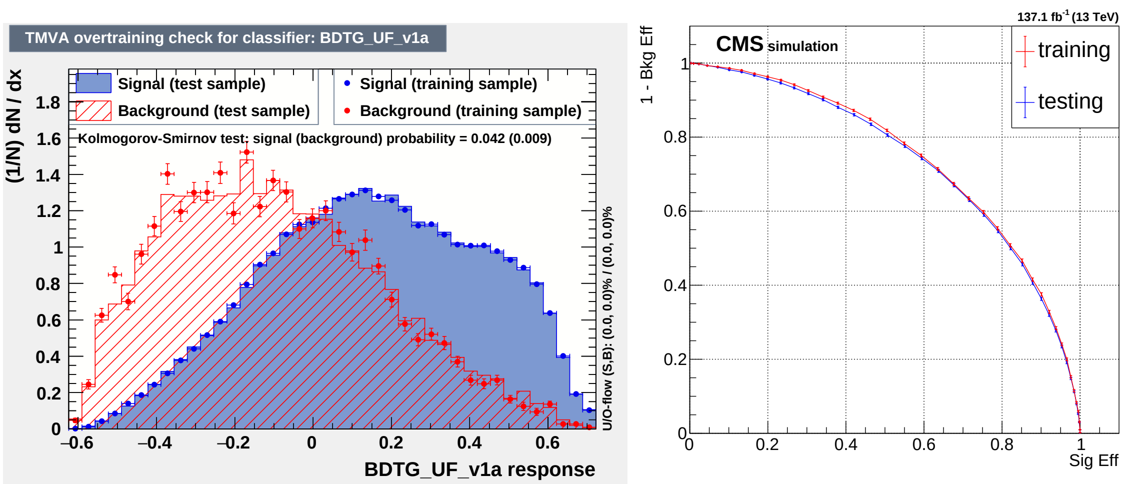

Figure 6-1. Plots of the performance of the WH $\rightarrow 3\ell$. On the left, the BDT output score, with signal in blue and background in red. On the right, the receiver operating characteristic (ROC) curve, with training sample in red and testing sample in blue. A slight over-training is observed in the region of low signal efficiency, due to the fluctuation in background. As will be shown in Fig. 6-5, the BDT dose not sculpt the shape of $m_{\mu\mu}$.

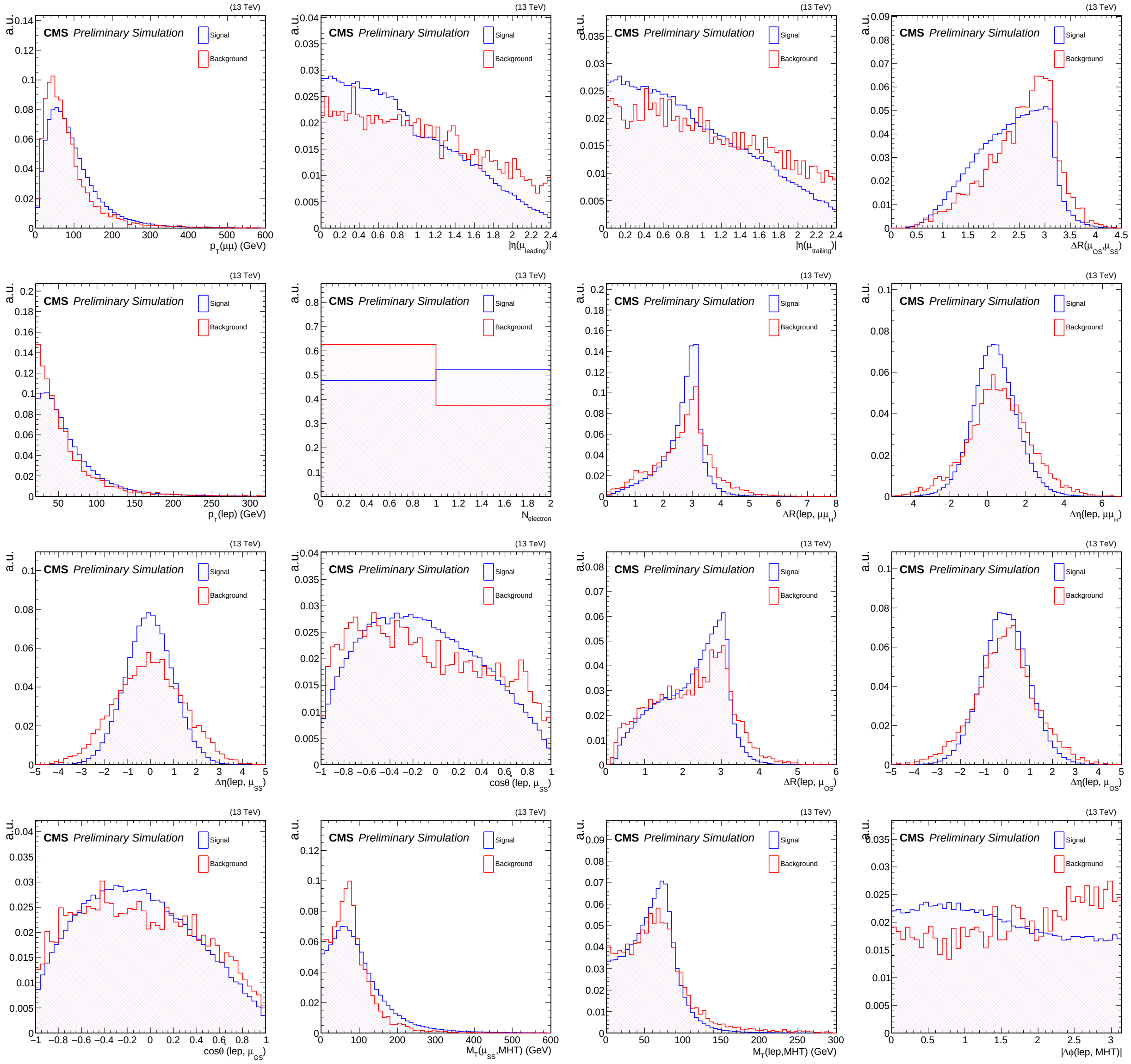

Figure 6-2. Input variables to the WH $\rightarrow 3\ell$ BDT, with signal in blue and background in red.

6.2.2 BDT targeting ZH $\rightarrow \ell\ell + \mu\mu$ signal

After the event selection of the ZH category, the background is almost purely composed of ZZ $\rightarrow 4\ell$ and ggZZ $\rightarrow 4\ell$ processes. Other backgrounds, prompt or non-prompt, have negligible contribution in this channel. Both ZZ and ggZZ processes have the identical final states as the ZH signal. Apart from the dimuon mass, which is used in the last stage for signal extraction, the most distinct discrimination between the signal and the background lies in the helicity angles, between the leptons from the H (Z) decay, and between the H (Z_1) and the Z_2 bosons.

The input variables to the BDT are listed in Table 6-4 and shown in Figure 6-4, among which, $\cos\theta^*(\mu\mu_{\mathrm{H}}, \ell\ell_{\mathrm{Z}})$, the helicity angle between the Higgs candidate and the Z candidate, is one of the most discriminating. In the ZZ background process, a propagator Z boson (Z_0) decays to two Z bosons (Z_1 and Z_2), which in turn decays to lepton pairs. Since Z bosons are spin-1 particles, in the $Z_0 \to Z_1 Z_2$ process, the direction of the decay is more likely to align with the direction of the momentum of Z_0. Whereas in the ZH events, since the Higgs bosons are spin-0 particles, there is no preferred direction for the the $Z_0 \to Z_1\mathrm{H}$ decay. A similar kinematic discrimination is also present in the helicity angle $\cos\theta^*(\mu_1, \mu_2)$, between the $\mathrm{Z} \to \mu\mu$ decay and the $\mathrm{H} \to \mu\mu$ decay, where in the Z decay the muons prefer to align with the momentum of their parent and in the H decay they follow a flat distribution. However, in this analysis, due to the acceptance of the CMS detector, the distribution of $\cos\theta^*(\mu_1, \mu_2)$ is sculpted and turns out not very different between signal and background. This variable is included in the initial training and later discarded during the variable trimming process.

Similar to the WH BDT training, as described in Section 6.2.1, the training is performed with simulated samples from all eras in Run2. The training is performed in the mass window of 110 GeV $< m_{\mu\mu} <$ 150 GeV. This training was performed prior to the production of ggZH signal samples, so only qqZH samples are used as signal events. Signal samples with different Higgs mass assumptions, $m_{\mathrm{H}} = 120, 125, 130$ GeV, are used. Signal events are only used if the candidate $\mu\mu$ pair truly originates from the Higgs decay. Signal events are weighted by $1/\sigma(m_{\mu\mu}^H)$. Events with $ee+\mu\mu$ and $\mu\mu+\mu\mu$ are used together in the training, but can be distinguished with the "lepton flavor" as one of the input variables. To increase the statistics of training events, the lepMVA cut is loosened from 0.4 to -0.4. Even so, there is no non-prompt background component passing the loosened selection.

The BDT output and the ROC curve are shown in Figure 6-3, in which the BDT performs the same on training and testing samples, indication no over-training. Distributions of the BDT input variables are shown in Figure 6-4.

Table 6-4. List of input variables used to train the signal-background separation BDT in the ZH category. In this table, $\mu\mu_{\mathrm{H}}$ is the Higgs candidate, and $\ell\ell_{\mathrm{Z}}$ is the Z candidate.

Variable	Description
p_{T} $(\mu\mu_{\mathrm{H}})$	p_{T} of the Higgs candidate
$\lvert\eta(\mu\mu_{\mathrm{H}})\rvert$	$\lvert\eta\rvert$ of the Higgs candidate
$\lvert\Delta\phi(\mu\mu_{\mathrm{H}})\rvert$	$\lvert\Delta\phi\rvert$ between the muons in the Higgs candidate
$\mathrm{M}(\ell\ell_{\mathrm{Z}})$	invariant mass of the Z candidate
p_{T} $(\ell\ell_{\mathrm{Z}})$	p_{T} of the Z candidate
$\lvert\eta(\ell\ell_{\mathrm{Z}})\rvert$	$\lvert\eta\rvert$ of the Z candidate
$\Delta\mathrm{R}(\ell\ell_{\mathrm{Z}})$	ΔR between the leptons in the Z candidate
lepton flavor	flavor of the Z candidate lepton pair
$\cos\theta^*(\mu\mu_{\mathrm{H}}, \ell\ell_{\mathrm{Z}})$	cosine helicity angle between the Higgs and the Z candidates
$\Delta\eta(\mu\mu_{\mathrm{H}}, \ell\ell_{\mathrm{Z}})$	$\Delta\eta$ between the Higgs and the Z candidates

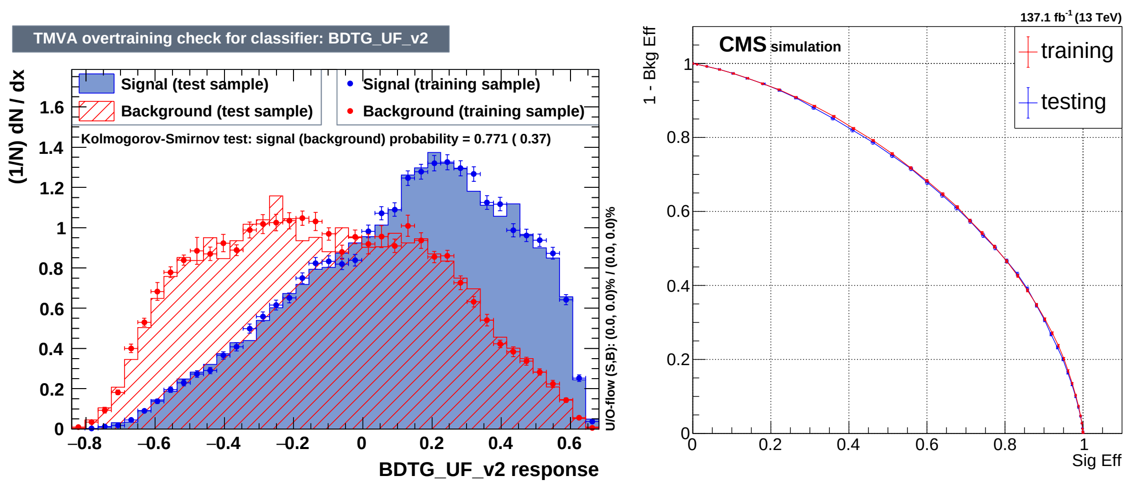

Figure 6-3. Plots of the performance of the ZH $\rightarrow 4\ell$ BDT. On the left, the BDT output score, with signal in blue and background in red. On the right, the receiver operating characteristic (ROC) curve, with training in red and testing in blue.

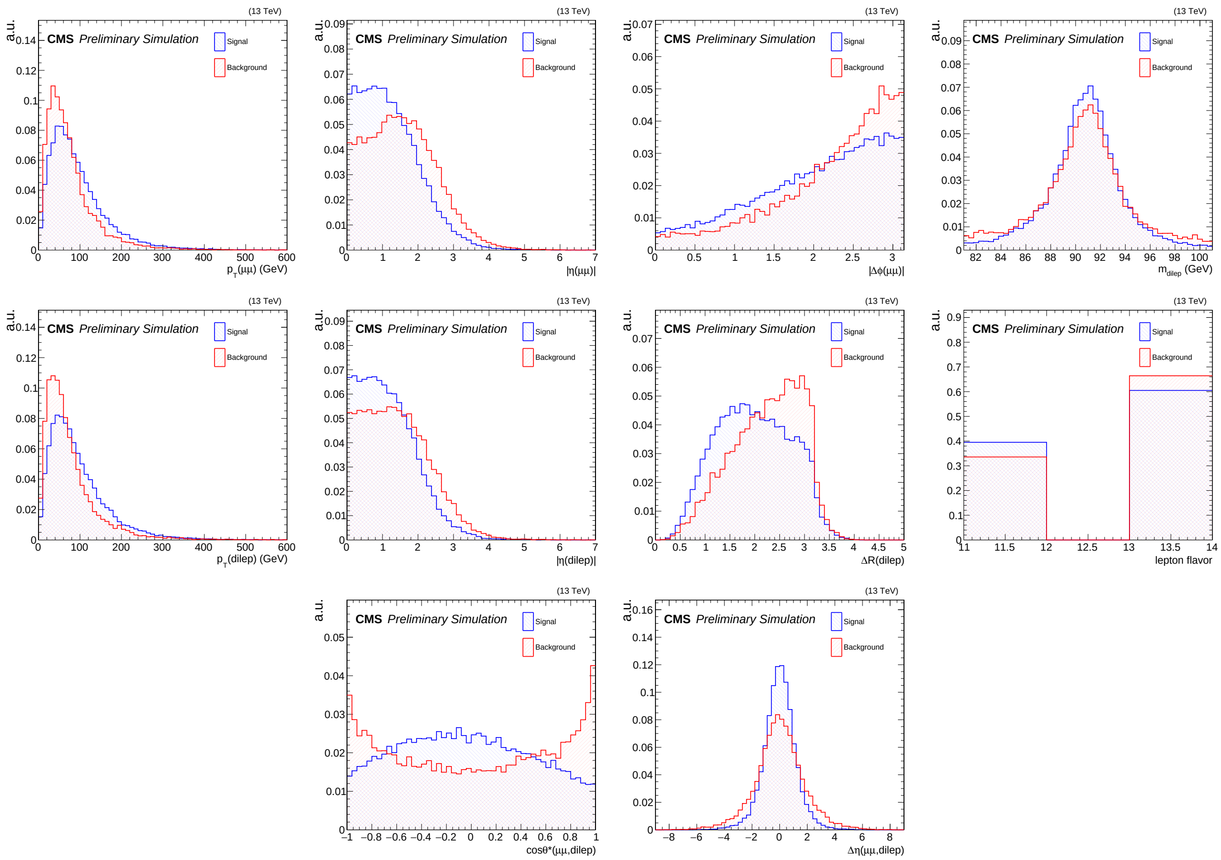

Figure 6-4. Input variables to the ZH $\rightarrow 4\ell$ BDT, with signal in blue and background in red.

6.2.3 Validation of the BDTs

As discussed in 3.2, the strategy of this analysis is to divide events into sub-categories with different S/B, and consequently maximize the overall sensitivity. The signal extraction is performed by fitting the $m_{\mu\mu}$ spectrum, therefore it is crucial that any selection cut applied to the BDT score should not sculpt the $m_{\mu\mu}$ shape. Two checks are performed for this purpose:

- The $m_{\mu\mu}$ shape of the background is compared between events in different BDT quantiles, shown as the left plots of Figures 6-5 and 6-6.
- The BDT output is compared between several signal samples with different m_{H} assumptions, shown as the right plots of Figures 6-5 and 6-6.

From these plots, no sign of correlation between BDT and $m_{\mu\mu}$ is seen. Therefore the WH and ZH BDTs can be used for categorization without introducing sculpting of the $m_{\mu\mu}$ shape.

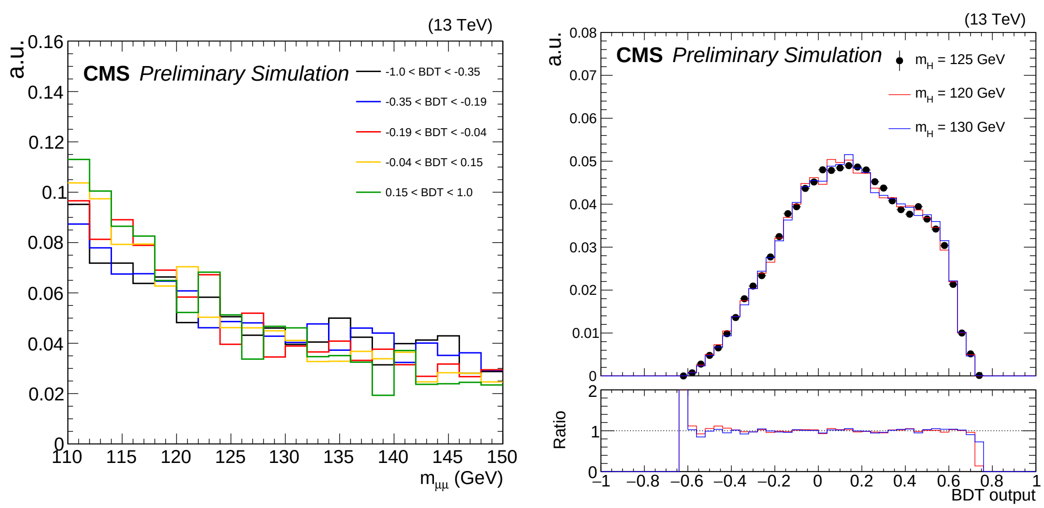

Figure 6-5. For the WH BDT, the distribution of the dimuon mass shape in the background for five different BDT quantile (left), and the distribution of the BDT output for three different signal mass assumptions (right).

Furthermore, it is also important to make sure the BDT would perform the same way on data as they do on the simulation. In order to do this, the inputs and output of the BDTs are plotted comparing between data and the simulation. Figure 6-7 shows the

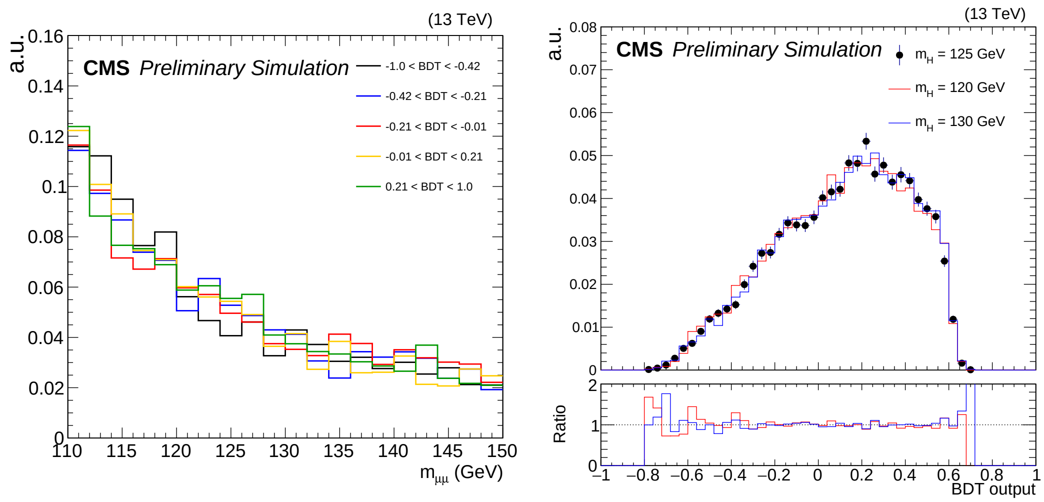

Figure 6-6. For the ZH BDT, the distribution of the dimuon mass shape in the background for five different BDT quantile (left), and the distribution of the BDT output for three different signal mass assumptions (right).

output of the WH BDT and the ZH BDT, and Figure 6-8 and 6-9 show the input variables to the WH and ZH BDTs respectively. Overall, data and simulation agree with each other within the uncertainties for the BDT outputs and most of the inputs. Some fluctuations are seen in data, especially in the ZH category, as the total number of events is small. These fluctuations are expected within the statistical uncertainty and do not indicate any systematic disagreement.

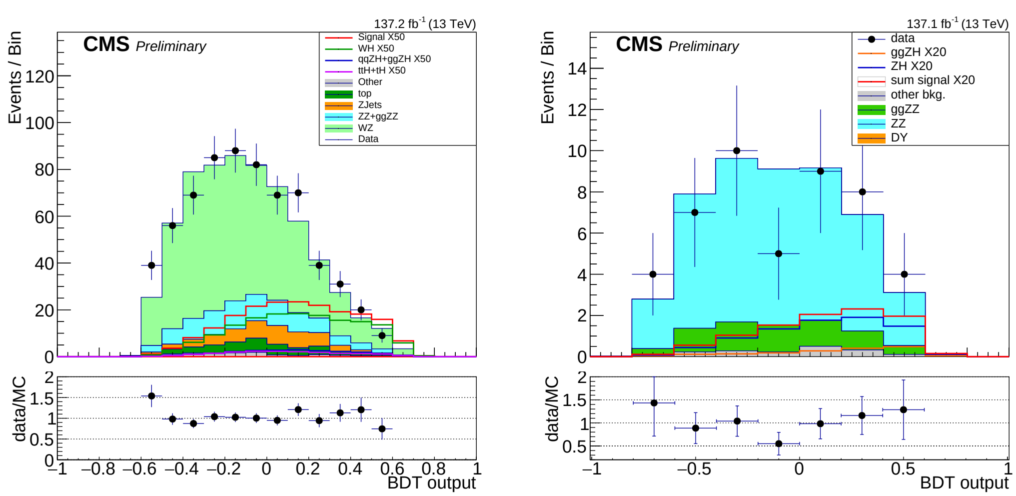

Figure 6-7. The WH BDT output (left) and the ZH BDT output (right) in full Run 2 in the signal region 110 GeV $< m_{\mu\mu} <$ 150 GeV.

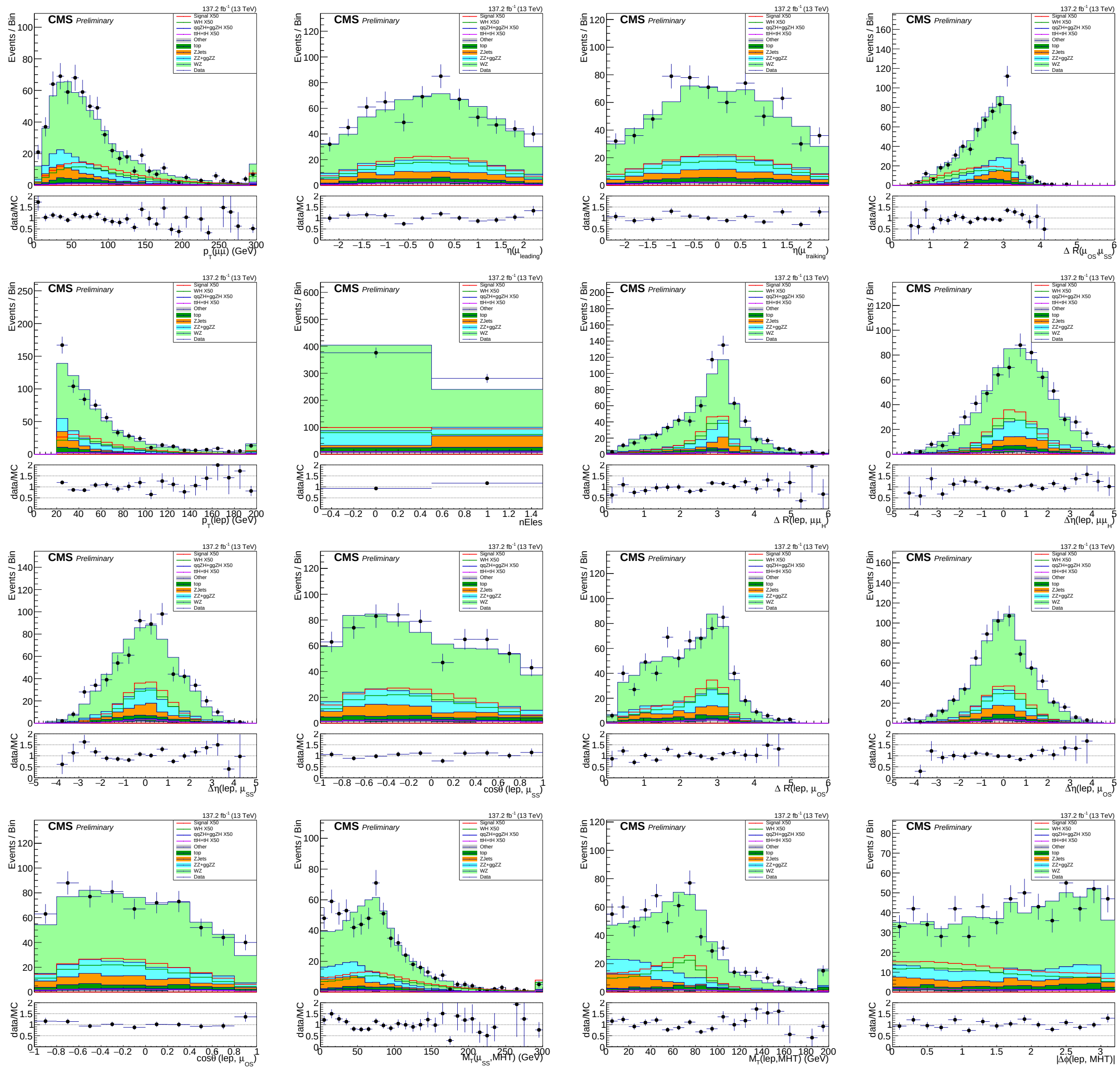

Figure 6-8. Input variables to the WH BDT in full Run 2 in the signal region 110 GeV < $m_{\mu\mu}$ < 150 GeV.

An arguable disagreement is seen in the leftmost region in one of the inputs to the WH BDT, $M_{\mathrm{T}}(\mu_{SS},\mathrm{MHT})$, shown as the second plot in the bottom row of Figure 6-8, also put separately in Figure 6-10. To understand if this disagreement would translate into a mismodeling of the WH BDT, the BDT output is plotted for both signal and background in different $M_{\mathrm{T}}(\mu_{SS},\mathrm{MHT})$ bins, shown as the right plot in Figure 6-10. In this plot, for both signal and background, the BDT profile is almost the same for events with $M_{\mathrm{T}}(\mu_{SS},\mathrm{MHT})$

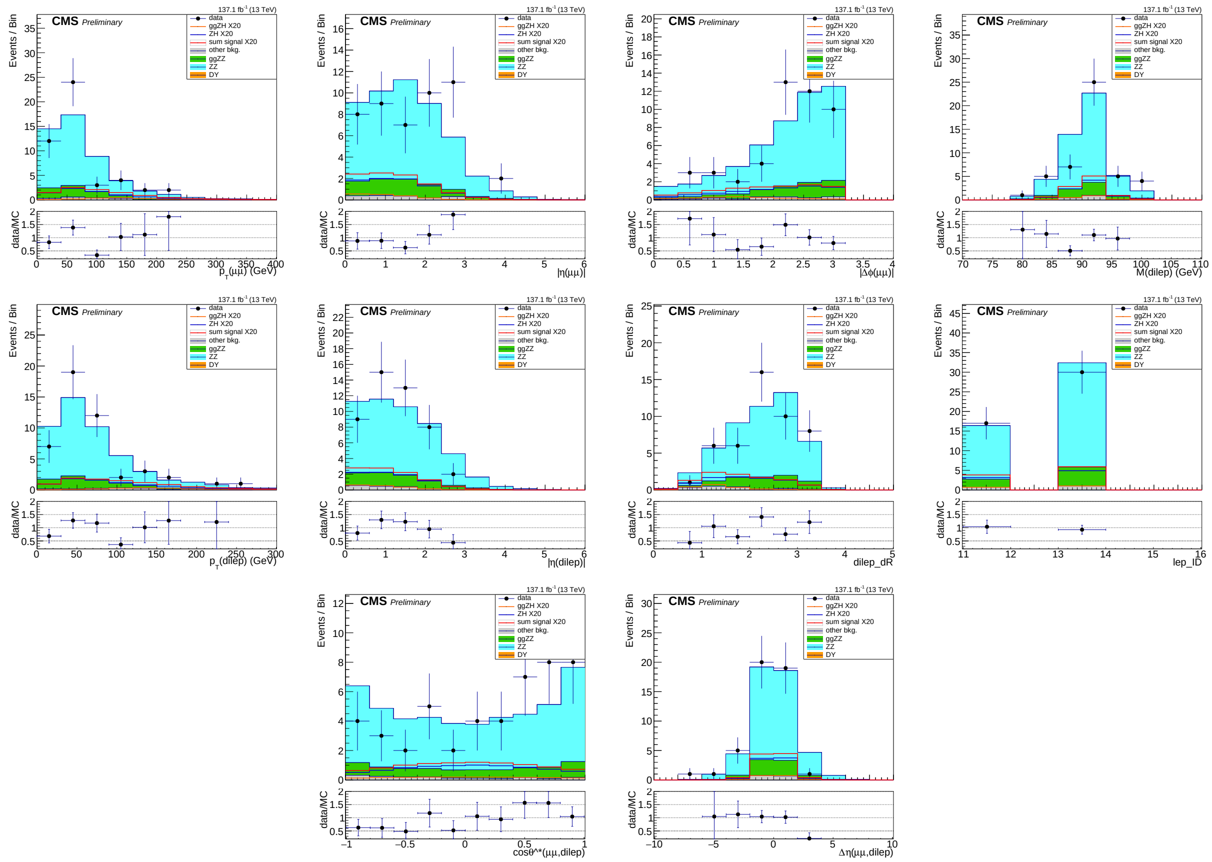

Figure 6-9. Input variables to the ZH BDT in full Run 2 in the signal region 110 GeV $< m_{\mu\mu}$ < 150 GeV.

< 40 GeV and events with $40 < M_{\mathrm{T}}(\mu_{SS},\mathrm{MHT}) < 80$ GeV, while it is different between events with $M_{\mathrm{T}}(\mu_{SS},\mathrm{MHT}) < 80$ GeV from events with $M_{\mathrm{T}}(\mu_{SS},\mathrm{MHT}) > 80$ GeV. The BDT is sensitive to whether the $M_{\mathrm{T}}(\mu_{SS},\mathrm{MHT})$ is greater or smaller than 80 GeV, but does not further distinguish events if the $M_{\mathrm{T}}(\mu_{SS},\mathrm{MHT})$ is less than 80 GeV. Once the bins below 80 GeV are merged in the left plot of Figure 6-10, there is no significant disagreement, therefore it should not cause any mismodeling of the BDT.

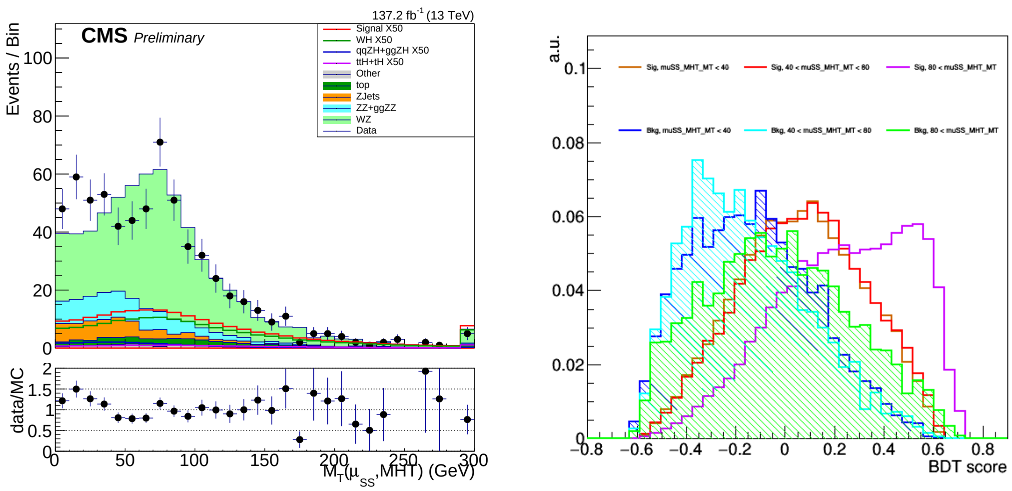

Figure 6-10. The input variable $M_{\mathrm{T}}(\mu_{SS},\mathrm{MHT})$ to the WH BDT (left), and the BDT output for signal and background in different $M_{\mathrm{T}}(\mu_{SS},\mathrm{MHT})$ bins (right). A mild disagreement is seen between the simulation and data in the low bins of $M_{\mathrm{T}}(\mu_{SS},\mathrm{MHT})$, while the BDT is not sensitive to the $M_{\mathrm{T}}(\mu_{SS},\mathrm{MHT})$ values in that region.

6.3 Event Categorization

To optimize the overall sensitivity of the VH analyses, the WH and the ZH phase-spaces are divided into several sub-categories with different S/B ratios, based on the BDT discriminants described in Section 6.2.

To achieve the maximal sensitivity with a reasonable number of sub-categories, an iterative procedure is taken. In each iteration, a cut is scanned at a step of 0.01 of the BDT value and the sum of the significance of the resulting sub-categories is calculated as the figure of merit. The figure of merit is defined as the $S/\sqrt{B}$ in each sub-category summed in quadrature, where S and B represent the expected signal and background yields within the FWHM of the signal peak in each sub-category. In addition, to ensure that there are enough events in each sub-category to perform a shape analysis, all sub-categories have to meet a minimal total event yield requirement during the BDT scanning process.

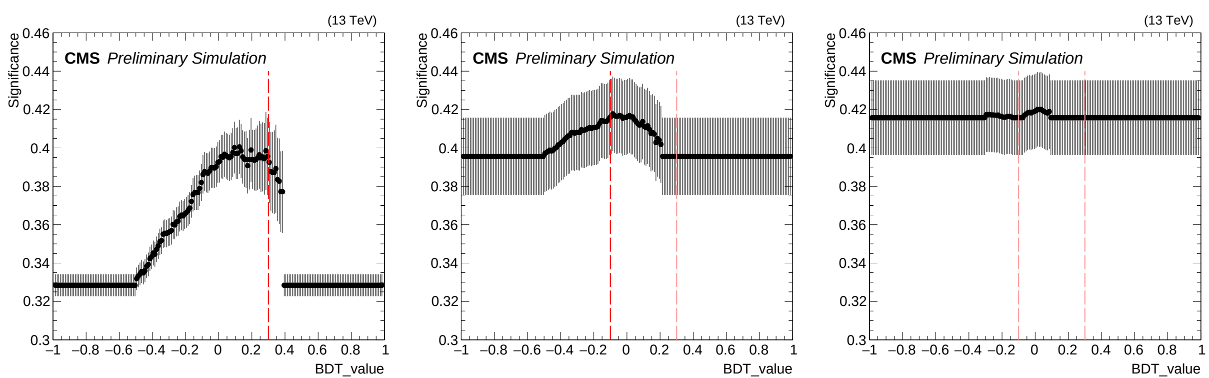

Figure 6-11. Scans for the first (left), second (middle) and a potential third (right) BDT cut in the WH channel. The first BDT cut is chosen at 0.3. The second BDT cut is chosen at -0.1. A third BDT cut is not necessary.

Figure 6-11 shows the iterations performed on the WH BDT. The minimum number of events in each category is set to be 30. In the first scan, the overall significance maximizes around $0 \sim 0.3$, and the cut is chosen at 0.3 so that there are enough events on its left side for a second cut. In the second scan, the overall significance maximizes around $-0.1 \sim 0.05$, and the position of the second cut can be any value in this range. To help decide the second cut, several third scans are performed under different assumptions of the second cut, all showing negligible changes of the overall significance (similar to the right plot in Figure 6-11). Therefore, there is no need for a third cut, and the choice for the second cut can be somewhat arbitrary. The second cut is decided at -0.1 so that there are a good number of events in the middle sub-category to ensure a stable shape analysis. As a result, two BDT boundaries are set, dividing the WH phase-space into 3 sub-categories, BDT within [-1.0, -0.1], BDT within [-0.1, 0.3] and BDT within [0.3, 1.0].

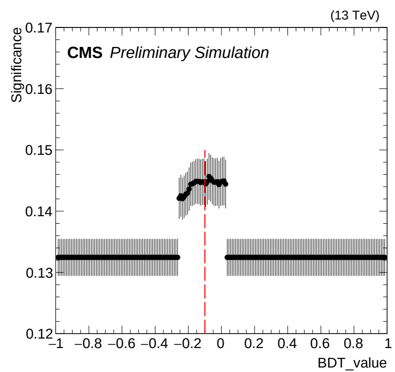

Figure 6-12. Scans for the BDT cut in the ZH channel. The BDT cut is chosen at -0.1.

Similarly, Figure 6-12 shows the scan performed on the ZH BDT. The minimum number of events in each category is set to be 16, as the total number of events in the ZH category is less than 50. In the BDT scan, the overall significance maximizes around $-0.15 \sim 0.05$. The BDT cut is chosen at -0.1, dividing the ZH events into two roughly equal halves. A second cut is not needed as the number of events is not enough for a further division. The resulting 2 ZH sub-categories are, BDT within [-1.0, -0.1], and BDT within [-0.1, 1.0].

6.4 Signal and background modeling

The extraction of signal is performed by fitting analytic functions to the $m_{\mu\mu}$ spectrum in each sub-category. Different functions are used to model the expected signal and background shapes: a sharp signal peak near 125 GeV, and a smooth falling background shape in 110 GeV $< m_{\mu\mu} <$ 150 GeV. Functions are first tested on the simulated samples to make sure the perform well in describing the shapes. The parameters of the signal function are constrained, with systematic uncertainties described in Section 6.5.1, to the best fit values to simulation as the expectation of the SM signal. The parameters of the background function are allowed to float freely, so that no prior assumption on the background is imposed, and the background prediction relies completely on data. The final evaluation of the signal strength is achieved by fitting the signal + background functions to data. where the normalizations of both the signal function and the background function are allowed to float freely. The normalization of the signal, in particular, is called the signal strength modifier and represents the signal strength relative to the SM prediction.

Function modeling of signal and background are described in Sections 6.4.1 and 6.4.2 respectively.

6.4.1 Signal modeling

In all sub-categories, signals are modeled independently by different production modes, with the contributions from three years (2016, 2017, 2018) summed together. In particular, qqZH and ggZH signals are modeled separately as there are no other signal component in the ZH category. Each of the components is modeled with a Double-sided Crystal Ball function (DCB), as described in Equation 6-1. In all DCB functions, the parameters n_L and n_R are fixed to 2.0, since they only affect the shape in tails and can take values in a large range without changing the quality of the fit by much. Other parameters are allowed to float freely.

$$\mathrm{DCB}(m_{\mu\mu}) = \begin{cases} e^{-(m_{\mu\mu}-s)^2/(2\sigma^2)} & -\alpha_\mathrm{L} < (m_{\mu\mu}-s)/\sigma < \alpha_\mathrm{R} \\ (\frac{n_\mathrm{L}}{|\alpha_\mathrm{L}|})^{n_\mathrm{L}} \times e^{-\alpha_\mathrm{L}^2/2} \times (\frac{n_\mathrm{L}}{|\alpha_\mathrm{L}|} - |\alpha_\mathrm{L}| - (m_{\mu\mu}-s)/\sigma)^{-n_\mathrm{L}} & (m_{\mu\mu}-s)/\sigma \leq -\alpha_\mathrm{L} \\ (\frac{n_\mathrm{R}}{|\alpha_\mathrm{R}|})^{n_\mathrm{R}} \times e^{-\alpha_\mathrm{R}^2/2} \times (\frac{n_\mathrm{R}}{|\alpha_\mathrm{R}|} - |\alpha_\mathrm{R}| + (m_{\mu\mu}-s)/\sigma)^{-n_\mathrm{R}} & (m_{\mu\mu}-s)/\sigma \geq \alpha_\mathrm{R} \end{cases} \tag{6-1}$$

Examples of signal modeling are shown in Figures 6-13 and 6-14. Please note that the plots shown are the signals in the inclusive WH and ZH categories. The actual models used in each sub-category are slightly different. ggH, VBF and $b\bar{b}$H have negligible contributions to the WH category and are not considered. Similarly, in the ZH category only qqZH and ggZH are considered since all other contributions are negligible.

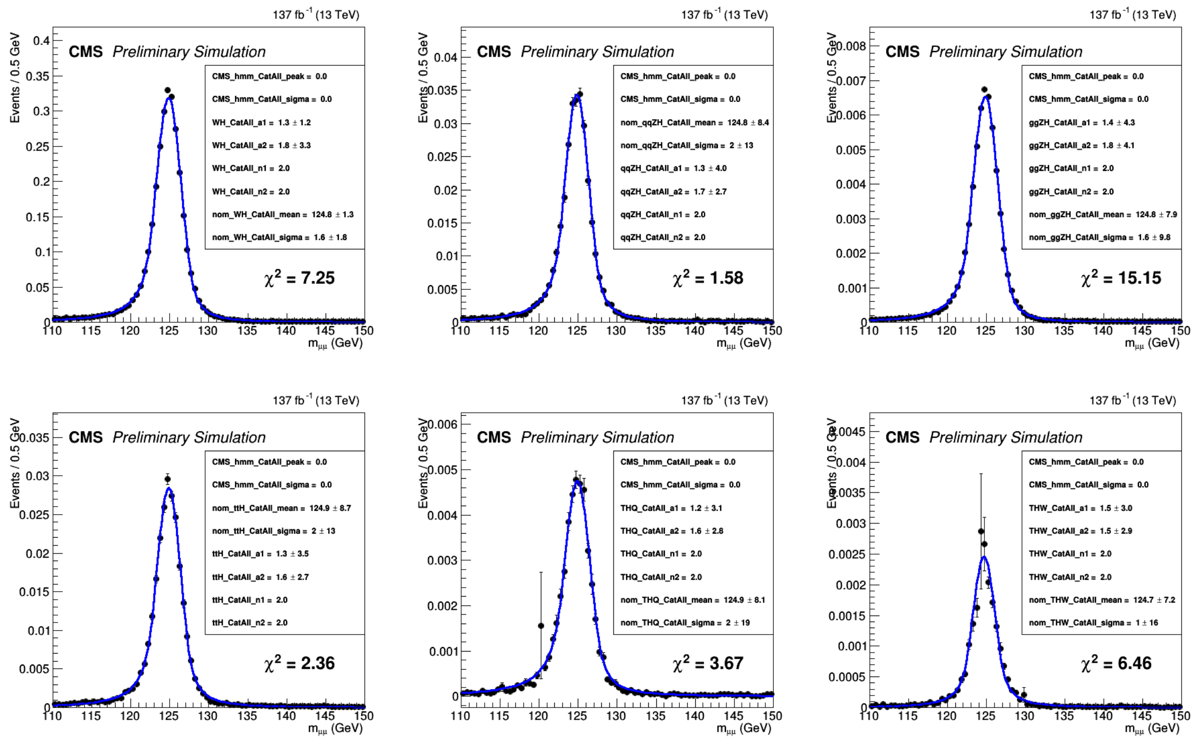

Figure 6-13. The signal modeling in the WH $\rightarrow \ell + \mu\mu$ inclusive category. Considered signal modes are WH (top left), qqZH (top middle), ggZH (top right), ttH (bottom left), THQ (bottom middle), and THW (bottom right).

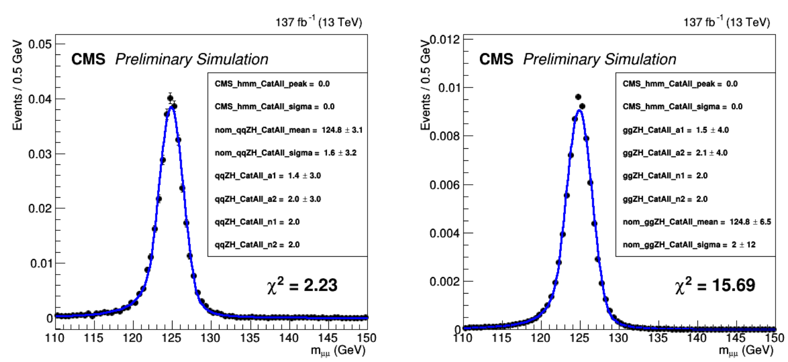

Figure 6-14. The signal modeling in the ZH $\rightarrow \ell\ell + \mu\mu$ inclusive category. Considered signals modes are qqZH (left) and ggZH (right).

6.4.2 Background modeling

As discussed in Section 6.1, the main background in WH (ZH) category is the WZ (ZZ) process, a fraction of which consists wrong pairing of the muons. The $m_{\mu\mu}$ spectrum of the correctly paired WZ (ZZ) events follows a Breit-Wigner tail of the Z boson, while the spectrum of the wrongly paired WZ (ZZ) events is rather flat. Overall the background shapes in the WH and ZH categories are smoothly falling, and Breit-Wigner like to some extent. Therefore, a group of different functional forms are considered as candidates for the background modeling. Some of them are physics-inspired, meaning that they are modified from the form of the Breit-Wigner function, the others are agnostic, which take the form of some general functional bases. The physics-inspired function candidates include the *BWZ* function (Equation 6-2), which is a Breit-Wigner core times an exponential term , the *BWZRedux* (Equation 6-3), which is a Breit-Wigner core times a exponential term with more degrees of freedom (DOFs), the *BWZGamma* (Equation 6-4), which is a linear combination of the *BWZ* function and an exponential function, and the $BWZ \times Bernstein$ (Equation 6-5), which is the *BWZ* function times a Bernstein polynomial.

$$\mathrm{BWZ}(m_{\mu\mu}) = \frac{\Gamma_Z \cdot e^{a \cdot m_{\mu\mu}}}{(m_{\mu\mu} - m_Z)^2 + (\Gamma_Z/2)^2} \tag{6-2}$$

$$\mathrm{BWZRedux}(m_{\mu\mu}) = \frac{\Gamma_Z \cdot e^{a \cdot m_{\mu\mu} + b \cdot m_{\mu\mu}^2}}{(m_{\mu\mu} - m_Z)^c + (\Gamma_Z/2)^c} \tag{6-3}$$

$$\mathrm{BWZGamma}(m_{\mu\mu}) = f \cdot \frac{\Gamma_Z \cdot e^{a \cdot m_{\mu\mu}}}{(m_{\mu\mu} - m_Z)^2 + (\Gamma_Z/2)^2} + (1-f) \cdot \frac{e^{a \cdot m_{\mu\mu}}}{m_{\mu\mu}^2} \tag{6-4}$$

$$\mathrm{BWZ} \times \mathrm{Bernstein}(m_{\mu\mu}) = \frac{\Gamma_Z \cdot e^{a \cdot m_{\mu\mu}}}{(m_{\mu\mu} - m_Z)^2 + (\Gamma_Z/2)^2} \times \mathrm{Bern}_n(m_{\mu\mu}) \tag{6-5}$$

The agnostic function candidates include the Bernstein polynomials (Equation 6-6), a series of exponential functions (Equation 6-7), and a series of power functions (Equation 6-8). In the actual fits, given the low statistics in the VH sub-categories, the sum of exponential or power functions are usually reduced to a single exponential or power function plus a constant (Equation 6-9 and 6-10).

$$\text{Bernstein}(m_{\mu\mu}) = \sum_i^n a_i \cdot \binom{n}{i} m_{\mu\mu}^i (1 - m_{\mu\mu})^{n-i} \tag{6-6}$$

$$\text{S-exponential}(m_{\mu\mu}) = \sum_i^n a_i \cdot e^{b_i \cdot m_{\mu\mu}} \tag{6-7}$$

$$\text{S-power-law}(m_{\mu\mu}) = \sum_i^n a_i \cdot m_{\mu\mu}^{b_i} \tag{6-8}$$

$$\text{Exponential+constant}(m_{\mu\mu}) = f + (1 - f) \times e^{a \cdot m_{\mu\mu}} \tag{6-9}$$

$$\text{Power-law+constant}(m_{\mu\mu}) = f + (1 - f) \times m_{\mu\mu}^a \tag{6-10}$$

In each sub-category, the function candidates are fit to the $m_{\mu\mu}$ shape in the range of $110 < m_{\mu\mu} < 150$ GeV, with events blinded in the signal region $120 < m_{\mu\mu} < 130$ GeV, so the functions are not aware of the existence of the signal. Because the limited number of events in VH sub-categories, the distribution of data is subject to large fluctuations. The $m_{\mu\mu}$ shape of data reflects both the underlying physics shape, as well as the specific features from the fluctuation of this particular dataset. It is important to make sure the modeling of background does not over-fit these specific features. On the other hand, as shown in Section 6.1 and 6.2, the simulated samples are known to provide a good modeling of data, and the $m_{\mu\mu}$ shape from the simulation can be assumed to be a good representation of the true physics shape. Therefore, the simulation can be used to study the performance of the background function candidates to learn how they would model generic expected physics shapes, and the data is treated as a particular realization of these physics distributions. The fit to simulation takes the $m_{\mu\mu}$ shape of the simulation, but assumes the statistical error in each bin as the Poisson error of the expected number of events in that bin rather than the number of simulated events in the sample. If a function candidate provides a good fit to the simulation, it is then tested on the real dataset, to make sure the fit does not break down because of the fluctuation, If the function gives consistently good fit performances on the simulation and data, it is considered as a good candidate. It is worth a remark that the fit to data does not assume any parameter information from the fit to simulation, so the simulation is only used to study the performance of the background functions, but not used to constrain the specific shapes.

All the functional forms listed above can be used with different DOFs. For the physics-inspired functions, the m_Z and Γ_Z can either be fixed at the nominal value for the Z boson or allowed to float freely, while for the agnostic functions, the order of the series can be adjusted. To find the right DOFs, each functional form is tested with different setups, and the optimal DOFs is determined following the idea of the likelihood ratio test. A standard likelihood ratio test compares the likelihood ratio between the fits with n and n+1 DOFs, usually calculated as $2(\mathrm{Log}\mathscr{L}_{n+1} - \mathrm{Log}\mathscr{L}_n)$, where the $\mathrm{Log}\mathscr{L}_n$ is the likelihood of the fit with n DOFs. This quantity should follow the χ^2_1 distribution, the chi-square distribution with one degree of freedom, whose p-value is then used to decide whether adding one more DOF in the fit leads to a significantly better fit quality.

In the practice of background fitting in the VH sub-categories, which all have low expected number of events, it turns out in most cases two DOFs are enough, one for overall normalization and one for shape variation. In some sub-categories with very low statistics, even functions without any shape DOF give good performances, namely, a function with all its shape parameters fixed at the best fit values to the simulation can be a good fit to data. These fixed shapes are included as some candidates along side with their freely floating versions. On the other hand, when the shape parameters are allowed to float, agnostic functions with low DOFs do not always fit well as they lack enough flexibility. For example, an order-1 Bernstein polynomial (2 shape DOFs) is just a straight line and is obviously not the true $m_{\mu\mu}$ shape, and the fits with a single exponential or power function are not stable and sometimes do not converge. To mitigate these behaviors, a BWZ $\times$ order-1 Bernstein (2 shape DOF in total), in which the BWZ part is fixed with the nominal Z boson shape, is used instead of the plain Bernstein, and a single exponential (power) function plus a free constant (2 shape DOF in total) is used instead of the plain exponential (power) function. Overall, the good function candidates include fixed forms (1 normalization DOF + 0 shape DOF) and floating forms (1 normalization DOF + 1 $\sim$2 shape DOFs).

The final choices of the background function in each sub-category is decided based on the bias it may have against other possibilities, described in detail in Section 6.5.3. If several functions pass the bias requirement, the function with the fewest DOF is chosen, as it leads to the highest significance in statistical analysis.

6.5 Systematic uncertainties

A crucial task in the statistical analysis is to evaluate all the systematic uncertainties that affect the signal and background estimation. In this analysis, both the signal and background are described by analytic functions, and the statistical analysis is performed based on the fits of them. All sources of systematic uncertainties are therefore translated into the variations of the parameters of signal and background functions.

Several sources of signal systematic uncertainties are considered, divided into two types, the *shape* and the *rate* uncertainties. The *shape* uncertainties, described in Section 6.5.1, account for the factors affecting the expected shape of the signal peak, while the *rate* uncertainties, described in Section 6.5.2, are those affecting the expected signal yield.

A different approach is taken to evaluate the systematic uncertainty in background. The background estimation always takes the best fit to data and does not rely on simulation, therefore none of the theoretical or experimental uncertainties considered for the signal needs to be considered for the background. However, by fitting the background shape with an analytical function, a potential bias could be introduced between the chosen background model and the underlying real distribution. A bias between the background estimation and the true background appearing at the position of the signal is essentially a spurious signal. This bias has to be small so that it does not impact the validity of the signal strength evaluation. The study to evaluate this potential bias is described in details in Section 6.5.3.

6.5.1 Signal shape uncertainties

For all Higgs boson production modes, the expected $m_{\mu\mu}$ signal shape is primarily affected by the uncertainties in muon energy scale and resolution, in other words the mean and sigma values in the DCB fits of the signal peak. As described in Chapter 5, the *Rochester correction* is implemented to correct for differences in both scale and resolution between data and simulated events, while the *FSR recovery* and *GeoFit correction* are not expected to introduce new differences between data and simulation. In the meantime, Section 5.4 shows that the simulation of the DY peak agrees with the data up to a per-mille level in scale and a percent level in resolution. The shape uncertainties can be estimated accordingly.

The muon energy scale shape uncertainty is estimated to be 0.1% of the mean value of the $m_{\mu\mu}$ peak, and the muon energy resolution uncertainty is conservatively estimated to be 10% of the resolution of the $m_{\mu\mu}$ peak. The effect of the scale uncertainty is an overall shift of the $m_{\mu\mu}$ peak to higher or lower mass value, while the effect of the resolution uncertainty is a stretching or squeezing of the width of the $m_{\mu\mu}$ peak. Both uncertainties are modeled as a Gaussian constrained nuisance parameter which is correlated across different production modes but uncorrelated between different sub-categories.

6.5.2 Signal rate uncertainties

The rate uncertainties are the ones that affect the signal yield in each sub-category, and may come from various sources. Some of them affect the overall prediction of the signal and act as a factor on the overall normalization of the signal. The normalization uncertainties include the theoretical uncertainties on the cross sections of signal productions, and theoretical uncertainties on the $\mathscr{B}(\mathrm{H} \to \mu\mu)$, as well as the uncertainties on the CMS luminosity measurement. Other uncertainties tweak the event kinematics and affect the acceptance of signals in each sub-category. The acceptance uncertainties include the uncertainties on all the event weights in the simulation, the uncertainties from all the efficiency scale factors applied in the analysis, and the uncertainties from all the physics object calibrations and corrections.

The impacts from theoretical uncertainties are shown in Table 6-5. The uncertainty on the $\mathscr{B}(\mathrm{H} \to \mu\mu)$ is $\pm 1.23\%$, independent from the production modes. The luminosity uncertainty for each year is set following the official recommendation of CMS, which is 2.5%, 2.3% and 2.5% for 2016, 2017 and 2018 respectively. Since the signals are modeled summing all years, the luminosity uncertainty in each year reflected in the overall signal yield is 0.7%, 0.7% and 1.1%, for 2016, 2017, and 2018.

Table 6-5. Normalization uncertainties on the Higgs boson production cross sections for various modes at $\sqrt{s} = 13\mathrm{TeV}$.

Process	Perturbative Order	+QCD scale unc. (%)	-QCD scale unc. (%)	+(PDF+α_s) unc. (%)	-(PDF+α_s) unc. (%)
WH	NNLO (QCD)	+0.5	-0.7	+1.9	-1.9
	NLO (EWK)				
qqZH	NNLO (QCD)	+0.5	-0.6	+1.9	-1.9
	NLO (EWK)				
ggZH	NLO (QCD)	+25.1	-18.9	+2.4	-2.4
$\mathrm{t\bar{t}H}$	NLO (QCD)	+5.8	-9.2	+3.6	-3.6
	NLO (EWK)				
tHq	NLO (QCD)	+6.5	-14.9	+3.7	-3.7
tHW	NLO (QCD)	+4.9	-6.7	+6.3	-6.3

The impacts from the pileup re-weight and ECAL L1 trigger prefiring re-weight are shown in Table 6-6. The acceptance impacts from the muon energy scale corrections are shown in Table 6-7. The impacts from the muon and electron ID scale factors (the lepMVA scale factor) are shown in Table 6-8. The impacts from the B-jet ID scale factors (for the B-jet vetoing) are shown in Table 6-9. The impacts from the jet energy calibrations are shown in Table 6-10.

Table 6-6. Uncertainties on different signal components in the WH and ZH channels related to pileup re-weight and L1 prefiring re-weight. Numbers before/after are the affects from shifting the uncertainty source up/down. Uncertainties smaller than 0.1% are neglected.

Uncertainty	Category	WH	qqZH	ggZH	ttH	THQ	THW
pileup 2016 (%)	WH cat0	+0.8/-0.7	+0.8/-0.7	+0.6/-0.5	+0.9/-0.7	+1.0/-0.9	+0.4/-0.4
	WH cat1	+0.8/-0.7	+0.6/-0.5	+0.6/-0.5	+0.6/-0.5	+1.0/-0.9	+0.7/-0.6
	WH cat2	+0.6/-0.5	+0.4/-0.3	+0.6/-0.4	+0.7/-0.6	+0.2/-0.3	+0.5/-0.4
	ZH cat0	-	+0.7/-0.7	+0.8/-0.7	-	-	-
	ZH cat1	-	+0.8/-0.7	+0.7/-0.6	-	-	-
pileup 2017 (%)	WH cat0	+0.6/-0.5	+0.2/-0.2	+0.3/-0.3	+0.3/-0.2	+0.3/-0.5	+0.6/-0.7
	WH cat1	+0.4/-0.4	+0.4/-0.4	+0.3/-0.3	+0.3/-0.3	+0.4/-0.5	+0.3/-0.4
	WH cat2	+0.5/-0.5	+0.5/-0.3	+0.3/-0.3	+0.6/-0.6	+0.5/-0.5	+0.4/-0.2
	ZH cat0	-	+0.4/-0.4	+0.4/-0.5	-	-	-
	ZH cat1	-	+0.3/-0.4	+0.4/-0.4	-	-	-
pileup 2018 (%)	WH cat0	+0.6/-0.6	+0.4/-0.4	+0.5/-0.5	+0.6/-0.6	+0.5/-0.5	+0.5/-0.5
	WH cat1	+0.5/-0.5	+0.3/-0.3	+0.4/-0.4	+0.5/-0.5	+0.4/-0.4	+0.8/-0.8
	WH cat2	+0.4/-0.4	+0.2/-0.3	+0.4/-0.4	+0.4/-0.3	+0.5/-0.5	+0.8/-0.8
	ZH cat0	-	+0.6/-0.6	+0.5/-0.5	-	-	-
	ZH cat1	-	+0.6/-0.6	+0.5/-0.5	-	-	-
prefire 2016 (%)	WH cat0	+0.1/-0.1	+0.1/-0.1	+0.2/-0.2	+0.2/-0.2	+0.2/-0.2	+0.2/-0.2
	WH cat1	+0.1/-0.1	+0.1/-0.1	+0.2/-0.2	+0.2/-0.2	+0.2/-0.2	+0.1/-0.1
	WH cat2	-	+0.1/-0.1	+0.1/-0.1	+0.1/-0.1	+0.2/-0.2	+0.1/-0.1
	ZH cat0	-	+0.1/-0.1	+0.1/-0.1	-	-	-
	ZH cat1	-	+0.1/-0.1	+0.1/-0.1	-	-	-
prefire 2017 (%)	WH cat0	+0.2/-0.2	+0.3/-0.3	+0.3/-0.3	+0.4/-0.4	+0.3/-0.3	+0.2/-0.3
	WH cat1	+0.1/-0.1	+0.3/-0.3	+0.3/-0.3	+0.3/-0.3	+0.3/-0.4	+0.2/-0.2
	WH cat2	+0.1/-0.1	+0.2/-0.2	+0.2/-0.2	+0.2/-0.2	+0.2/-0.2	+0.1/-0.1
	ZH cat0	-	+0.2/-0.2	+0.3/-0.3	-	-	-
	ZH cat1	-	+0.1/-0.1	+0.2/-0.2	-	-	-

Table 6-7. Uncertainties on different signal components in the WH and ZH channels related to the muon energy scale. Numbers before/after are the affects from shifting the uncertainty source up/down. Uncertainties smaller than 0.1% are neglected.

Uncertainty (%)	WH	qqZH	ggZH	ttH	THQ	THW
WH cat0	-	+0.0/+0.1	-	-0.1/+0.3	+0.0/-0.1	+0.0/+0.3
WH cat1	-	-0.1/-0.0	+0.1/-0.1	+0.1/-0.0	-0.1/+0.2	-0.1/-0.2
WH cat2	+0.0/+0.1	-0.2/-0.0	-0.2/+0.1	-0.2/-0.0	+0.0/+0.4	+0.1/-0.0
ZH cat0	-	+0.0/+0.1	+0.0/+0.1	-	-	-
ZH cat1	-	-0.1/-0	-	-	-	-

Table 6-8. Uncertainties on different signal components in the WH and ZH channels related to lepMVA scale factor. The lepMVA scale factor is the only scale factor applied to correct for the lepton efficiency modeling. The ID scale factor and Isolation scale factor are covered by the lepMVA scale factors. Numbers before/after are the affects from shifting the uncertainty source up/down. Uncertainties smaller than 0.1% are neglected.

Uncertainty	Category	WH	qqZH	ggZH	ttH	THQ	THW
muon SF	WH cat0	-1.8/+1.8	-1.7/+1.8	-2.3/+2.3	-2.3/+2.3	-2.1/+2.1	-2.5/+2.5
(%)	WH cat1	-1.7/+1.8	-1.7/+1.7	-2.4/+2.4	-2.0/+2.0	-1.9/+2.0	-2.3/+2.3
	WH cat2	-2.3/+2.3	-1.9/+2.0	-2.5/+2.5	-2.5/+2.5	-2.3/+2.4	-2.8/+2.9
	ZH cat0	-	-1.9/+1.9	-2.5/+2.6	-	-	-
	ZH cat1	-	-2.5/+2.6	-3.3/+3.4	-	-	-
electron SF	WH cat0	-0.3/+0.3	-0.4/+0.4	-0.4/+0.4	-0.3/+0.3	-0.4/+0.4	-0.2/+0.2
(%)	WH cat1	-0.5/+0.5	-0.6/+0.6	-0.5/+0.5	-0.5/+0.5	-0.6/+0.6	-0.5/+0.5
	WH cat2	-0.5/+0.5	-0.6/+0.6	-0.6/+0.6	-0.5/+0.5	-0.6/+0.6	-0.5/+0.5
	ZH cat0	-	-0.6/+0.6	-0.6/+0.6	-	-	-
	ZH cat1	-	-0.8/+0.8	-0.6/+0.6	-	-	-

Table 6-9. Uncertainties on different signal components in the WH and ZH channels related to B-jet vetoing. Numbers before/after are the affects from shifting the uncertainty source up/down. Uncertainties smaller than 0.1% are neglected.

Uncertainty (%)	WH	qqZH	ggZH	ttH	THQ	THW
WH cat0	+0.1/-0.1	+0.1/-0.1	-0.8/+0.8	+5.5/-5.3	-0.9/+0.9	-1.4/+1.4
WH cat1	+0.1/-0.1	+0.1/-0.1	-0.9/+0.9	+5.7/-5.5	-0.8/+0.8	-1.3/+1.3
WH cat2	+0.1/-0.1	+0.0/-0.1	-1.0/+1.0	+5.3/-5.1	-0.9/+0.9	-1.4/+1.4
ZH cat0	-	+0.1/-0.1	-0.6/+0.6	-	-	-
ZH cat1	-	+0.2/-0.2	-0.5/+0.5	-	-	-

Table 6-10. Uncertainties on different signal components in the WH Cat0 related to jet energy calibration. JEC uncertainties are in general small for the main signals in the WH and ZH channels. WH Cat0 is shown as an example. Numbers in other categories are similar. Numbers before/after are the affects from shifting the uncertainty source up/down. Uncertainties smaller than 0.1% are neglected.

Uncertainty (%)	WH	qqZH	ggZH	ttH	THQ	THW
flavorQCD	+0.1/-0.0	-0.4/-0.0	+0.1/-0.0	+0.6/-0.9	+0.2/-0.5	+1.5/-0.8
relativeBal	+0.1/-0.0	-0.2/-0.0	+0.1/-0.0	+0.7/-0.5	+0.0/-0.2	+0.7/-0.5
absolute	-	+0.0/+0.1	-	-	+0.0/+0.1	+0.1/+0.4
BBEC1	+0.1/-0.0	-0.4/-0.0	+0.1/-0.1	+1.5/-1.1	+0.2/-0.7	+1.2/-0.7
EC2	-	-	-	-0.1/-0.0	-0.1/-0.3	+0.2/+0.1
HF	-0.1/+0.1	-0.2/-0.0	+0.1/+0.1	+0.5/-0.6	+0.0/-0.5	+0.5/+0.3
relativeSample_2016	-	-0.1/-0.0	-	+0.1/-0.3	-	+0.1/-0.3
absolute_2016	-	+0.0/-0.1	-	+0.1/-0.1	+0.0/+0.1	-
BBEC1_2016	-	+0.0/-0.1	-	+0.0/-0.1	+0.0/+0.1	+0.1/-0.0
EC2_2016	-	-	-	-	+0.0/+0.1	+0.1/-0.0
HF_2016	-	-	-	-	-	+0.1/-0.0
relativeSample_2017	-	-0.1/+0.2	+0.1/-0.0	+0.1/-0.2	-0.2/+0.1	+0.3/+0.3
absolute_2017	-	-0.1/+0.2	-	+0.2/-0.1	-	+0.3/+0.2
BBEC1_2017	-	-0.1/+0.1	-	+0.2/+0.0	-0.1/+0.1	+0.2/+0.0
EC2_2017	-	+0.1/-0.0	-	-	+0.1/+0.3	+0.1/+0.3
HF_2017	-	-	-	-	-0.1/-0.2	-
relativeSample_2018	-0.1/+0.1	+0.1/+0.2	+0.1/-0.0	+0.4/-0.5	+0.1/-0.4	+0.7/-0.7
absolute_2018	+0.0/+0.1	-0.2/-0.0	-	+0.0/-0.1	+0.2/-0.4	+0.3/-0.6
BBEC1_2018	+0.0/+0.1	-0.2/-0.0	-	+0.0/-0.1	-	+0.1/-0.1
EC2_2018	+0.0/+0.1	-0.1/+0.1	-	+0.0/+0.1	+0.0/+0.1	+0.0/+0.1
HF_2018	-	+0.0/-0.1	-	+0.0/+0.1	+0.0/-0.1	-

6.5.3 Background systematic bias

As described in Section 6.4.2, the background modeling follows a data-driven approach, and is not affected by any systematic uncertainty in the simulation. Instead of evaluating the impacts of uncertainties as done for the signal modeling, the main task for background is to make sure it is robust against spurious signals.

A spurious signal is produced by the bias between the analytic background function and the true background shape at the position of the expected signal. For an analysis with finite statistics, there is a statistical uncertainty on the signal strength, σ_{stat}, resulted from the from the statistical fluctuation of background events. The best fit signal strength μ_{fit} under the null hypothesis, which is the hypothesis without the existence of a true signal, should follow $\mathcal{N}(0, \sigma_{stat})$, the normal distribution with a mean of 0 and a standard deviation of σ_{stat}. The 1σ or 2σ range of this distribution gives the 68.3% or 95.4% confidence intervals for the exclusion of this null hypothesis. If there is a systematic spurious signal $\hat{\mu}_{SS}$, namely a bias, the probability distribution for the μ_{fit} becomes $\mathcal{N}(\hat{\mu}_{SS}, \sigma_{stat})$, and the coverage of the $1\sigma_{stat}$ range becomes equation 6-11, which is not 68.3%.

$$\int_{-\sigma_{stat}}^{\sigma_{stat}} \mathcal{N}(\hat{\mu}_{SS}, \sigma_{stat}) = \frac{1}{2}\,[erf(\frac{\sigma_{stat}+\hat{\mu}_{SS}}{\sqrt{2}\,\sigma_{stat}}) + erf(\frac{\sigma_{stat}-\hat{\mu}_{SS}}{\sqrt{2}\,\sigma_{stat}})] \tag{6-11}$$

The left plot of Figure 6-15 illustrates this difference in coverage. The middle plot of Figure 6-15 shows how the coverage changes as the bias gets larger. As a result, to achieve the 68.3% confidence level, the signal uncertainty from the fit, σ_{fit}, needs to satisfy equation 6-12 and becomes larger than the σ_{stat}.

$$\frac{1}{2}\,[erf(\frac{\sigma_{fit}+\hat{\mu}_{SS}}{\sqrt{2}\,\sigma_{stat}}) + erf(\frac{\sigma_{fit}-\hat{\mu}_{SS}}{\sqrt{2}\,\sigma_{stat}})] = 68.3\% \tag{6-12}$$

In this way, the bias in the background modeling, even if it is not strictly an uncertainty, adds to the overall uncertainty of the signal strength measurement. The relationship between σ_{fit} and $\hat{\mu}_{SS}$ is shown in the right plot of Figure 6-15. As a convention in the $\mathrm{H} \to \mu\mu$ analysis, biases below 20% of the statistical uncertainty of the signal are considered acceptable, which corresponds to less than 2% inflation of the signal uncertainty.

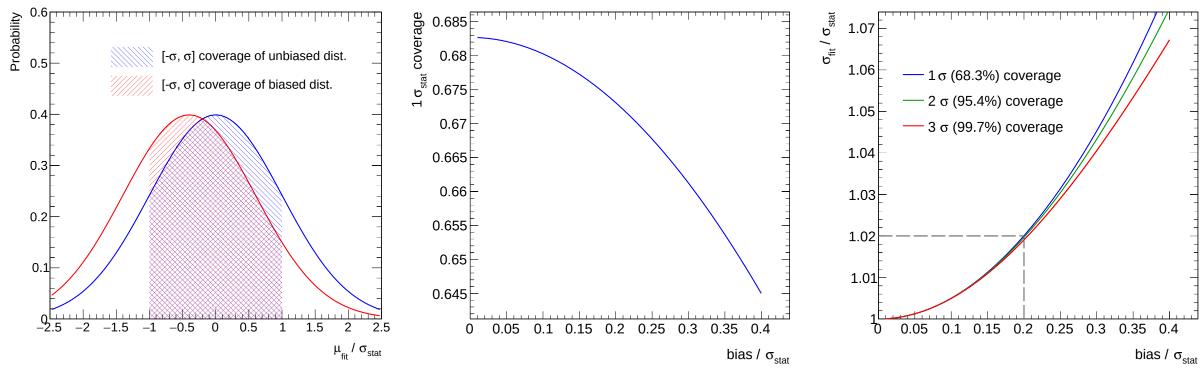

Figure 6-15. Schemes on how the bias affects the uncertainty on the signal strength measurement. The left plot is an illustration of the $[-\sigma, \sigma]$ coverage of the biased signal strength measurement. The middle plot shows this coverage becomes less as the bias gets larger. The right plot shows how the bias impacts the best fit signal strength uncertainty σ_{fit}. The gray dash lines in the right plot indicates the conventional acceptable range of the bias in this analysis.

In this analysis, the bias is evaluated between different function candidates via groups of toy studies. The true background shape is of course unknown, but is believed to be covered by the flexibility of the collective set of functional forms. Procedures for the bias evaluation are as follows:

1. Toy generation
   - One function candidate $f(m_{\mu\mu})$ is fit to the background shape of the simulation to find the best fit parameters.
   - The best fit shape of $f(m_{\mu\mu})$ is used as the Probability Density Function (PDF) to generate toy datasets. In the each toy, the number of events in each bin is taken sampling the Poisson distribution of the expected number of events given by $f(m_{\mu\mu})$.
   - For each selected function $f(m_{\mu\mu})$, 3000 toys are generated.

2. Signal injection
   - For each background toy, an artificial signal is also generated following the Poisson distribution of a given signal strength $\hat{\mu}_{inj}$. In this set of study, two sets of artificial signal strength are tested, which are zero or the expected SM signal strength.

- The artificial signal toys are added to the background toys, which completes the signal + background toys.

3. Signal extraction

   - For each signal + background toy of function $f(m_{\mu\mu})$, the shape analysis is performed using another function $g(m_{\mu\mu})$. In these toy analyses, systematic uncertainties on the signal modeling are not included, as they are unrelated to the bias estimation.
   - From these fits, the best fit signal strength μ_{fit} and its standard deviation σ_{fit} are extracted.

4. Bias evaluation

   - The spurious signal between function $f(m_{\mu\mu})$ and $g(m_{\mu\mu})$ in each toy is defined as:
   $$\mu_{SS}(f,g) = \frac{\mu_{fit} - \hat{\mu}_{inj}}{\sigma_{fit}} \tag{6-13}$$
   - The distribution (of 3000 toys) of this spurious signal is fit with a gaussian function. As stated above, this spurious signal should follow the Gaussian distribution $\mathcal{N}(\hat{b}, 1)$, where $\hat{b} = \hat{\mu}_{SS}/\sigma_{stat}$. The mean value from the Gaussian fit is the bias between function $f(m_{\mu\mu})$ and $g(m_{\mu\mu})$.

Such bias is evaluated in each sub-category between each combination of $f(m_{\mu\mu})$ and $g(m_{\mu\mu})$, and the results are summarized in Figure 6-16 and 6-17. Most of the functions have good bias response against other functions can be used for the analysis. In the final analysis, the BWZGamma function (2 shape DOF) is chosen as the background model in the WH [-1.0, -0.1] category, and the BWZ function (1 shape DOF) is chosen in all other categories.

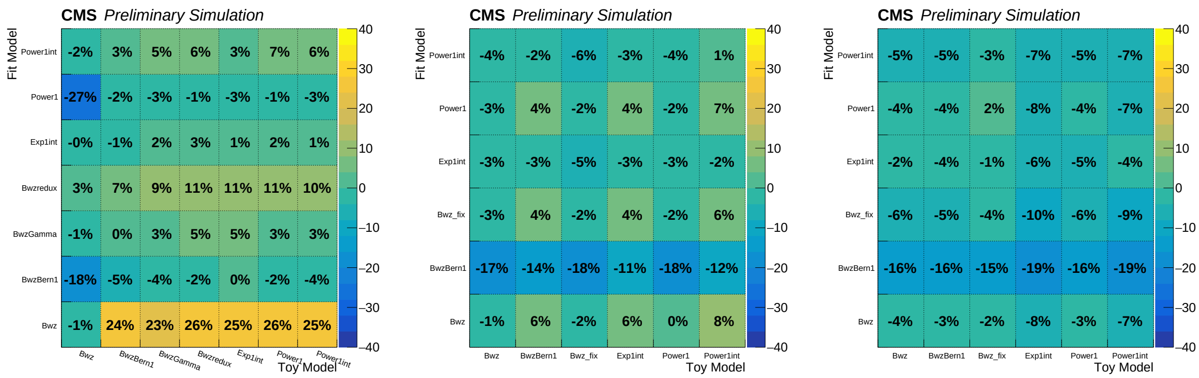

Figure 6-16. Bias in different BDT-based WH sub-categories. The sub-categories are: Cat0 BDT [-1.0, -0.1] (left), Cat1 BDT [-0.1, 0.3] (middle), Cat2 BDT [0.3, 1.0] (right). In the tables, the Power stands for a single "Power" function and the "PowerInt" stands for a single power function plus a constant.

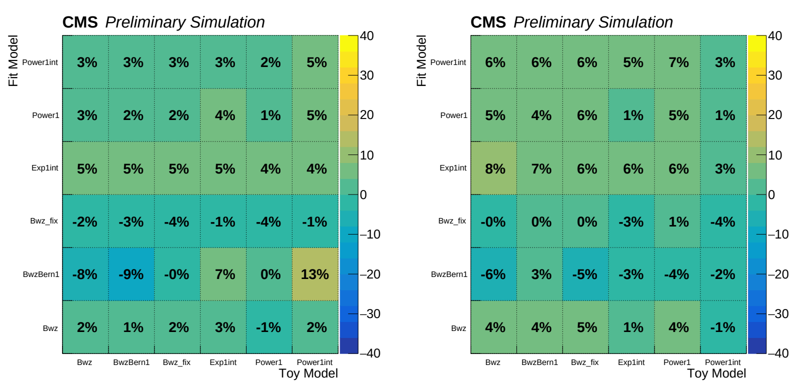

Figure 6-17. Bias in different BDT-based ZH sub-categories. The sub-categories are: Cat0 BDT [-1.0, -0.1] (left), Cat1 BDT [-0.1, 1.0] (right). In the tables, the "Power" stands for a single power function and the "PowerInt" stands for a single power function plus a constant.

6.6 Results of the VH analysis

The final results are extracted by performing a binned maximum-likelihood fit in each VH sub-category. The fit is performed on the observed $m_{\mu\mu}$ distribution in the range of $110 < m_{\mu\mu} < 150$ GeV. All the different signal modes in different sub-categories shares a common signal strength modifier μ. Figure 6-18 and 6-19 show the post-fit results of the signal-plus-background fits in the WH and ZH sub-categories.

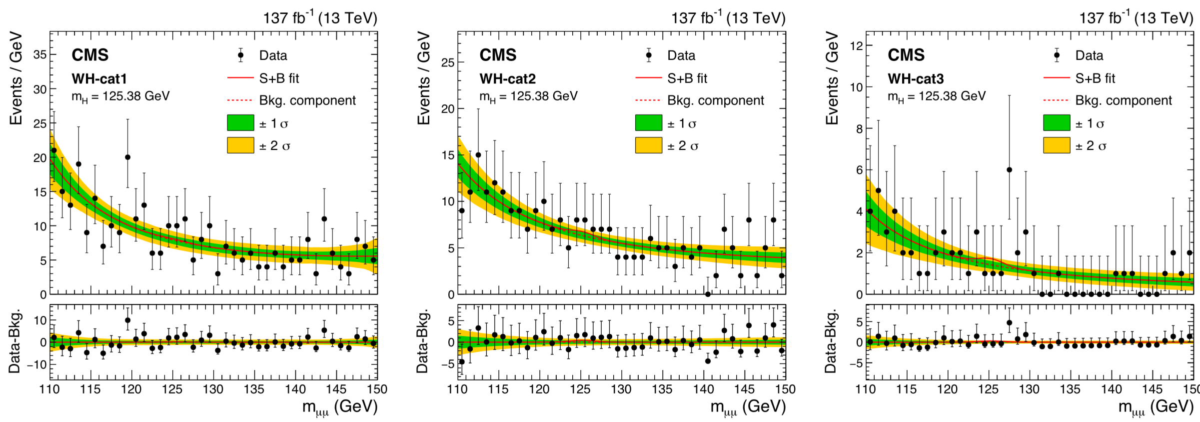

Figure 6-18. Post-fit $m_{\mu\mu}$ distribution of the WH sub-categories. The sub-categories are: Cat0 BDT [-1.0, -0.1] (left), Cat1 BDT [-0.1, 0.3] (middle), Cat2 BDT [0.3, 1.0] (right). The upper panel in the plots shows the distribution of observed data and the shape of the signal-plus-background fit. The lower panel in the plots shows the residual distribution after subtracting the background component in the fits. The green and yellow bands show the one and two standard deviation of the background component uncertainty. Plots taken from Ref. [15].

As described in Section 3, the VH analysis is combined with other categories (ggH, VBF, and $t\bar{t}$H) to make the inclusive $H \to \mu\mu$ analysis. More studies in the statistical analysis are covered in more details in Chapter 7. The expected and observed limits and significance for the VH sub-categories are summarized in Table 6-11.

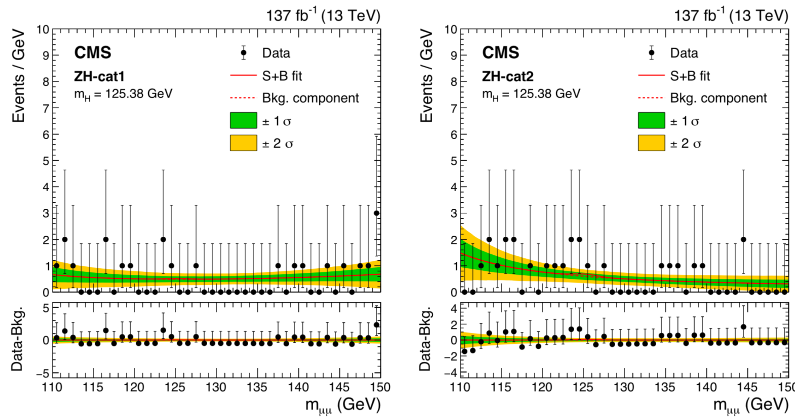

Figure 6-19. Post-fit $m_{\mu\mu}$ distribution of the ZH sub-categories. The sub-categories are: Cat0 BDT [-1.0, -0.1] (left), Cat1 BDT [-0.1, 1.0] (right). The upper panel in the plots shows the distribution of observed data and the shape of the signal-plus-background fit. The lower panel in the plots shows the residual distribution after subtracting the background component in the fits. The green and yellow bands show the one and two standard deviation of the background component uncertainty. Plots taken from Ref. [15].

Table 6-11. Summary of the expect and observed limits and significance in each individual sub-category and the combination.

Category	Expected UL	Observed UL	Expected Signif.	Observed Signif.
WH $\rightarrow 3\ell$ Cat0	27	37.4	0.08	0.89
WH $\rightarrow 3\ell$ Cat1	9.8	12.8	0.22	0.79
WH $\rightarrow 3\ell$ Cat2	7.3	10.4	0.33	0.64
ZH $\rightarrow 4\ell$ Cat0	58	68.2	0.05	0.65
ZH $\rightarrow 4\ell$ Cat1	19	34.0	0.14	1.81
WH combine	5.5	8.9	0.40	1.15
ZH combine	17	31.7	0.15	1.92
WH and ZH combine	5.1	10.2	0.43	1.86

The analysis in the VH category is combined with those in the ggH, VBF, and $t\bar{t}$H categories. Figure 7-1 summarizes the expected signal composition in all sub-categories of the $\mathrm{H} \to \mu\mu$ analysis. Figure 7-2 summarizes the expected $S/(S+B)$ and $S/\sqrt{B}$ in all sub-categories, in which the signal and background yields are calculated by integrating the expectations within the FWHM range of the signal peak for the ggH, VH, and $t\bar{t}$H sub-categories, while for the VBF category the considered mass range is $115\mathrm{GeV} < m_{\mu\mu} < 135\mathrm{GeV}$. For both figures, the mass of the Higgs boson is expected at $m_{\mathrm{H}} = 125.38$ GeV [19], which is the most precise measurement of the Higgs mass up to date.

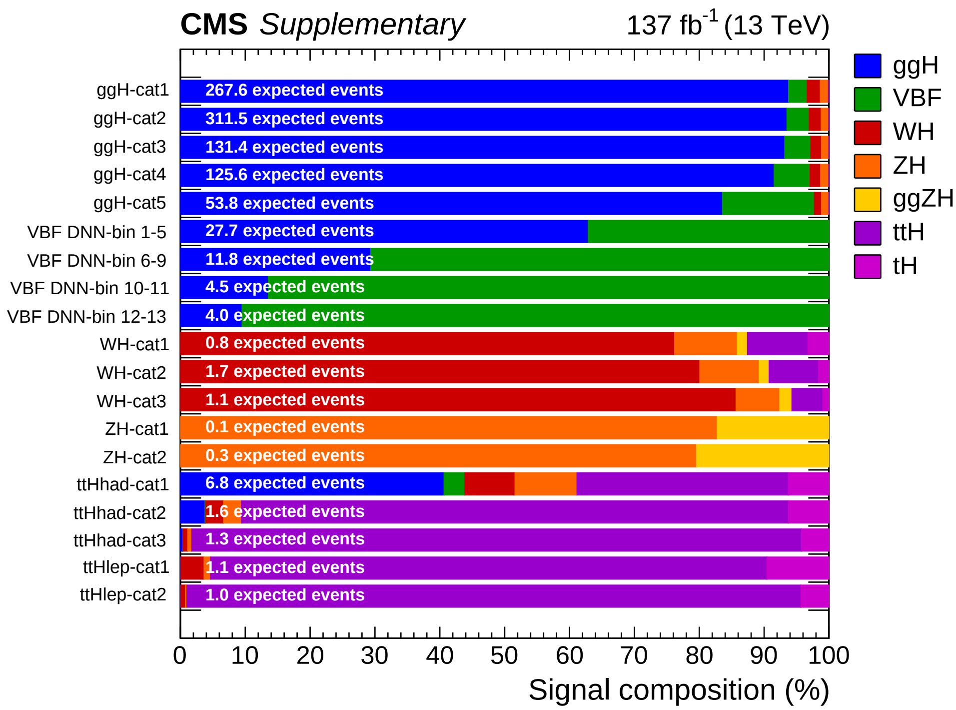

Figure 7-1. Expected fraction of signal events per production mode in the different sub-categories for $m_{\mathrm{H}} = 125.38$ GeV. The tH contribution is defined as the sum of tHq and tHW processes. Plot taken from Ref. [15].

The individual signal strength modifier from each category is summarized in Figure 7-3, with the Higgs signal expected at $m_{\mathrm{H}} = 125.38$ GeV. A combined fit is performed across all categories with one common signal strength modifier, whose best fit value is $\hat{\mu} = 1.19^{+0.41}_{-0.40}(\mathrm{stat})^{+0.17}_{-0.16}(\mathrm{syst})$, shown in the plot as the solid red line.

The statistical significance of the presence of the signal is tested against the null hy-

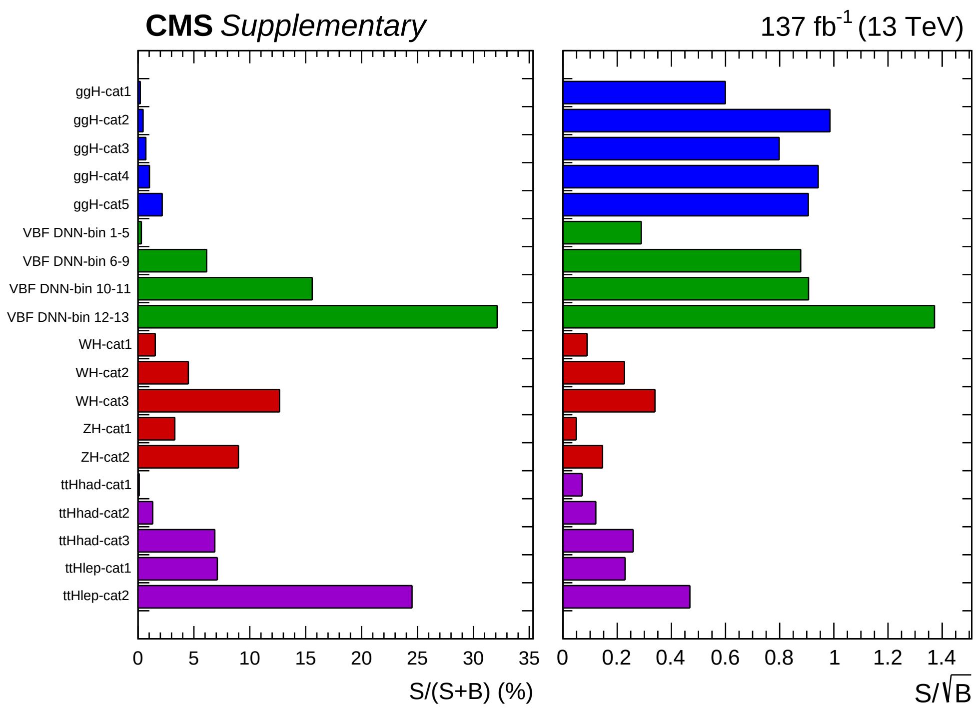

Figure 7-2. Expected $S/(S+B)$ and $S/\sqrt{B}$ in different sub-categories, where S and B indicate the number of expect signal and background events, respectively. Plot taken from Ref. [15].

pothesis, in which no signal is expected and the observed distribution is raised by the statistical fluctuation in the background. A scan of p-value is performed across the mass range of $120\text{GeV} < m_{\mathrm{H}} < 130\text{GeV}$, which quantifies the probability for the background to produce a fluctuation larger than the apparent signal observed in the search region. Figure 7-4 shows the observed and expected (with a signal at 125.38 GeV and $\mu = 1$) p-values for individual categories as well as the overall combination. The overall observed (expected for $\mu = 1$) significance at $m_{\mathrm{H}} = 125.38$ GeV of the incompatibility with the background-only hypothesis is 3.0 (2.5) standard deviations, while the observed (expected for $\mu = 0$) upper limit of the signal strength at the 95% confidence level is 1.9 (0.8) times the SM expectation. This result makes the most sensitive measurement of the $\mathrm{H} \to \mu\mu$ decay rate, establishing the first evidence of the Higgs boson decay to fermions of the second generation.

Finally, the measurement of the $\mathrm{H} \to \mu\mu$ decay rate also provides the measurement on the coupling strength between the Higgs boson and the muon. The coupling strength

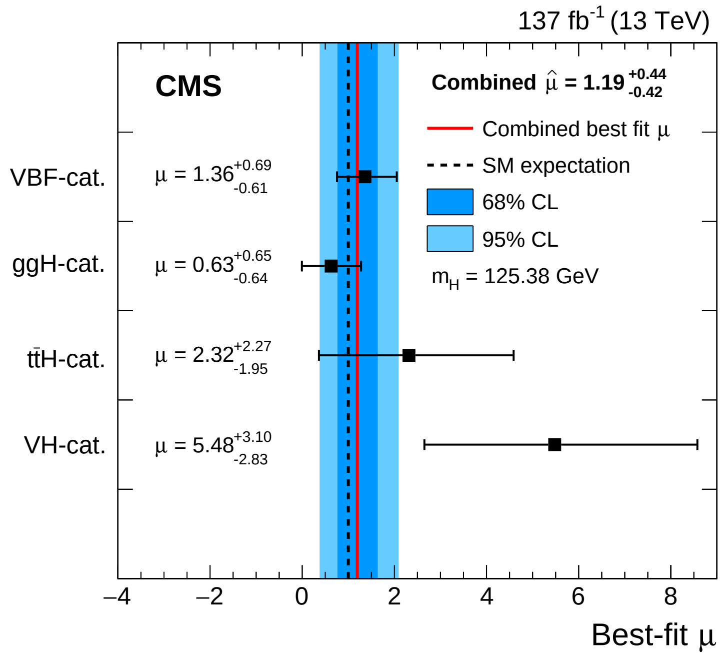

Figure 7-3. Signal strength modifiers measured for $m_{\mathrm{H}} = 125.38$ GeV in each production category (black points) are compared to the result of the combined fit (solid red line) and the SM expectation (dashed gray line). Plot taken from Ref. [15].

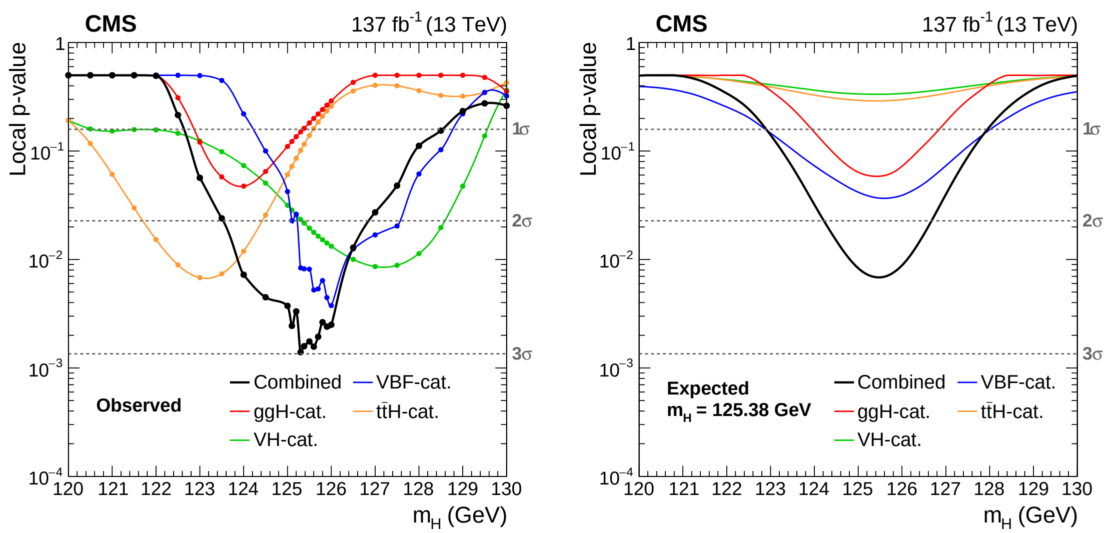

Figure 7-4. The local p-values as a function of different m_{H} hypotheses, for each individual categories as well as the overall combination. The left plot shows the observed p-values, each solid marker indicating a mass point for which the observed p-values are computed. The right plot shows the expected p-values calculated using the background estimate from the S+B fit and injecting a signal with $m_{\mathrm{H}} = 125.38$ GeV and $\mu = 1$. Plot taken from Ref. [15].

is evaluated in the κ-framework [31] and the fit result is shown in Figure 7-5. The best fit value for κ_μ is 1.07 and the corresponding observed 68% confidence interval is $0.85 < \kappa_\mu < 1.29$. This result is furthermore combined with the measurements of the Higgs boson couplings to other particles presented in Ref. [2], which is based on pp collision data recorded by CMS in 2016, corresponding to an integrated luminosity of 35.9 fb^{-1}. As a result, Figure 1-2 is updated to Figure 7-6, providing the best estimated of the six coupling strength modifiers for the Higgs boson coupling to leptons, quarks, and gauge bosons up to date.

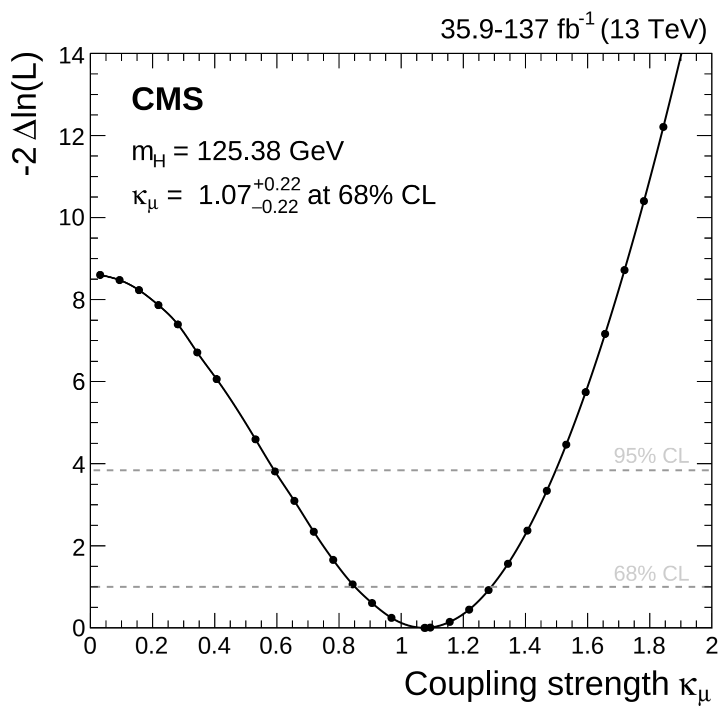

Figure 7-5. The observed profile likelihood ratio as a function of κ_μ for $m_{\mathrm{H}} = 125.38$ GeV. Plot taken from Ref. [15].

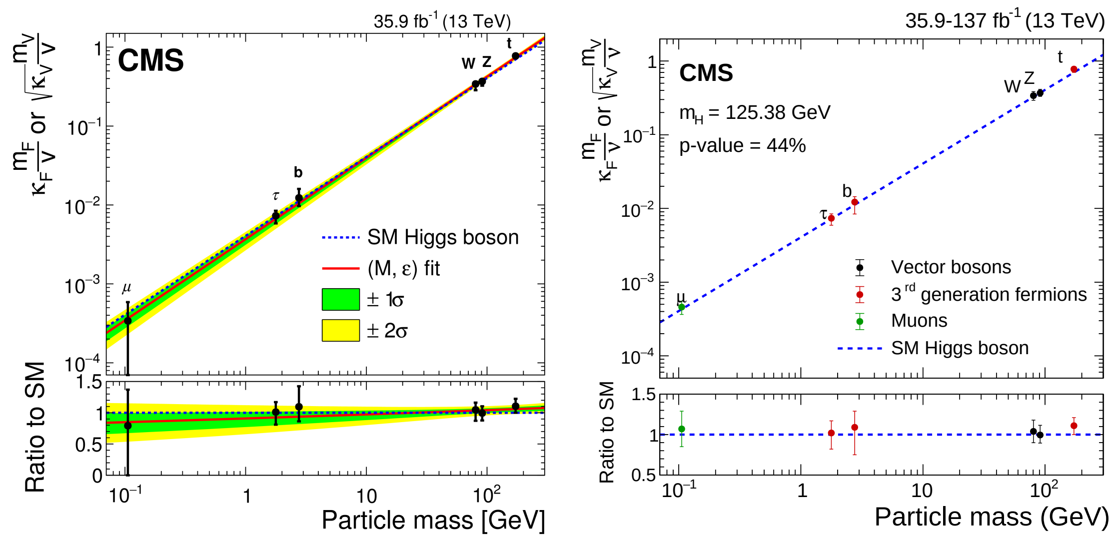

Figure 7-6. Left: A duplicate of Figure 1-2, taken from Ref. [2]. Summary of the CMS measurements on the Higgs coupling to fermions and bosons based on data recorded in 2016. Right: The coupling strength measurements updated with this $H \to \mu\mu$ result. Plot taken from Ref. [15].

[1] Go on a particle quest at the first cern webfest. URL https://cds.cern.ch/journal/CERNBulletin/2012/35/News%20Articles/1473657.

[2] Combined measurements of Higgs boson couplings in proton-proton collisions at $\sqrt{s} = 13$ TeV. *Eur. Phys. J. C*, 79(arXiv:1809.10733. CMS-HIG-17-031-005):421. 67 p, Sep 2018. doi: 10.1140/epjc/s10052-019-6909-y. URL https://cds.cern.ch/record/2640611. Submitted to Eur.Phys.J.

[3] Lyndon Evans and Philip Bryant. LHC machine. *Journal of Instrumentation*, 3(08): S08001–S08001, aug 2008. doi: 10.1088/1748-0221/3/08/s08001. URL https://doi.org/10.1088/1748-0221/3/08/s08001.

[4] Magnetic field of an idealized quadrupole. URL https://en.wikipedia.org/wiki/File:Magnetic_field_of_an_idealized_quadrupole_with_forces.svg.

[5] T Gleisberg, S Höche, F Krauss, M Schönherr, S Schumann, F Siegert, and J Winter. Event generation with SHERPA 1.1. *Journal of High Energy Physics*, 2009 (02):007–007, feb 2009. doi: 10.1088/1126-6708/2009/02/007. URL https://doi.org/10.1088/1126-6708/2009/02/007.

[6] The CMS Phase-1 Pixel Detector Upgrade. Technical Report arXiv:2012.14304, Dec 2020. URL https://cds.cern.ch/record/2748381.

[7] J Mans, J Anderson, B Dahmes, P de Barbaro, J Freeman, T Grassi, E Hazen, J Mans, R Ruchti, I Schimdt, T Shaw, C Tully, J Whitmore, and T Yetkin. CMS Technical Design Report for the Phase 1 Upgrade of the Hadron Calorimeter. Technical Report CERN-LHCC-2012-015. CMS-TDR-10, Sep 2012. URL https://cds.cern.ch/record/1481837.

[8] A Tapper and Darin Acosta. CMS Technical Design Report for the Level-1 Trigger Upgrade. Technical Report CERN-LHCC-2013-011. CMS-TDR-12, Jun 2013. URL https://cds.cern.ch/record/1556311.

[9] Tai Sakuma. Cutaway diagrams of CMS detector. May 2019. URL https://cds.cern.ch/record/2665537.

[10] The CMS Collaboration. Performance of the CMS muon detector and muon reconstruction with proton-proton collisions at $\sqrt{s}$ =13 TeV. *Journal of Instrumentation*, 13(06):P06015–P06015, jun 2018. doi: 10.1088/1748-0221/13/06/p06015. URL https://doi.org/10.1088/1748-0221/13/06/p06015.

[11] CMS Collaboration. Precise mapping of the magnetic field in the CMS barrel yoke using cosmic rays. *Journal of Instrumentation*, 5(03):T03021–T03021, mar 2010. doi: 10.1088/1748-0221/5/03/t03021. URL https://doi.org/10.1088/1748-0221/5/03/t03021.

[12] Sketches of the cms tracker detector. URL https://twiki.cern.ch/twiki/bin/view/CMSPublic/DPGResultsTRK.

[13] Siona Ruth Davis. Interactive Slice of the CMS detector. Aug 2016. URL https://cds.cern.ch/record/2205172.

[14] Oliver Rieger. *Evidence for Higgs boson decays to muons with the CMS experiment at the LHC*. PhD thesis, University of Hamburg, 2021.

[15] CMS Collaboration. Evidence for Higgs boson decay to a pair of muons, 2020.

[16] Georges Aad et al. Observation of a new particle in the search for the Standard Model Higgs boson with the ATLAS detector at the LHC. *Phys. Lett. B*, 716:1, 2012. doi: 10.1016/j.physletb.2012.08.020.

[17] Serguei Chatrchyan et al. Observation of a new boson at a mass of 125GeV with the CMS experiment at the LHC. *Phys. Lett. B*, 716:30, 2012. doi: 10.1016/j.physletb.2012.08.021.

[18] Serguei Chatrchyan et al. Observation of a new boson with mass near 125GeV in pp collisions at $\sqrt{s} = 7$ and 8TeV. *JHEP*, 06:081, 2013. doi: 10.1007/JHEP06(2013)081.

[19] A.M. Sirunyan et al. A measurement of the Higgs boson mass in the diphoton decay channel. *Physics Letters B*, 805:135425, 2020. ISSN 0370-2693. doi: https://doi.org/10.1016/j.physletb.2020.135425. URL https://www.sciencedirect.com/science/article/pii/S037026932030229X.

[20] A.M. Sirunyan et al. Measurements of Higgs boson properties in the diphoton decay channel in proton-proton collisions at $\sqrt{s} = 13$ TeV. *JHEP*, 11(CMS-HIG-16-040. CMS-HIG-16-040-003):185. 56 p, Apr 2018. doi: 10.1007/JHEP11(2018)185. URL https://cds.cern.ch/record/2312121. Submitted to JHEP. All figures and tables can be found at http://cms-results.web.cern.ch/cms-results/public-results/publications/HIG-16-040 (CMS Public Pages).

[21] A.M. Sirunyan et al. Measurements of properties of the Higgs boson decaying to a W boson pair in pp collisions at $\sqrt{s}$ =13TeV. *Physics Letters B*, 791:96–129, 2019. ISSN 0370-2693. doi: https://doi.org/10.1016/j.physletb.2018.12.073. URL https://www.sciencedirect.com/science/article/pii/S0370269319301169.

[22] Albert M Sirunyan et al. Measurements of properties of the Higgs boson decaying into the four-lepton final state in pp collisions at $\sqrt{s} = 13$TeV. *JHEP*, 11:047, 2017. doi: 10.1007/JHEP11(2017)047.

[23] A. M. Sirunyan et al. Observation of Higgs Boson Decay to Bottom Quarks. *Phys. Rev. Lett.*, 121:121801, Sep 2018. doi: 10.1103/PhysRevLett.121.121801. URL https://link.aps.org/doi/10.1103/PhysRevLett.121.121801.

[24] A.M. Sirunyan et al. Observation of the Higgs boson decay to a pair of τ leptons with the CMS detector. *Physics Letters B*, 779:283–316, 2018. ISSN 0370-2693. doi: https://doi.org/10.1016/j.physletb.2018.02.004. URL https://www.sciencedirect.com/science/article/pii/S0370269318301035.

[25] M. Aaboud et al. Cross-section measurements of the Higgs boson decaying into a pair of τ-leptons in proton-proton collisions at $\sqrt{s} = 13$ TeV with the ATLAS detector. *Phys. Rev. D*, 99:072001, Apr 2019. doi: 10.1103/PhysRevD.99.072001. URL https://link.aps.org/doi/10.1103/PhysRevD.99.072001.

[26] M. Aaboud et al. Observation of H $\rightarrow b\bar{b}$ decays and VH production with the ATLAS detector. *Physics Letters B*, 786:59–86, 2018. ISSN 0370-2693. doi: https://doi.org/10.1016/j.physletb.2018.09.013. URL https://www.sciencedirect.com/science/article/pii/S0370269318307056.

[27] M. Aaboud et al. Measurements of gluongluon fusion and vector-boson fusion Higgs boson production cross-sections in the H $\rightarrow$ WW* $\rightarrow e\nu\mu\nu$ decay channel in pp collisions at s=13 TeV with the ATLAS detector. *Physics Letters B*, 789:508–529, 2019. ISSN 0370-2693. doi: https://doi.org/10.1016/j.physletb.2018.11.064. URL https://www.sciencedirect.com/science/article/pii/S0370269318309936.

[28] M. Aaboud and et al. Measurement of the Higgs boson coupling properties in the H $\rightarrow$ ZZ* $\rightarrow 4l$ decay channel at $\sqrt{s} = 13$ TeV with the ATLAS detector. *Journal of High Energy Physics*, 2018(3), Mar 2018. ISSN 1029-8479. doi: 10.1007/jhep03(2018)095. URL http://dx.doi.org/10.1007/JHEP03(2018)095.

[29] A. M. Sirunyan et al. Observation of $t\bar{t}H$ Production. *Phys. Rev. Lett.*, 120:231801, Jun 2018. doi: 10.1103/PhysRevLett.120.231801. URL https://link.aps.org/doi/10.1103/PhysRevLett.120.231801.

[30] M. Aaboud et al. Observation of Higgs boson production in association with a top quark pair at the LHC with the ATLAS detector. *Physics Letters B*, 784:173–191, 2018. ISSN 0370-2693. doi: https://doi.org/10.1016/j.physletb.2018.07.035. URL https://www.sciencedirect.com/science/article/pii/S0370269318305732.

[31] J R Andersen et al. Handbook of LHC Higgs Cross Sections: 3. Higgs Properties. 7 2013. doi: 10.5170/CERN-2013-004.

[32] CMS Collaboration. The CMS experiment at the CERN LHC. *Journal of Instrumentation*, 3(08):S08004–S08004, aug 2008. doi: 10.1088/1748-0221/3/08/s08004. URL https://doi.org/10.1088/1748-0221/3/08/s08004.

[33] V. Khachatryan et al. Search for a standard model-like Higgs boson in the $\mu^+\mu^-$ and e^+e^- decay channels at the LHC. *Physics Letters B*, 744:184 – 207, 2015. ISSN 0370-2693. doi: https://doi.org/10.1016/j.physletb.2015.03.048. URL http://www.sciencedirect.com/science/article/pii/S0370269315002117.

[34] A. M. Sirunyan et al. Search for the Higgs Boson Decaying to Two Muons in Proton-Proton Collisions at $\sqrt{s} = 13$ TeV. *Phys. Rev. Lett.*, 122:021801, Jan 2019. doi: 10.1103/PhysRevLett.122.021801. URL https://link.aps.org/doi/10.1103/PhysRevLett.122.021801.

[35] G. Aad et al. Search for the Standard Model Higgs boson decay to $\mu^+\mu^-$ with the ATLAS detector. *Physics Letters B*, 738:68 – 86, 2014. ISSN 0370-2693. doi: https://doi.org/10.1016/j.physletb.2014.09.008. URL http://www.sciencedirect.com/science/article/pii/S0370269314006583.

[36] M. Aaboud et al. Search for the Dimuon Decay of the Higgs Boson in pp Collisions at $\sqrt{s} = 13$ TeV with the ATLAS Detector. *Phys. Rev. Lett.*, 119:051802, Aug 2017. doi: 10.1103/PhysRevLett.119.051802. URL https://link.aps.org/doi/10.1103/PhysRevLett.119.051802.

[37] Georges Aad et al. A search for the dimuon decay of the Standard Model Higgs boson with the ATLAS detector. Submitted to *Phys. Lett. B*, 2020.

[38] S. Agostinelli et al. Geant4a simulation toolkit. *Nuclear Instruments and Methods in Physics Research Section A: Accelerators, Spectrometers, Detectors and Associated Equipment*, 506(3):250 – 303, 2003. ISSN 0168-9002. doi: https://doi.org/10.1016/S0168-9002(03)01368-8. URL http://www.sciencedirect.com/science/article/pii/S0168900203013688.

[39] Torbjörn Sjöstrand, Stefan Ask, Jesper R. Christiansen, Richard Corke, Nishita Desai, Philip Ilten, Stephen Mrenna, Stefan Prestel, Christine O. Rasmussen, and Peter Z. Skands. An introduction to pythia 8.2. *Computer Physics Communications*, 191:159 – 177, 2015. ISSN 0010-4655. doi: https://doi.org/10.1016/j.cpc.2015.01.024. URL http://www.sciencedirect.com/science/article/pii/S0010465515000442.

[40] Johannes Bellm et al. Herwig 7.0/Herwig++ 3.0 release note. *Eur. Phys. J. C*, 76:196, 2016. doi: 10.1140/epjc/s10052-016-4018-8.

[41] J. Alwall, R. Frederix, S. Frixione, V. Hirschi, F. Maltoni, O. Mattelaer, H. S. Shao, T. Stelzer, P. Torrielli, and M. Zaro. The automated computation of tree-level and next-to-leading order differential cross sections, and their matching to parton shower simulations. *JHEP*, 07:079, 2014. doi: 10.1007/JHEP07(2014)079.

[42] Paolo Nason. A new method for combining NLO QCD with shower monte carlo algorithms. *Journal of High Energy Physics*, 2004(11):040–040, nov 2004. doi: 10.1088/1126-6708/2004/11/040. URL https://doi.org/10.1088%2F1126-6708%2F2004%2F11%2F040.

[43] Stefano Frixione, Paolo Nason, and Carlo Oleari. Matching NLO QCD computations with parton shower simulations: the POWHEG method. *Journal of High Energy Physics*, 2007(11):070–070, nov 2007. doi: 10.1088/1126-6708/2007/11/070. URL https://doi.org/10.1088%2F1126-6708%2F2007%2F11%2F070.

[44] Simone Alioli, Paolo Nason, Carlo Oleari, and Emanuele Re. A general framework for implementing NLO calculations in shower Monte Carlo programs: the POWHEG BOX. *JHEP*, 06:043, 2010. doi: 10.1007/JHEP06(2010)043.

[45] E. Bagnaschi, G. Degrassi, P. Slavich, and A. Vicini. Higgs production via gluon fusion in the POWHEG approach in the SM and in the MSSM. *JHEP*, 02:088, 2012. doi: 10.1007/JHEP02(2012)088.

[46] Keith Hamilton, Paolo Nason, Emanuele Re, and Giulia Zanderighi. NNLOPS simulation of Higgs boson production. *JHEP*, 10:222, 2013. doi: 10.1007/JHEP10(2013)222.

[47] Keith Hamilton, Paolo Nason, and Giulia Zanderighi. Finite quark-mass effects in the NNLOPS POWHEG+MiNLO Higgs generator. *JHEP*, 05:140, 2015. doi: 10.1007/JHEP05(2015)140.

[48] Paolo Nason and Carlo Oleari. NLO Higgs boson production via vector-boson-fusion matched with shower in POWHEG. *JHEP*, 02:037, 2010. doi: 10.1007/JHEP02(2010)037.

[49] Gionata Luisoni, Paolo Nason, Carlo Oleari, and Francesco Tramontano. $HW^{\pm}/HZ + 0$ and 1 jet at NLO with the POWHEG BOX interfaced to gosam and their merging within MiNLO. *JHEP*, 10:083, 2013. doi: 10.1007/JHEP10(2013)083.

[50] Heribertus B. Hartanto, Barbara Jager, Laura Reina, and Doreen Wackeroth. Higgs boson production in association with top quarks in the POWHEG BOX. *Phys. Rev. D*, 91:094003, 2015. doi: 10.1103/PhysRevD.91.094003.

[51] LHC Higgs Cross Section Working Group. Handbook of LHC Higgs Cross Sections: 4. Deciphering the Nature of the Higgs Sector. 10 2016.

[52] Charalampos Anastasiou, Claude Duhr, Falko Dulat, Elisabetta Furlan, Thomas Gehrmann, Franz Herzog, Achilleas Lazopoulos, and Bernhard Mistlberger. High precision determination of the gluon fusion Higgs boson cross-section at the LHC. *JHEP*, 05:058, 2016. doi: 10.1007/JHEP05(2016)058.

[53] Matteo Cacciari, Frédéric A. Dreyer, Alexander Karlberg, Gavin P. Salam, and Giulia Zanderighi. Fully differential vector-boson-fusion Higgs production at next-to-next-to-leading order. *Phys. Rev. Lett.*, 115:082002, 2015. doi: 10.1103/PhysRevLett.115.082002. [Erratum: DOI10.1103/PhysRevLett.120.139901].

[54] Oliver Brein, Abdelhak Djouadi, and Robert Harlander. NNLO QCD corrections to the Higgs-strahlung processes at hadron colliders. *Phys. Lett. B*, 579:149, 2004. doi: 10.1016/j.physletb.2003.10.112.

[55] S. Dawson, C. Jackson, L. H. Orr, L. Reina, and D. Wackeroth. Associated Higgs production with top quarks at the large hadron collider: NLO QCD corrections. *Phys. Rev. D*, 68:034022, 2003. doi: 10.1103/PhysRevD.68.034022.

[56] S. Frixione, V. Hirschi, D. Pagani, H. S. Shao, and M. Zaro. Weak corrections to Higgs hadroproduction in association with a top-quark pair. *JHEP*, 09:065, 2014. doi: 10.1007/JHEP09(2014)065.

[57] Federico Demartin, Fabio Maltoni, Kentarou Mawatari, and Marco Zaro. Higgs production in association with a single top quark at the LHC. *Eur. Phys. J. C*, 75:267, 2015. doi: 10.1140/epjc/s10052-015-3475-9.

[58] Federico Demartin, Benedikt Maier, Fabio Maltoni, Kentarou Mawatari, and Marco Zaro. tWH associated production at the LHC. *Eur. Phys. J. C*, 77:34, 2017. doi: 10.1140/epjc/s10052-017-4601-7.

[59] A. Djouadi, J. Kalinowski, and M. Spira. HDECAY: A program for Higgs boson decays in the standard model and its supersymmetric extension. *Comput. Phys. Commun.*, 108:56, 1998. doi: 10.1016/S0010-4655(97)00123-9.

[60] Michael Spira. QCD effects in Higgs physics. *Fortsch. Phys.*, 46:203, 1998. doi: 10.1002/(SICI)1521-3978(199804)46:3<203::AID-PROP203>3.0.CO;2-4.

[61] Ye Li and Frank Petriello. Combining QCD and electroweak corrections to dilepton production in FEWZ. *Phys. Rev. D*, 86:094034, 2012. doi: 10.1103/PhysRevD.86.094034.

[62] Massimiliano Grazzini, Stefan Kallweit, Dirk Rathlev, and Marius Wiesemann. $W^{\pm}Z$ production at the LHC: fiducial cross sections and distributions in NNLO QCD. *JHEP*, 05:139, 2017. doi: 10.1007/JHEP05(2017)139.

[63] Massimiliano Grazzini, Stefan Kallweit, and Dirk Rathlev. ZZ production at the LHC: fiducial cross sections and distributions in NNLO QCD. *Phys. Lett. B*, 750:407, 2015. doi: 10.1016/j.physletb.2015.09.055.

[64] T. Gehrmann, M. Grazzini, S. Kallweit, P. Maierhöfer, A. von Manteuffel, S. Pozzorini, D. Rathlev, and L. Tancredi. W^+W^- production at hadron colliders in next-to-next-to-leading order QCD. *Phys. Rev. Lett.*, 113:212001, 2014. doi: 10.1103/PhysRevLett.113.212001.

[65] John M. Campbell, R. Keith Ellis, and Ciaran Williams. Vector boson pair production at the LHC. *JHEP*, 07:018, 2011. doi: 10.1007/JHEP07(2011)018.

[66] Michal Czakon and Alexander Mitov. Top++: A program for the calculation of the top-pair cross-section at hadron colliders. *Comput. Phys. Commun.*, 185:2930, 2014. doi: 10.1016/j.cpc.2014.06.021.

[67] P. Kant, O. M. Kind, T. Kintscher, T. Lohse, T. Martini, S. Mölbitz, P. Rieck, and P. Uwer. HATHOR for single top-quark production: Updated predictions and uncertainty estimates for single top-quark production in hadronic collisions. *Comput. Phys. Commun.*, 191:74, 2015. doi: 10.1016/j.cpc.2015.02.001.

[68] Richard D. Ball et al. Parton distributions for the LHC Run II. *JHEP*, 04:040, 2015. doi: 10.1007/JHEP04(2015)040.

[69] Richard D. Ball et al. Parton distributions from high-precision collider data. *Eur. Phys. J. C*, 77:663, 2017. doi: 10.1140/epjc/s10052-017-5199-5.

[70] Johan Alwall et al. Comparative study of various algorithms for the merging of parton showers and matrix elements in hadronic collisions. *Eur. Phys. J. C*, 53:473, 2008. doi: 10.1140/epjc/s10052-007-0490-5.

[71] Rikkert Frederix and Stefano Frixione. Merging meets matching in MC@NLO. *JHEP*, 12:061, 2012. doi: 10.1007/JHEP12(2012)061.

[72] A. M. Sirunyan et al. Identification of heavy-flavour jets with the CMS detector in pp collisions at 13TeV. *JINST*, 13:P05011, 2018. doi: 10.1088/1748-0221/13/05/P05011.

[73] A.M. Sirunyan et al. Particle-flow reconstruction and global event description with the CMS detector. *Journal of Instrumentation*, 12(10):P10003–P10003, oct 2017. doi: 10.1088/1748-0221/12/10/p10003. URL https://doi.org/10.1088%2F1748-0221%2F12%2F10%2Fp10003.

[74] Wolfgang Adam, Boris Mangano, Thomas Speer, and Teddy Todorov. Track Reconstruction in the CMS tracker. Technical Report CMS-NOTE-2006-041, CERN, Geneva, Dec 2006. URL http://cds.cern.ch/record/934067.

[75] The CMS Collaboration. Description and performance of track and primary-vertex reconstruction with the CMS tracker. *Journal of Instrumentation*, 9(10): P10009–P10009, oct 2014. doi: 10.1088/1748-0221/9/10/p10009. URL https://doi.org/10.1088/1748-0221/9/10/p10009.

[76] Are Strandlie and W Wittek. Propagation of Covariance Matrices of Track Parameters in Homogeneous Magnetic Fields in CMS. Technical Report CMS-NOTE-2006-001, CERN, Geneva, Jan 2006. URL http://cds.cern.ch/record/927379.

[77] The CMS Collaboration. Electron and photon reconstruction and identification with the cms experiment at the cern lhc, 2020.

[78] The CMS Collaboration. Performance of photon reconstruction and identification with the CMS detector in proton-proton collisions at $\sqrt{s}$= 8 TeV. *Journal of Instrumentation*, 10(08):P08010–P08010, aug 2015. doi: 10.1088/1748-0221/10/08/p08010. URL https://doi.org/10.1088/1748-0221/10/08/p08010.

[79] Matteo Cacciari, Gavin P Salam, and Gregory Soyez. The anti-ktjet clustering algorithm. *Journal of High Energy Physics*, 2008(04):063–063, apr 2008. doi: 10.1088/1126-6708/2008/04/063. URL https://doi.org/10.1088/1126-6708/2008/04/063.

[80] Matteo Cacciari, Gavin P. Salam, and Gregory Soyez. Fastjet user manual. *The European Physical Journal C*, 72(3), 2012. ISSN 1434-6052. doi: 10.1140/epjc/s10052-012-1896-2. URL https://doi.org/10.1140/epjc/s10052-012-1896-2.

[81] Reconstruction and identification of τ lepton decays to hadrons and $\nu\tau$at CMS. *Journal of Instrumentation*, 11(01):P01019–P01019, jan 2016. doi: 10.1088/1748-0221/11/01/p01019. URL https://doi.org/10.1088/1748-0221/11/01/p01019.

[82] The CMS Collaboration. Performance of reconstruction and identification of τ leptons decaying to hadrons and $\nu\tau$ in pp collisions at $\sqrt{s}$=13 TeV. *Journal of Instrumentation*, 13(10):P10005–P10005, oct 2018. doi: 10.1088/1748-0221/13/10/p10005. URL https://doi.org/10.1088/1748-0221/13/10/p10005.

[83] CMS Collaboration. Performance of missing transverse momentum reconstruction in proton-proton collisions at $\sqrt{s}$ = 13 TeV using the CMS detector. *Journal of Instrumentation*, 14(07):P07004–P07004, jul 2019. doi: 10.1088/1748-0221/14/07/p07004. URL https://doi.org/10.1088/1748-0221/14/07/p07004.

[84] The CMS collaboration. Performance of the CMS missing transverse momentum reconstruction in pp data at $\sqrt{s}$ = 8 TeV. *Journal of Instrumentation*, 10(02):P02006–P02006, feb 2015. doi: 10.1088/1748-0221/10/02/p02006. URL https://doi.org/10.1088/1748-0221/10/02/p02006.

[85] Daniele Bertolini, Philip Harris, Matthew Low, and Nhan Tran. Pileup per particle identification. *Journal of High Energy Physics*, 2014(10), 2014. ISSN 1029-8479. doi: 10.1007/JHEP10(2014)059. URL https://doi.org/10.1007/JHEP10(2014)059.

[86] A. M. Sirunyan et al. Observation of Single Top Quark Production in Association with a Z Boson in Proton-Proton Collisions at $\sqrt{s} = 13$ TeV. *Phys. Rev. Lett.*, 122:132003, Apr 2019. doi: 10.1103/PhysRevLett.122.132003. URL https://link.aps.org/doi/10.1103/PhysRevLett.122.132003.

[87] A. Bodek, A. van Dyne, J. Y. Han, W. Sakumoto, and A. Strelnikov. Extracting muon momentum scale corrections for hadron collider experiments. *Eur. Phys. J. C*, 72:2194, 2012. doi: 10.1140/epjc/s10052-012-2194-8.

[88] Albert M Sirunyan et al. Search for a new scalar resonance decaying to a pair of Z bosons in proton-proton collisions at $\sqrt{s} = 13$ TeV. *JHEP*, 06:127, 2018. doi: 10.1007/JHEP06(2018)127,10.1007/JHEP03(2019)128. [Erratum: JHEP03,128(2019)].

[89] Andrew M. Carnes. *A Search for the Standard Model Higgs Boson Decaying to Two Muons at the CMS Experiment*. PhD thesis, University of Florida, 2018.